
# Investigating the local circulation of the southeast Cape Basin

**by**

**Matthew David Carr**

**Thesis submitted in fulfilment of the requirements for the degree**

**Masters in: Physical Oceanography**

**in the Faculty of Oceanography**

**at the University of Cape Town**

**Supervisor: Dr. T. Lamont**
**Co-supervisor: Dr I. Ansorge**

December 2017

## DECLARATION

I, Matthew David Carr, declare that the contents of this dissertation/thesis represent my own unaided work, and that the dissertation/thesis has not previously been submitted for academic examination towards any qualification. Furthermore, it represents my own opinions and not necessarily those of the University of Cape Town.

**M. Carr** **28/11/2017**

**Signed** **Date**

# Abstract

Located off the west coast of southern Africa, the southeast Cape Basin is characterised by a unique combination of strong coastal upwelling and vigorous offshore mesoscale variability. The juxtaposition of offshore mesoscale variability and coastal upwelling results in a complex and dynamic environment. In this study a combination of *in situ* Acoustic Doppler Current Profiler (ADCP) data and satellite observations were used to identify, describe and characterise the features driving the local circulation within the southeast Cape Basin.

The ADCP data was obtained from the South Atlantic MOC Basin-wide Array (SAMBA), which included four deep sea moorings located along ~34.5°S on the 1000, 2000, 3000 and 4500m isobaths respectively. There was a distinct difference in the circulation observed at the mooring located on the shelf edge (1000m) and the moorings further offshore (2000m, 3000m and 45000m). The offshore circulation, observed by the moorings located on the 2000, 3000, 4500m isobaths, were driven by large mesoscale eddies, both cyclonic and anticyclonic, originating at the Agulhas retroflection and within the Cape Basin itself. The mesoscale eddies induced high speed baroclinic transport events which impacted the upper water column to a depth of at least 400m. The *in situ* observations were used to show the precise characteristics of two cyclonic shelf eddies and one anticyclonic eddy through the upper water column (~50 to 500m). The analysis of these features was important as the physical characteristics of both the cyclonic shelf eddies and anticyclonic eddies through depth are not well known. Considering the short period of observations (18$^{th}$ September 2014 to 1$^{st}$ December 2015), the analysis was not used to assume the prevailing physical characteristics of cyclonic shelf eddies and anticyclonic eddies. Instead the analysis showed the potential for future long term studies to use the sustained *in situ* observations from the SAMBA mooring array and similar analysis to define the precise characteristics of mesoscale eddies through depth. This will greatly improve the understanding of how these features influence the interocean exchange between the Indian and Atlantic Oceans.

The circulation at the shelf edge, observed by the mooring located on the 1000m isobath, was shown to be driven by a combination of offshore mesoscale eddies, the position of the upwelling front and warm filaments formed at the reflection of the Agulhas Current. Identifying the influence of both the offshore mesoscale eddies and coastal upwelling at the shelf edge showed connectivity between the upwelling system and the offshore mesoscale variability. An example of the connectivity between the offshore mesoscale variability and the upwelling front was identified and presented. A dipole formed by two mesoscale eddies was observed to induced cross shelf transport advecting productive shelf waters offshore. The *in situ* observations were used to calculate the amount water transported from

the shelf to the open ocean during this cross shelf transport event. The filament representing the cross shelf transport event was calculated to have a total volume of ~2 x $10^{12}$ $m^3$ with a volume transport of ~1Sv suggesting the event would have had a substantial impact on the local biology. The detailed analysis and quantification of the cross shelf transport event aimed to improve the current understanding of how mesoscale features interact with the upwelling system. *In situ* observations of cross shelf transport are rare, therefore the quantification of the amount of transported in the cross shelf transport event can serve as a baseline for future studies attempting to assess the impact of comparable cross shelf transport events on the local biology.

# ACKNOWLEDGEMENTS

**I wish to thank:**

- Tarron Lamont for the all of her time, guidance and enthusiasm as well as the amazing opportunity to go to sea and be a part of the data collection.
- Isabelle Ansorge for guidance in the structure and themes of the project
- Marion Kersale for assistance with data analysis and methods as well as providing the eddy detection scheme.
- Marcel van den Berg for processing the raw data and opening my eyes to the art of data collection
- National Research Foundation (NRF) for financial assistance. Opinions expressed in this thesis and the conclusions arrived at, are those of the author, and are not necessarily to be attributed to the National Research Foundation.

## TABLE OF CONTENTS



## LIST OF CONTENTS

## LIST OF FIGURES



## LIST OF TABLES

# Chapter 1: Introduction

## The role of the southeast Cape Basin in interocean and coastal-open ocean exchanges

The Cape Basin, located off the west coast of southern Africa (Figure 1.1), plays a vital role in facilitating interocean exchange between the Indian and Atlantic Oceans (Boebel et al. 2003). The interocean exchange, specifically the transfer of Indian Ocean waters into the Atlantic Ocean, around southern Africa has received much attention in the literature due to its significant impact on Atlantic Meridional Overturning Circulation (AMOC). The input of warm, saline waters from the Indian Ocean has been shown to modify the stability of AMOC over various timescales which in turn has a significant influence on the global overturning circulation (Gordon et al. 1992, Biastoch et al. 2008, Beal et al. 2011).

The Cape Basin can be considered as a gateway for Indian Ocean waters to enter the southern Atlantic Ocean due to its geographic location. Indian Ocean waters enter the South Atlantic Ocean via the retroflection of the Agulhas Current and are subsequently advected through the Cape Basin via the Benguela Drift before veering westward into the interior of the South Atlantic Ocean (Figure 2.2) (De Ruijter et al 1999, Beal et al. 2011). Initially studies of the interocean exchange focused on the large anticyclonic eddies, referred to as Agulhas rings, which are sporadically shed from the reflection. The interocean exchange was quantified by observing the rate at which the anticyclonic eddies decay, leaking their Indian Ocean signal into the south Atlantic Ocean (Figure 1.1) (Byrne et al. 1994, Duncombe Rae et al. 1996). Subsequently, a combination of hydrographic and altimetry studies have shown numerous mesoscale features including anticyclonic eddies, cyclonic eddies and filaments to originate from the Agulhas retroflection; all of which play a vital role in the interocean exchange (Lutjeharms and Cooper 1996, Boebel et al. 2003, Richardson 2007, Hall and Lutjeharms 2011). The various mesoscale features are observed to interact with each other within the southeast Cape Basin causing the features to merge, deform and spilt (Boebel et al. 2003). The vigorous stirring and mixing events that result from the interactions between the mesoscale features are thought to facilitate increased exchanges of Indian and Atlantic Ocean waters within the southeast Cape Basin (Boebel et al. 2003, Schmid et al. 2003, Hall and Lutjeharms 2011). This dynamic environment creates uncertainty when attempting to analyse these mesoscale features and interpret their relative impact on interocean fluxes, which in turn decreases researchers' ability to accurately calculate the interocean exchange between the Indian and Atlantic Ocean.

While the offshore regime is dominated by mesoscale variability such as Agulhas rings and cyclonic eddies, the circulation over the continental shelf of the Cape Basin is strongly influenced by the coastal upwelling associated with the southern Benguela upwelling system. The southern Benguela upwelling system plays a vital role in both the biology and circulation of the region. The cold, nutrient rich waters of the upwelling system are vital for the local marine ecosystem as they facilitate primary production which in turn supports substantial fish stocks (Brown et al. 1991, Hutchings et al. 2009). In addition, the cold upwelled waters along the coast creates a strong zonal temperature gradient with the relatively warmer waters situated offshore. The temperature gradient produces a strong horizontal density gradient which result in the formation of a number of coastal jets and shelf edge currents (Veitch and Penven 2017).

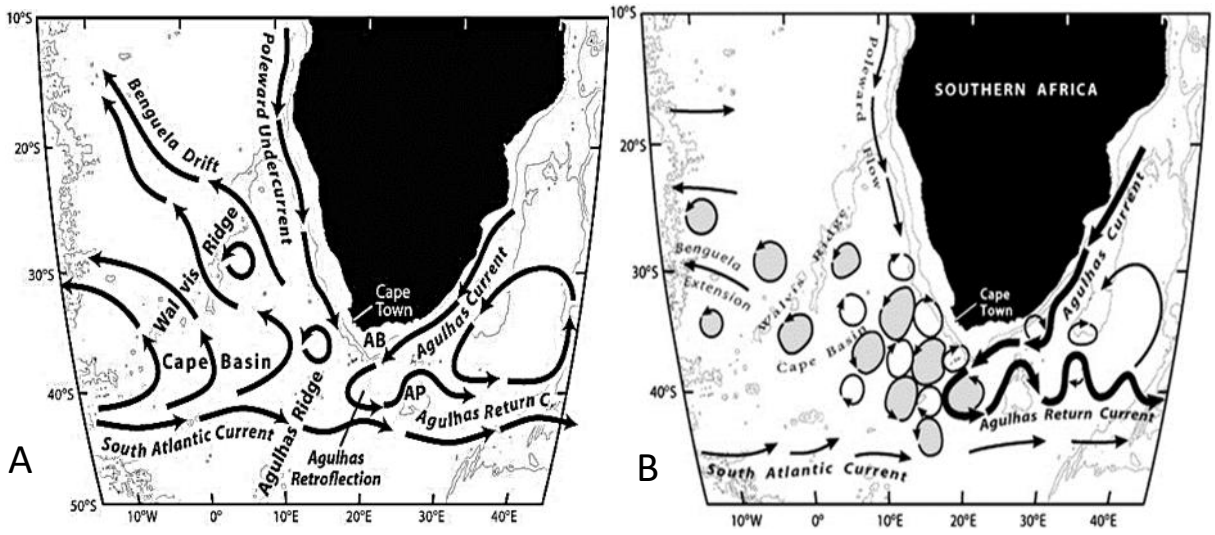


**Figure 1.1: Historical schematic of the interocean exchange around southern Africa. Figure 1.1A represents the interocean exchange as a simple system considering only the Agulhas rings. (Boebel et al. 2003). Figure 1.1B represents the complexities of the southeast Cape Basin indicating the vigorous offshore mesoscale variability after Hall and Lutjeharms (2011).**

The offshore mesoscale variability and coastal upwelling are often studied as separate systems with divergent research questions; however, mesoscale features have been observed to interact with and modify the upwelling front (Duncombe Rae et al. 1992, Shannon and Nelson 1996, Hutchings et al. 1998). The interactions between the upwelling system and mesoscale features are observed to induce coastal-open ocean exchanges which advect productive shelf waters to the open ocean, strongly influencing the marine ecosystem of the region (Duncombe Rae et al. 1992).

The complex environment of the southeast Cape Basin makes interpreting and quantifying the interocean and coastal-ocean exchanges extremely complex. The South Atlantic MOC Basin-wide Array (SAMBA) mooring array thus provides a unique opportunity to observe the interocean and

coastal-ocean exchanges *in situ* for a sustained period. The *in situ* observations provided, for the first time, an opportunity to clarify the nature of the processes involved and allow for improved estimates of the interocean and coastal-ocean exchanges in this region.

The SAMBA array located at 34.5°S (Figure 3.1) was deployed in 2014 within the southeast Cape in order to increase the number of *in situ* observations within the South Atlantic Ocean. The initiative behind this programme aimed to provide a long term set of high resolution *in situ* observations through the upper water column in an attempt to resolve complex circulation of the southeast Cape Basin and in so doing quantify the region's influence on interocean exchange and global circulation (Ansorge et al. 2014).

This thesis presented the first year (18$^{th}$ September 2014 to 1$^{st}$ December 2015) of data recorded by the SAMBA mooring array. The thesis highlighted the ability of the *in situ* observations to capture the distinctive the oceanographic features within the southeast Cape Basin. The *in situ* observations were used to present detailed analysis of these oceanographic features which impact on both interocean exchange and coastal-open ocean exchange within the region. Considering the SAMBA array is the first long term mooring array in this region and the thesis used only the first year of data, the analysis did not aim to present conclusive physical characteristics of these features but rather show the potential for future data sets from the SAMBA mooring array to do so and improve estimates of interocean exchange and coastal-open ocean exchanges. The thesis was presented in four sections which aim to:

- Describe the local circulation observed along the mooring array, specifically the differences between the circulation offshore and at the shelf edge.
- Provide detailed analysis of individual mesoscale features within the dynamic environment of the southeast Cape Basin and in so doing show the ability of the *in situ* observations to improve the estimates of inter ocean exchange in future long term studies.
- Show the connectivity between the offshore mesoscale features and the coastal upwelling system by demonstrating the role of both systems on the circulation at the shelf edge.
- Improve the current understanding of how mesoscale features interact with the upwelling system. The section shows the potential of the *in situ* observations calculate the scale of the interactions between mesoscale features and the upwelling system and improve the understanding of their relative the impact on the local marine system.

# Chapter 2: Literature Review

## 2.1 Geographical Location

Located off the west coast of southern Africa in the south eastern Atlantic Ocean the Cape Basin is bounded by the Agulhas ridge to the south and Walvis ridge to the north (Figure 2.1). The west coast of southern Africa and the southern extent of the mid-Atlantic ridge complete the Basin on the east and west respectively (Figure 2.1). The continental shelf is defined by the 1000m isobath. The shelf edge within the Cape Basin is relatively uniform showing little variation from the Agulhas Bank to the Walvis Ridge (Hutchings et al. 2002).

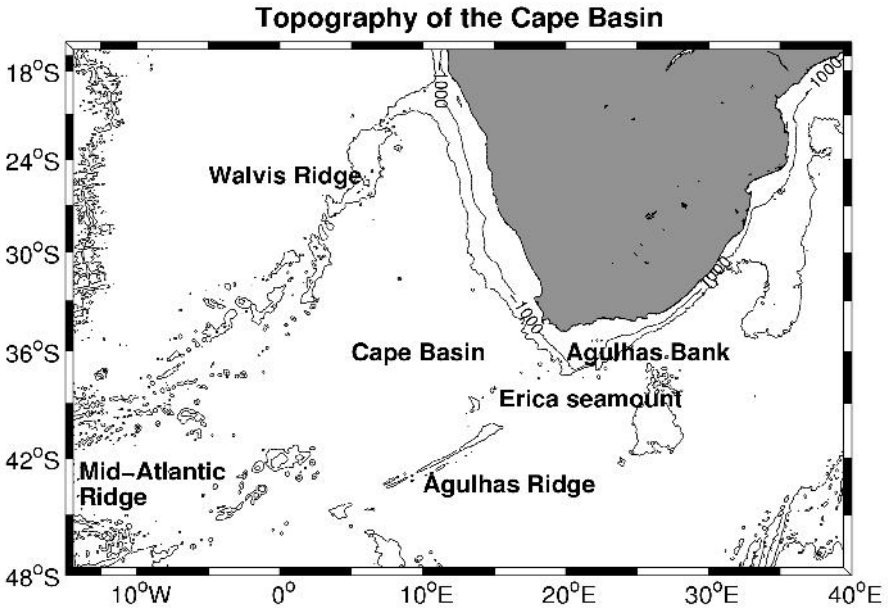


**Figure 2.1: Topographic features defining the Cape Basin. The 1000, 3000m isobaths are displayed.**

## 2.2 Large-scale circulation features

### 2.2.1 The Benguela Current

The basin scale circulation patterns of the Cape Basin are dominated by the Benguela Current which forms the eastern boundary current of the South Atlantic sub-tropical gyre (Peterson and Stramma 1991). Analogous to other global eastern boundary currents, the Benguela Current is a broad, cool, relatively weak flow. The current flows northwards from approximately 35°S to 21°S (Garzoli and Gordon 1996, Wedephohl et al. 2000).

The width of the Benguela current increases from 200km in the south(±35°S) to 750km northwards(±23°S); however, the weak flow and transient nature of the offshore edge and limited sampling in the region increases the uncertainty of the offshore boundary. This results in a discrepancy

in the width of the current within the scientific community (Shannon 1985, Wedephol et al. 2000). The mean drift speed of the Benguela Current, derived from ship-drift observations, ranges from 11 to 23cm.$s^{-1}$ (Wedephol et al. 2000). A moored array (July 1992 to November 1993) at 30°S, deployed during BEST (Benguela Sources and Transport) project, observed a northward transport of 13Sv (1Sv =1x $10^6 m^3 s^{-1}$) for the first 1000m (Garzoli and Gordon 1996). North of 26°S, a large offshore component of the Benguela Current turns westward. The westward flowing band, referred to as the Benguela extension, is centred at approximately 30°S (Schmid et al. 2003, Boebel et al. 2003). This extension joins the South Equatorial Current forming the northern limb of the South Atlantic sub-tropical gyre (Hardman-Mountford et al. 2003, Boebel et al. 2003) while its inshore branch continues northwards until it reaches the Angola-Benguela front (Hardman-Mountfoud et al. 2003).

## 2.3 Sources of the Cape Basin

There are three distinct oceanographic features that supply waters to the Cape Basin; the South Atlantic Current (SAC), the Agulhas retroflection and south of the Subtropical Convergence, via the advection of waters from the Antarctic Circumpolar Current (Garzoli and Gordon 1996).

### 2.3.1 The South Atlantic Current

The SAC forms the southern limb of the Southern Atlantic sub-tropical gyre, entraining South Atlantic Central Water (SACW) typical of the sub-tropical South Atlantic Ocean into the Cape Basin from the southwest (Figure 2.2) (Stramma and England 1999). Observations from the KAPEX float programme (Boebel et al. 1998) indicated the SAC splits before entering the Cape Basin (Richardson 2007). Floats and drifters seeded within the SAC south of 41°S tended to continue eastward, south of the Cape Basin. The majority of floats and drifters seeded north of 41°S drifted north eastward joining the Benguela Current and entering the Cape Basin (Richardson 2007). Using the float trajectories, the northern branch of the SAC is suggested to be centred approximately 38°S. The southern branch is suggested to be centred around 43°S (Richardson 2007). The spilt of the SAC has been suggested to indicate a westward extension of the Agulhas Current (Figure 2.2), which may result in a blend of south Indian Ocean and South Atlantic waters entering the Cape Basin through the northern branch of the SAC; thus providing an additional source of Indian Ocean waters into the Cape Basin (Richardson 2007). Geostrophic transports derived from observational *in situ* data indicate that the SAC supplies ~5Sv to the Benguela Current (Gordon et al. 1992). The transport is in agreement with Garzoli and Gordon (1996) who suggested that of the 13Sv transported by the Benguela Current, 50% is derived from the central Atlantic Ocean.

### 2.3.2 The Agulhas retroflection

The Agulhas Current is tightly constrained by the continental slope and flows, southwards along the east coast of South Africa. The current separates from the coast before sharply retroflecting and returning eastward into the Indian Ocean at approximately 37 °S (Lutjeharms and Ballegooyen 1988).

The inertial overshoot and sharp retroflection of the Agulhas Current allows for a significant amount of south India Ocean waters to escape the retroflection and persist into the South Atlantic Ocean (Gordon et al. 1992, De Ruijter et al. 1999a). The collective term for the water which persists in the South Atlantic is Agulhas leakage (Beal et al. 2011). Agulhas Leakage occurs predominantly in the form of large anticyclonic eddies ($\sim 250 km$ in diameter), which are shed from the retroflection, while cyclonic eddies and filaments formed at the retroflection play a secondary role (Lutjeharms and Cooper 1996, Beal et al. 2011) (Figure 2.2). The Agulhas retroflection and ring shedding process has been widely researched and Lutjeharms (2006) provides a full description of the known dynamics controlling ring shedding events. The combination of filaments, anticyclonic eddies and cyclonic eddies, as well as their subsequent interactions with local flows within the Cape Basin, are extremely complex, resulting in discrepancies (2Sv to 15Sv) within the literature when attempting to quantify the amount of Indian Ocean water transported into the Cape Basin (Beal et al. 2011). Observational data from Gordon et al. (1992) suggests that the Agulhas Current contributes as much as 10Sv to the Benguela Current and the Cape Basin. Highlighting the complexity in quantifying Agulhas Leakage; Richardson (2007) observed a leakage of 15Sv using sub-surface floats and drifters. Despite the complexity in quantifying Agulhas Leakage there is a general consensus within the literature that Indian Ocean water from the Agulhas retroflection is a significant, if not dominant source of the Cape Basin (Gordon et al. 1992, Garzoli and Gordon 1996, Richardson 2007, Vietch et al. 2010).

### 2.3.3 Subtropical Convergence

The shedding of anticyclonic eddies from the retroflection of the Agulhas Current has been observed to disturb the Subtropical Convergence entraining sub-antarctic surface water (SAWS) from the Antarctic Circumpolar Current into the Cape Basin (Garzoli and Gordon 1996). The sub-antarctic waters are advected in the form of relatively thin filaments, only occasionally over 150km in width (Lutjeharms 1988). The shedding of anticyclonic eddies from the retroflection is sporadic and the advection of sub-antarctic surface waters in not always observed during a shedding event. As a result the contribution of sub-antarctic waters to the Cape Basin is unclear but it is surmised to be secondary to the contributions from the SAC and Agulhas Leakage (Garzoli and Gordon 1996).

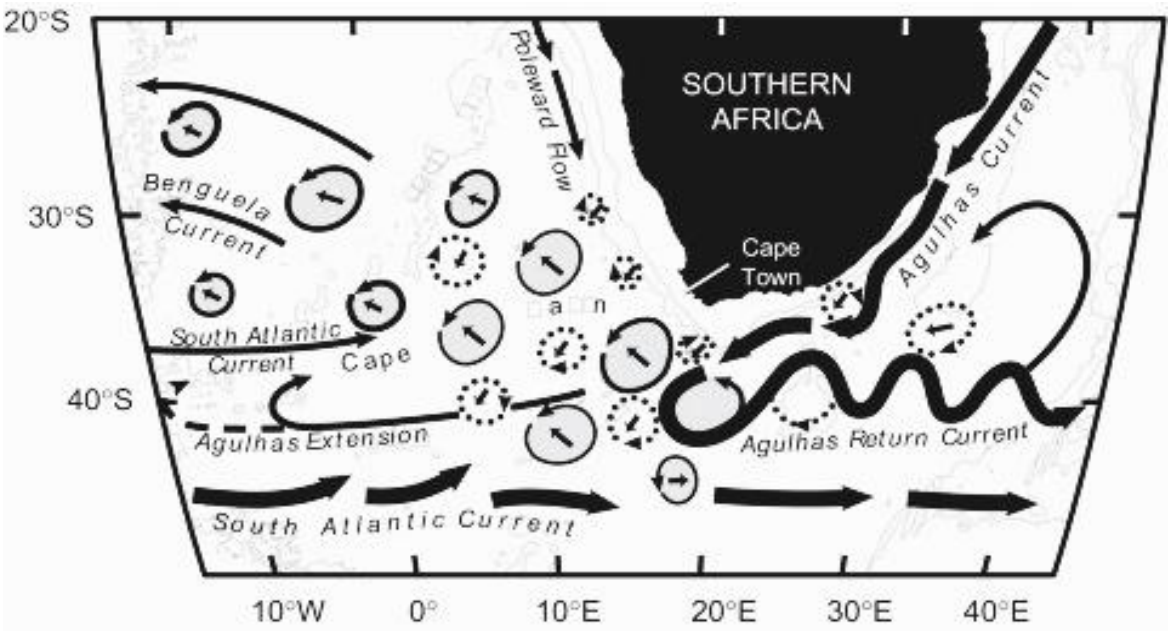


**Figure 2.2: The oceanographic features supplying water to the Cape Basin. The South Atlantic Current, Agulhas Leakage and Agulhas extensions are shown. The advection of sub-antarctic waters is not denoted however the shedding of eddy at the position of the Subtropical convergence (±38°S) highlights mechanism in which sub-antarctic waters are advected into the Cape Basin. (Richardson 2007).**

## 2.4 Basin scale circulation

The circulation of the Cape Basin is controlled by a combination of oceanographic features including strong coastal upwelling, local jet currents and offshore mesoscale variability.

### 2.4.1 Coastal upwelling

The Benguela Current Large Marine Ecosystem (BCLME) is one of the four upwelling systems in the world. Here, cold, nutrient rich waters are upwelled due to the offshore Ekman transport resulting from alongshore winds set up by the anticyclonic motion around the atmospheric South Atlantic high pressure system and continental low pressure trough (Shannon and Nelson 1996). The upwelling system extends along the west coast of southern Africa from 14°S to 37°S. The upwelling system is not uniform along the coast but divided into seven distinct regions of enhanced upwelling or upwelling cells (Figure 2.3) (Lutjeharms and Meeuwis 1987). These upwelling cells are associated with local increases in wind stress or a change in coastline orientation (Shannon and Nelson 1996). The Lüderitz upwelling cell (~27.5°S) is considered the most vigorous and forms the northern border of the southern Benguela system (Shannon and Nelson 1996). The BCLME is divided into the northern and southern systems due to variations in physical and biological characteristics. Only the southern Benguela system falls within the Cape Basin as the southern Benguela upwelling system extends from

the Lüderitz upwelling cell to the retroflection of the Agulhas Current which is considered the oceanographic southern border of the BCLME (~ 37°S 25°E) (Figure 2.3). A strong seasonal (strongest during austral spring and summer) signal is observed within the southern Benguela system compared to the perennial upwelling observed in the northern system (Andrews and Hutchings 1980). The southern Benguela system's strong seasonal signal is a result of the seasonal meridional shift of the South Atlantic high pressure system (Shannon and Nelson 1996).

The upwelling front of the southern Benguela system is well defined and generally follows the shelf break, compared to the northern Benguela upwelling front which is more diffuse with multiple fronts on occasion (Shannon and Nelson 1996). Intense offshore mesoscale activity is observed within the southern Benguela system in the form of eddies and filaments originating from the retroflection region and within southern Benguela system (Boebel et al. 2003, Vietch et al. 2009, Rubio et al. 2009). The mesoscale activity, further elaborated on below, has been observed to interact with the upwelling front, inducing large filaments of upwelling water that extend offshore and convolute the upwelling front (Duncombe Rae et al. 1992, Shannon and Nelson 1996, Hutchings et al. 1998). These cross shelf transport events have been shown to entrain fish eggs, larvae and substantial amounts of chlorophyll-a which has a direct influence on the marine ecosystem of the southern Benguela upwelling system (Duncombe Rae et al. 1992, Hutchings et al. 2002). However, the scale, and therefore the impact on the marine ecosystem, of these cross shelf transport events remain relevantly unknown as observations of these events have been limited to sparse hydrographic cruise data (Duncombe Rae et al. 1992, Nelson et al. 1998, Shillington et al. 1992). Observations from three cruises showed the cross shelf transport events are in the order of 50 – 100 meters deep and characterised by speeds of 50 – 70 $cm.s^{-1}$ (Duncombe Rae et al. 1992, Shillington et al. 1992).

### 2.4.2 Local jet currents and undercurrent

A number of local jet currents have been observed across the shelf of the southern Benguela system (Figure 2.3). The most frequently observed and described jet is located off the Cape Peninsula upwelling cell. The jet is often referred to as the Goodhope Jet or Benguela Jet. The jet is a narrow (20-30 km) equatorward current generally located between the 300 and 400m isobaths but is observed to shift zonally across the shelf (Nelson et al. 1998). Bang and Andrews (1974) predicted and observed the jet which was proposed to result from the strong offshore sea surface temperature (SST) gradient. The cool upwelled coastal waters and warm offshore water from the Indian Ocean influx create strong horizontal SST gradients and therefore density gradients. The Goodhope Jet is observed to be a permanent feature despite the strong seasonality of the southern Benguela upwelling, suggesting a discontinuity between the SST gradient set up by upwelling favourable winds and the jet

(Shannon and Nelson 1996, Nelson et al. 1998). The discontinuity is likely a result of the Indian Ocean influx which shows no discernible seasonality (Veitch and Penven 2017). The lack of seasonality highlights the importance of warm Agulhas influx in creating the density gradient driving the Jet. The mean speed of the jet is typically quoted as ±50cm.s$^{-1}$, however, observations of the jet are highly variable (Bang and Andrews 1974, Shannon and Nelson 1996, Wedepohl et al. 2000). The Goodhope Jet plays a vital role in the recruitment of several fish species. Fish larvae are transported via the Goodhope Jet, from the spawning grounds on the Agulhas Bank to their nursery area in St. Helena Bay (Shelton and Hutchings 1982).

Similar to the other major global upwelling system, a poleward undercurrent is observed within the Benguela upwelling system (Shannon and Nelson 1996). The poleward undercurrent has been shown to extend along the coast as far as the Cape Peninsula with observed speeds of 5 to 10 cm.s$^{-1}$ (Nelson 1989). However, there is a deepening of the current, partly due to the conservation of potential vorticity, as it moves southward resulting in few observations of the undercurrent in the southern Benguela upwelling system (Veitch et al. 2009). The undercurrent is observed between 100 – 500m depth along the shelf edge in the northern Benguela upwelling system (Blanke et al. 2005, Mohrholz et al. 2008, Veitch et al. 2009).

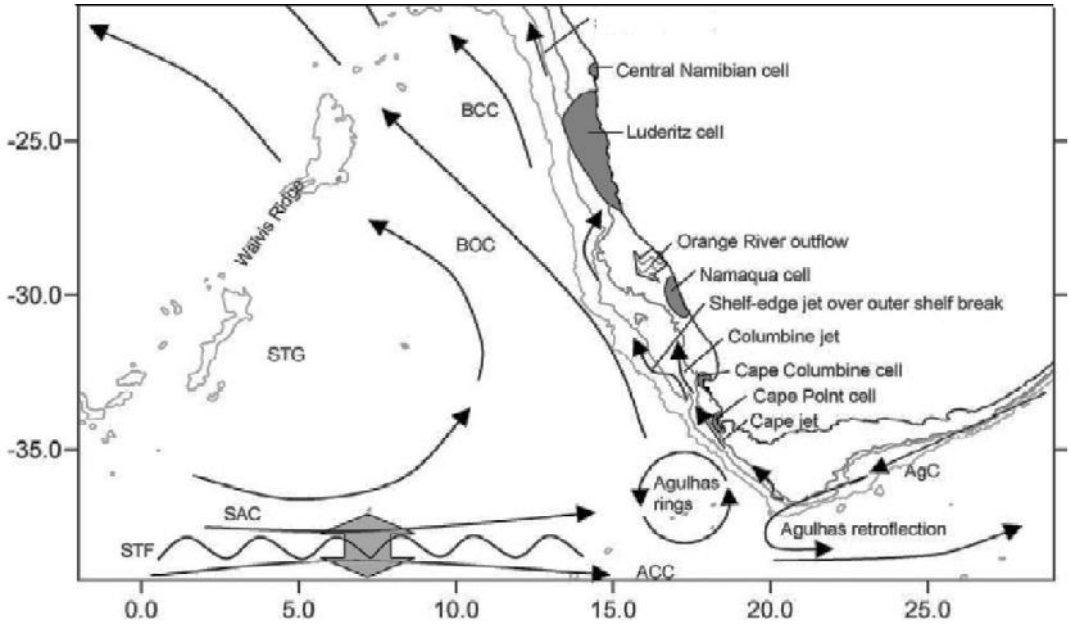


**Figure 2.3: Schematic of the southern Benguela upwelling system highlights the upwelling cells associated with regions of enhanced upwelling. The local jet currents are shown along the shelf edge. The acronyms are as follows: BOC - Benguela Oceanic Current, BCC – Benguela Coastal Current, SAC – South Atlantic Current, AgC - Agulhas Current, STF – Subtropical front, STG – Subtropical Gyre, ACC –Antarctic Circumpolar Current. Adapted from Hardman-Mountford et al. (2003).**

### 2.4.3 Cyclonic and anticyclonic eddies of the Cape Basin

The anticyclonic mesoscale eddies which persist from the Agulhas retroflection, often referred to as Agulhas rings, have dominated the literature in the region due to their significant influence on interocean exchange. However, a combination of float, drifter and altimetry studies have shown that rather than being dominated by anticyclonic eddies, the southeast Cape Basin is a highly energetic field of co-existing cyclonic and anticyclonic eddies (Boebel et al. 2003, Richardson 2007, Hall and Lutjeharms 2011).

#### 2.4.3.1 Anticyclonic eddies

The Cape of Good Hope Experiments (KAPEX) seeded numerous naturally buoyed floats within the Cape Basin in an attempt to resolve interocean exchange around southern Africa (Boebel et al. 1998). KAPEX provided for the first time high resolution *in situ* observations of mesoscale features within the region. During the period of the KAPEX float project (1997-1999) 29 anticyclonic eddies were identified within the Cape Basin (Figure 2.4). However, only 10 of these anticyclonic eddies crossed 5°E representing a 'traditional' long lived Agulhas ring. The 29 anticyclonic eddies observed within the southeast Cape Basin exhibited a mean north westward drift of 3.8±1.2cm.s$^{-1}$ with average diameter of 200 km (Boebel et al. 2003). Richardson (2007) observed a mean north westward drift of 4.4cm.s$^{-1}$ and an average diameter of 250km using additional drifters and sub-surface floats in conjunction within the KAPEX observations. The mean north westward trajectory was further confirmed by Dencausse et al. (2010) from altimetry data in which 199 anticyclonic eddies, including anticyclonic features which spilt and merged, were tracked over 14 years of data. *In situ* cruise data of an Agulhas ring show the anticyclonic feature had a baroclinic signal which penetrated to a depth of 4500m and confirmed Indian Ocean water within the feature (van Aken et al. 2003).

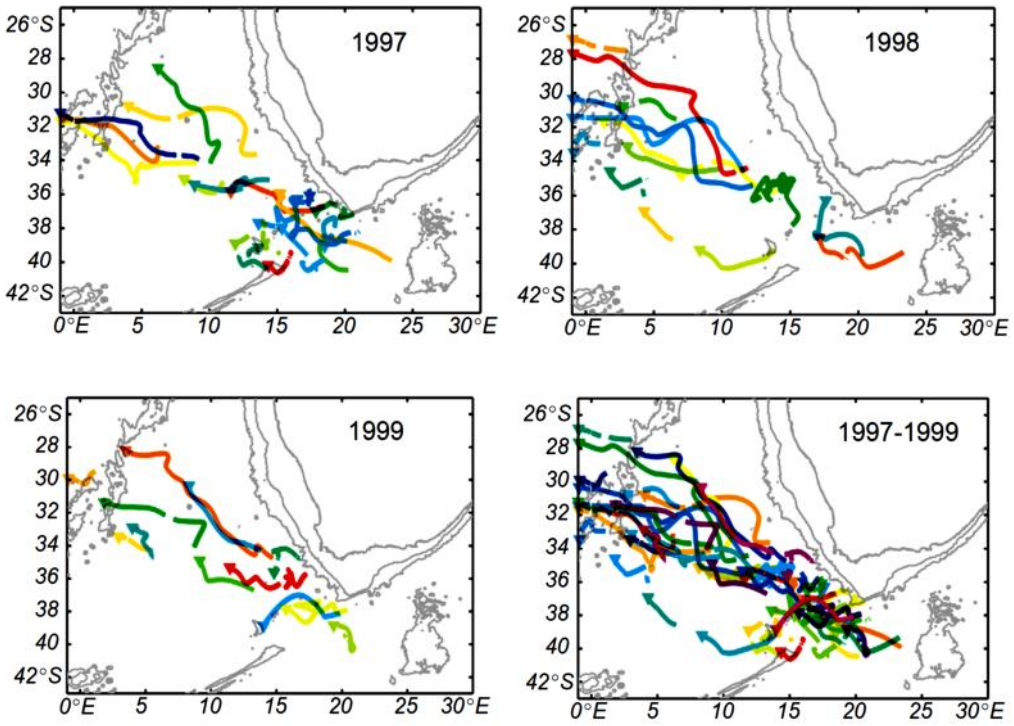


**Figure 2.4: The anticyclonic eddies and associated trajectories observed during the KAPEX experiment for 1997, 1998, 1999 and the combined trajectories for the three years. (Boebel et al. 2003). The trajectories observed during the KAPEX experiment confirms the general north westward trajectory of anticyclonic eddies within the Cape Basin and highlights the difference between the trajectories of anticyclonic eddies within the southeast Cape Basin and the northern Cape Basin.**

The trajectories and structure of anticyclonic eddies within the southeast Cape Basin and northern Cape Basin are dissimilar. Trajectories within the northern Cape Basin exhibited a relatively constant north westward drift while the southeast Cape Basin displayed a complex, turbulent flow regime (Boebel et al. 2003, Dencausse et al. 2010). The complex flow regime is highlighted by a high variability in the translation speeds of the anticyclonic eddies within the southeast basin (Schmid et al. 2003). Additionally, the anticyclonic eddies were observed to merge, split, deform and reconnect to the Agulhas Retroflection within the southeast Cape Basin compared to the northern Cape Basin where the anticyclonic eddies where observed to retain a circular shape (Boebel et al. 2003, Richardson 2007). The complex flow of the southern Cape Basin has been attributed to a combination of the topography and the cyclonic eddies which significantly influences the speed, trajectory and structure of the anticyclonic eddies (Arhan et al. 1999, Dencausse et al. 2010).

In an attempt to classify the complex flow regime of anticyclonic eddies within the southeast Cape Basin, Dencausse et al. (2010) observed three general pathways anticyclonic eddies would follow relative to topographical features. A total of 32% of the anticyclonic eddies (59 out of 186) passed north of the Erica seamount (Figure 2.1) following the 'northern route', 48% (90 out of 186 anticyclonic eddies) passed through the Erica seamount and the Agulhas Ridge following the 'central route' and

20% (37 out of 186 anticyclonic eddies) passed south of the Agulhas Ridge following the 'southern route'. The preference of the central route over the northern route is unexpected as the central route provides greater topographical obstructions (Dencausse et al. 2010). The tendency to favour the central route may be explained by the numerous cyclonic eddies formed along the continental shelf (further elaborated below) which may prove a greater obstacle than topographic features (Dencausse et al. 2010).

#### 2.4.3.2 Cyclonic eddies

A key finding of the KAPEX float programme was the large number of cyclonic eddies within the southeast Cape Basin. Cyclonic eddies were observed to outnumber anticyclonic eddies by a factor of 3:2 within the southeast Cape Basin (Boebel et al. 2003). The cyclonic eddies were observed to have overall west south westward drift of 3.6±8cm.$s^{-1}$ (Boebel et al. 2003). The mean west south westward drift (Figure 2.5) was further confirmed by Hall and Lutjeharms (2011) using ten years of altimetry data (1992-2002). The cyclonic eddies were observed to have a mean diameter of approximately 120km (Boebel et al. 2003, Hall and Lutjeharms 2011). However, cyclonic eddies with comparable scales to anticyclonic eddies, greater than 200km, were also observed. An average life span of 250±18 days was observed from 105 cyclonic eddies identified (Hall and Lutjeharms 2011).

The cyclonic eddies show three distinct regions of formation; inshore of the Agulhas Current, south of the Subtropical Convergence within the sub-antarctic zone and along the continental shelf within the Cape Basin.

Cyclonic eddies are formed as shear features, inshore of the Agulhas Current, during the propagation of a Natal Pulse (Lutjeharms et al. 2003). A Natal Pulse is a solitary meander which propagates southwards through the Agulhas Current (De Ruijter et al. 1999b). Natal Pulses are thought be generated through baroclinic instability at the anomalously shallow continental slope between St Lucia (28°S) and Durban (30°S) referred to as the Natal Bight (Van Leeuwen et al. 2000, De Ruijter et al. 1999b). The associated cyclonic eddy propagates southward with the Natal Pulse and is shed into the Cape Basin (Lutjeharms et al. 2003). Similar shear edge cyclonic eddies have been observed to form inshore of the southern Agulhas Current, at the bight of the Agulhas Bank, and propagate in the Cape Basin without the presence of Natal Pulses (Lutjeharms et al. 2003). Collectively the cyclonic eddies produced inshore of the Agulhas current are referred to as Agulhas cyclones. In addition, these shear edge eddies are thought to trigger the formation of additional cyclonic lee eddies adjacent to the Agulhas Bank, which detach from the bank and enter the southeast Cape Basin (Lutjeharms et al. 2003).

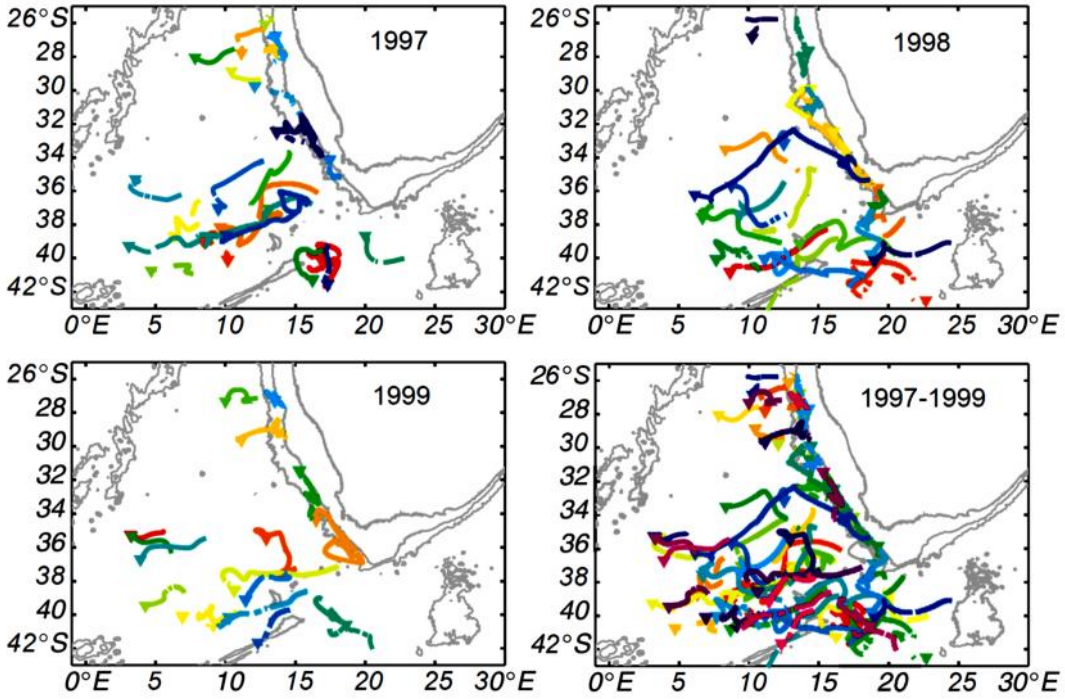


**Figure 2.5: The cyclonic eddies and associated trajectories observed during the KAPEX experiment for 1997, 1998, 1999 and a combination of the three years (Boebel et al. 2003). The observed trajectories of the cyclonic eddies confirm the west south westward trajectory of the cyclonic eddies within the Cape Basin and highlights the three regions associated with the formation of cyclonic eddies.**

Cyclonic eddies have also been observed to enter the southeast Cape Basin from the sub-Antarctic zone, south of the Agulhas Current. No floats from the KAPEX experiment were entrained within a sub-antarctic eddy; however, they are clearly identified with altimetry data (Boebel et al. 2003). All sub-antarctic cyclonic eddies observed from the altimetry formed eastward of the Agulhas Retroflection and entered the Cape Basin through the same passage as the anticyclonic eddies shed from the reflection using the deep passage between the Agulhas Bank and Agulhas Ridge (Boebel et al. 2003). These cyclonic eddies are thought to carry sub-antarctic waters into the southeast Cape Basin, however, hydrographic observations of these eddies are absent.

A large number of cyclonic eddies within the Cape Basin have been observed to form along the continental shelf (Boebel et al. 2003, Hall and Lutjeharms 2011, Baker-Yeboah et al. 2010). During ten years of data Hall and Lutjeharms (2011) observed 12 out every 13 cyclonic eddies were first detected inshore of the 4000m isobath. Rubio et al. (2009) observed a similar trend of high cyclonic eddy formation over the continental slope using altimetry and model observations. The formation of cyclonic eddies is observed along the entire length of the continental shelf within the Cape Basin 24°S - 35°S. The formation of cyclonic shelf eddies shows no significant correlation to the intense upwelling

cells associated with the upwelling system; and therefore the upwelling cells appear not to influence the formation of the cyclonic eddies contrary to previous suggestions (Hall and Lutjeharms 2011). Instead the cyclonic shelf eddies may be generated through the interaction of Agulhas Rings with the continental shelf (Baker-Yeboah et al. 2010). The formation of cyclonic eddies along the continental shelf and the subsequent westward translation plays a vital role in the exchange of waters across the shelf. Rubio et al. (2009) estimate cyclonic shelf eddies can transport between 2 and $4.5x10^{12}m^3$ of shelf waters to the open ocean during its translation. The high number of cyclonic eddies formed along the shelf edge increases the probability of the interactions between mesoscale eddies and the upwelling front as observed by Duncombe Rae et al. (1992).

#### 2.4.3.3 Interaction of cyclonic and anticyclonic eddies

The west southwestward trajectory of thef cyclonic eddies crosses the north westward trajectory of the anticyclonic eddies. The intersecting trajectories result in numerous interactions between the features. The cyclonic eddies significantly influence the path, structure and dissipation of anticyclonic eddies; playing a significant role in deforming and splitting anticyclonic eddies within the southeast Cape Basin (Boebel et al. 2003, Baker-Yeboah et al. 2010, Dencausse et al. 2010). The intermediate depth floats of the KAPEX experiment were observed to regularly exchange between cyclonic and anticyclonic eddies within the southeast Cape Basin indicating the entrainment of waters and vigorous mixing between features (Boebel et al. 2003). The regular exchange between features is suggested to increase the decay of the Indian Ocean signal into the background waters of the Cape Basin (Boebel et al. 2003). This enhanced interocean exchange increases the need for a greater understanding of the interactions between mesoscale features within the southeast Cape Basin.

The numerous studies of the mesoscale features within the southeast Cape Basin have comprehensively shown the characteristic trajectory, diameter and translational speed of both cyclonic and anticyclonic eddies within the southeast Cape Basin (Boebel et al. 2003, Lutjeharms et al. 2003, Hall and Lutjeharms 2011, Dencausse et al. 2010). However, studies of these feature's depth structure and characteristics through the water column are scarce. Model studies provide observations through the water column however, the dynamic environment of southeast Cape Basin and lack of observations through the water column to validate the outputs increases the uncertainty of model solutions (Rubio et al. 2009). The KAPEX float experiment provides numerous *in situ* observations; however, the observations are temporally limited as the floats were advected through the southeast Cape Basin relatively quickly (Boebel et al. 1998). Similarly, van Aken (2003) presents *in situ* data of a ring shedding event providing observations through the water column; however, only captures a single event. The lack of observations through the water column decreases the ability to

accurately analyse the offshore mesoscale features and prevent definitive findings of the region's role in interocean exchange.

The literature focusing on the southeast Cape Basin have shown the region's influence on both the global ocean circulation, associated with interocean exchange, and the local marine ecosystem, associated with cross shelf transport. However, these studies have been limited to satellite observations (Dencausse et al. 2010, Hall and Lutjeharms. 2011), model observations (Rubio et al. 2009, Veitch et al. 2009) or short term hydrographical studies (Duncombe Rae et al. 1992, Boebel et al. 2003, Richardson 2007). The SAMBA mooring array provided a sustained period of high resolution, *in situ* observations through the upper water column. The high resolution, long term nature of the observations provided a unique opportunity to regularly observe the features and processes influencing both interocean exchange and coastal-open ocean exchanges. The long term *in situ* observations provided the opportunity to show the precise physical characteristics of the offshore mesoscale variability, improving the understanding and estimates of interocean exchange within the southeast Cape Basin. Similarly, the *in situ* observations of the connectivity between mesoscale features and the upwelling system provided the opportunity to improve estimates of cross shelf transport events and the associated biological impact.

---

# Chapter 3: Data and Methods

In order to describe the local circulation and characterise the features driving the circulation of the southeast Cape Basin, *in situ* Acoustic Doppler Current Profiler (ADCP) data from four deep sea moorings was used in conjunction with various remote sensing products and an eddy tracking algorithm. The *in situ* ADCP data was used to identify variations in the speed and direction of flow across the mooring array in order to describe the local circulation of the southeast Cape Basin. The ADCP data was then compared to the satellite products in order to identify the features driving the local circulation. The *in situ* observations were used to analyse the features driving the circulation. The analysis provided precise descriptions of the physical characteristics of these features. The ADCP data, eddy tracking algorithm and remote sensing products which included sea level anomaly (SLA), derived chlorophyll-a (Chl-a) and sea surface temperature (SST) were fully described. MATLAB R2014b was used for the manipulation, analysis and visualisation of the data.

## 3.1 ADCP Data

The SAMBA mooring array was initiated in 2013 when four Current and Pressure Recording Inverted Echo Sounders (CPIES) were deployed. In 2014, four deep sea moorings and two shallow water moorings were added to the array. This project will focus only on the four deep sea moorings.

The four deep sea moorings M7, M8, M9 and M10 were located at ~34.5°S on the 1000m, 2000m, 3000m and 4500m isobaths respectively (Figure 3.1). Each mooring was equipped with a 75kHz upward facing acoustic Doppler current profiler (ADCP) located at approximately 500m depth. The ADCPs measured the current speed and direction of the upper water column from ~500 to ~50m depth. The depth of each ADCP varied slightly for each mooring; the average vertical range is 582.85m to 54.85m, 588.55m to 60.65m, 410.25m to 42.95m, 413.78m to 45.38m for M7, M8, M9 and M10 respectively**.** The deep sea moorings were also equipped with SBE MicroCATs measuring temperature and salinity below 500m. However, this project will focus solely on the ADCP data from the deep sea moorings, thus focusing on describing local flow dynamics within the upper water column.

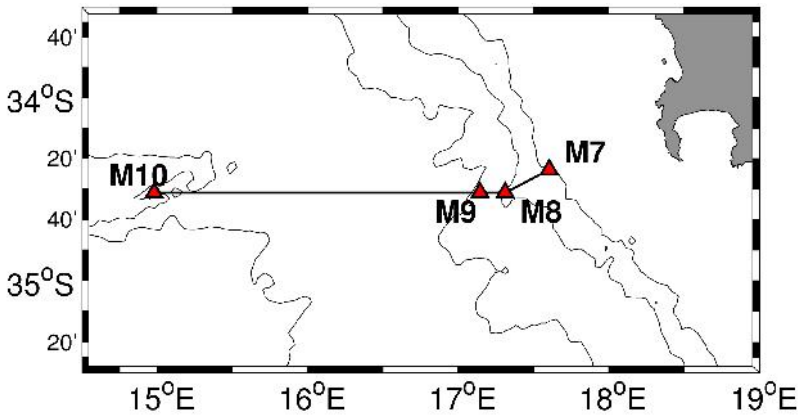


**Figure 3.1: Position of each deep sea mooring along the SAMBA mooring array. The moorings M7, M8, M9 and M10 are located at∼34.5°Son the 1000, 2000, 3000 and 4500m isobaths respectively.**

A total of 16 months of ADCP data, from 18 September 2014 to 1 December 2015, was analysed. The current speed and direction was sampled hourly which was then converted to daily averages (Figure 3.2). The daily averages negate sub-daily signals within the data resulting from tidal signals or extreme wave events. The ADCP data was not rotated relative to the coastline or bathymetry. Observations of current speed and direction from each mooring were analysed in order to identify the circulation at the position of the mooring array. Significant variations or anomalies in speed or direction of flow were of particular interest. The frequency and nature of these current events were then compared between each mooring in order to distinguish similarities or differences across the array. The timing of the events was then compared to remote sensing products in order to identify the spatial characteristics of the features responsible for the observed events or anomalies.

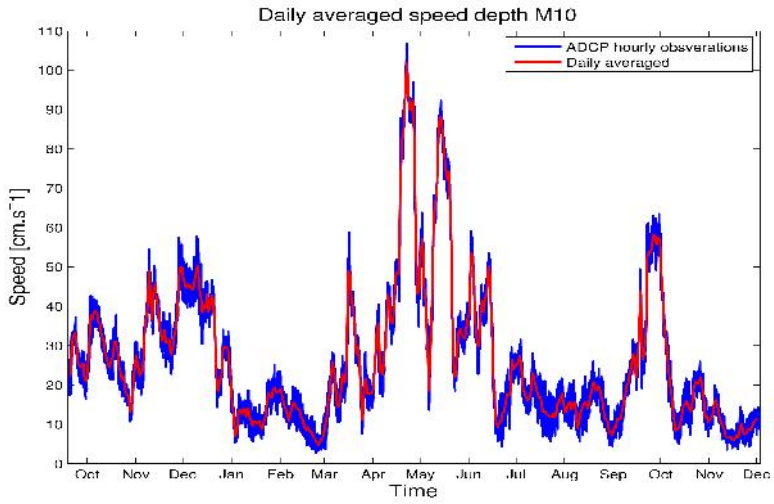


**Figure 3.2: The ADCP observations of speed sampled hourly (blue) averaged through depth for M10 overlaid with the same observations averaged daily (red). M10 was chosen as an example to show the smoothing effect of the daily averaging.**

## 3.2 Remote Sensing Data

### 3.2.1 Sea Level Anomalies (SLA)

The sea level anomaly (SLA) was used in order to identify mesoscale features within the Cape Basin. The product used was a level 4 (L4) merged, delayed time product which is distributed by Copernicus Marine Environment Monitoring Service (CMEMS). The product was previously distributed by Aviso+. The data processing protocols remained unchanged across both distributing platforms. The full description of the product (SEALEVEL_GLO_PHY_L4_REP_OBSERVATIONS_008_047) and processing system is available from the CMEMS website http://marine.copernicus.eu/. The SLA data was produced daily and had 0.25 degree spatial resolution. The altimetry product provided transient geostrophic velocities derived from the sea level anomalies observed. These derived velocities were compared with the *in situ* ADCP data and were necessary for the detection of mesoscale features using the eddy tracking algorithm (see section 3.3).

Altimetry, specifically sea level anomalies has been proven to reliably represent mesoscale variability within the Cape Basin (Rubio et al. 2009, Hall and Lutjeharms 2011). Mesoscale variability strongly influenced the offshore flow dynamics of the Cape Basin (section 2.5.3). Therefore, the timing of current events observed from the ADCP data were compared to the proximity of mesoscale features identified from the altimetry in order to explore the impact of mesoscale variability on the mooring array.

In order to illustrate the mesoscale variability within the Cape Basin the eddy kinetic energy was calculated using the Formula 1:

$$(1)\quad EKE = \frac{U'^2 + V'^2}{2}$$

The eddy kinetic energy was calculated per unit mass and therefore was presented in $cm^2.s^{-2}$. Where the terms U' and V' represent the zonal and meridional transient geostrophic velocity derived from the altimetry product described in section 3.2.1. The terms U' and V' are calculated as follows: $U' = U - \overline{U}$ and $V' = V - \overline{V}$; where $\overline{U}$ and $\overline{V}$ are the time-mean components of all the $U$ and $V$ components derived from the altimetry product mentioned above. Both the U- and V-component of the velocity is measured in $cm.s^{-1}$. The eddy kinetic energy was calculated daily and then averaged for the period of the ADCP data (17 September 2014 to 4 December 2015).

### 3.2.2 Sea Surface Temperature (SST)

The Group for High Resolution Sea Surface Temperature (GHRSST) provided a high resolution regional SST product for the greater Agulhas Region. The product is a level 4 L4 gridded SST product using the Advanced Very High Resolution Radiometer (AVHRR) platform with a 0.02 degree spatial resolution. The product was produced daily, and the full description is available at http://cersat.ifremer.fr/data/collections/ghrsst.

The sea surface temperature (SST) was used to highlight coastal upwelling within the Cape Basin due to the sharp temperature gradients typical of the upwelling system. This project used the SST gradient to identify the influence of the upwelling system on the circulation at the shelf edge. The contrast of the cold upwelled waters along the coast adjacent to the warmer waters offshore, associated with Agulhas Leakage, created a zonal temperature gradient. The temperature gradient created a strong density gradient driving equatorward flow (Veitch and Penven 2017). Therefore, a region of strong SST gradient suggested strong equatorward flow. The SST gradient was calculated using the partial derivatives (Formula 2). Where the spacing between points is the distance between the grid cells of the SST data described above.

$$\nabla F = \frac{\partial F}{\partial x}\hat{\imath} + \frac{\partial F}{\partial y}\hat{\jmath} \quad (2)$$

### 3.2.3 Chlorophyll-a (Chl-a)

Chlorophyll-a (Chl-a) was analysed by using a derived Chl-a product. The product used was reprocessed GLOBCOLOUR-OSS2015, a merged, level (L3) daily product combining MERIS, MODIS, SeaWifs and VIIRS platforms produced by the Global Ocean and Atlantic Satellite Observations (ACRI-ST company and distributed by Copernicus Marine Environment Monitoring Service (CMEMS). The full description is available at http://marine.copernicus.eu/. The product has a 0.04 degree spatial resolution. 5-day composites of the daily product were used to avoid excessive cloud cover without compromising the influence of local flows with shorter temporal scales. Chl-a can be used as a proxy for identifying upwelling regions as high Chl-a waters are a defining characteristic of upwelling regions. The distribution of Chl-a was analysed in order to identify the interactions between mesoscale variability and the upwelling system, as the high Chl-a waters characteristic of the upwelling system can be easily distinguished from low Chl-a waters offshore, essentially acting as a tracer.

### 3.3 Eddy detection scheme

The eddy detection scheme distinguished mesoscale eddies using Delayed Time Maps of Absolute Dynamic Topography (MADT) mapped daily on a $\frac{1}{4}°$ Mercator grid (Pujol et al. 2016). The full description of the scheme is available in Chaigneau et al. (2009). The eddy tracking scheme identifies relative local minima and maxima in the SLA product, fully described above, using a 1° x 1° moving window. The relative minima (maxima) are defined as the cyclonic (anticyclonic) eddy centres. For each eddy centre identified the algorithm searches for closed SSH contours using a $10^{-3}$ m increment. The outermost closed contour which includes the eddy centre is defined as the eddy edge. The algorithm only detects eddies with an amplitude of at least 2cm to account for the accuracy of the satellite product (Chaigneau et al. 2009).

The identification of eddy centres allows for coherent eddy features to be tracked. The eddy centre must be identified for at least 5 consecutive days. For this project eddies were only considered if they were detectable within a defined area, 13.5°E to 20°E and -39°S to -32°S, for at least 5 consecutive days (Figure 3.3).

The coherent structures identified by the eddy tracking scheme were overlaid onto the altimetry observations in order to identify mesoscale features in the vicinity of the SAMBA moorings. The timing of the mesoscale features was compared to current event within the ADCP data to identify any correlation. Similarly, the structures were overlaid onto SST and Chl-a observations in order to identify interactions between the mesoscale variability and the upwelling front.

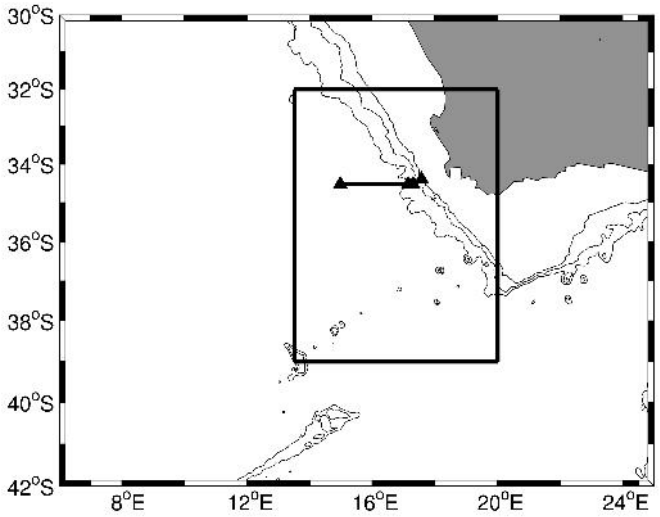


**Figure 3.3: The area, 13.5°E to 20°E and 39°S to 32°S, in which mesoscale features need to be detected for at least five consecutive days in order to be recordered by the eddy tracking scheme.**

### 3.4 Quantification of cross shelf transport

As previously stated, mesoscale eddies have been observed to interact with the southern Benguela upwelling front resulting in large filaments of upwelled water which extend from the shelf edge to the open ocean (Duncombe Rae et al. 1992). The combination of ADCP, SST and Chl-a data were used to identify an example of the interaction between mesoscale features and the upwelling front. A large filament of high Chl-a was observed over the position of the mooring array (Figure 4.18, 4.20). The position of the filament, over the mooring array, provided a unique opportunity to analyse the structure of the filament through the upper water column. Combining the *in situ* observations with satellite observations allowed for an estimation of the dimensions of the filament and in turn the quantification of the amount of water transferred from the shelf to the open ocean (Figure 4.18, 4.19, 4.21). The amount of water transferred was quantified using the total volume and volume transport.

The method used to determine the dimensions of the filament is fully described in section 4.4.2. The total volume of the filament was calculated using Formula 3 under the assumption the filament form a rectangular prism. The term volume is the total volume of the filament with units of $m^3$. The term width refers to the distance across a section of the filament used to define the width of the filament (section 4.4.2). The width is measured in meters (m). The term length is the distance from the edge continental shelf (1000m isobath) to the westward (offshore) extent of the filament (section 4.4.2). The length is measured in meters (m). The term depth is the distance to which the filament is observed to penetrate the water column. The depth of the filament is measured in meters (m).

(3) $$volume = length \times width \times depth$$

As for the dimensions used to calculate the total volume the determination of the dimensions used for calculating the volume transport is fully described in section 4.4.2. The volume transport across two sections within the filament was calculated using the Formula 4. The term Volume transport refers to the volume of water transported across a section within the filament measured in $m^3.s^{-1}$. The term U refers to U (zonal) component of the velocity measured by ADCP data. The U-component is measured in $cm.s^{-1}$. The term width refers to the distance measured across a section of the filament and is measured in meters (m). The term depth refers to the depth impacted by the filament. The depth is measured in meters (m).

(4) $$volume\ transport = U \times (width \times depth)$$

# Chapter 4: Results

The SAMBA mooring array was ideally positioned to capture both the offshore circulation associated with mesoscale activity and the circulation along the shelf edge associated with the coastal upwelling. The ADPC data was combined with satellite observations and an eddy tracking scheme to describe both offshore and shelf edge circulation as well as the oceanographic features driving the circulation. The ADCP data was used to analyse these features in an attempt to improve the understanding of how these features impact both interocean exchange and coastal-open ocean exchange. The findings are presented as follows:

- The ADCP data and satellite observations were used to show the differences in the circulation across the mooring array. In particular, the differences between the offshore circulation and the circulation observed at the shelf edge were highlighted.
- The satellite and ADCP observations were used to identify the features driving the circulation along the shelf edge.
- The eddy tracking scheme was used in conjunction with the ADCP data to describe the physical characteristics of mesoscale variability and individual mesoscale features influencing the mooring array.
- An example of the interactions between offshore mesoscale features and the upwelling system was identified and its characteristics were analysed by combining the *in situ* ADCP and satellite observations.

## 4.1 The local circulation at the position of the mooring array

### 4.1.1 Variation in Speed

The variation in current speed across the mooring array was assessed using a time series of speed, averaged daily and through the upper water column, (Figure 4.1) recorded at each mooring (Table 1).

M7 was the closest inshore mooring, located on the 1000m isobath (Figure 3.1). A mean speed of 15.60cm.s$^{-1}$ with a standard deviation of ±6.43cm.s$^{-1}$ was observed at M7 over the full deployment period from 18 September 2014 to 1 December 2015 (Table 1). Throughout the time series there were a number of events characterised by short periods of increased speed substantially higher than the mean (Figure 4.1A). These events were more frequently observed and were associated with higher speed during the first half of the time series, from November 2014 to May 2015 (Figure 4.1A).

M8, located on the 2000m isobath (Figure 3.1), showed a mean speed of 18.93cm.s$^{-1}$ with a standard deviation of ±10.72cm.s$^{-1}$ over the full deployment period (Table 1). Similar to M7 there were a number of increased speed events throughout the time series at M8 (Figure 4.1B). These events also occurred more frequently in the first half of the time series (September 2014 to April 2015) compared to the second half of the time series (May 2015 to December 2015), as observed at M7. The event observed in March 2015 was notable as it was substantially higher in speed when compared to the other events observed at M8 (Figure 4.1B) and those seen at M7 (Figure 4.1A).

M9 was in close proximity to M8 situated on the 3000m isobath (Figure 3.1). A mean speed of 22.77cm.s$^{-1}$ with a standard deviation of ±13.31cm.s$^{-1}$ was calculated at M9 from 18 September 2014 to 1 December 2015. Again, high speed, short period events were present throughout the time series at M9 (Figure 4.1C). The events visible at M9 (Figure 4.1C) were comparable in speed and timing to the events seen at M8 (Figure 4.1B) resulting in a strong resemblance between the two time series. The extreme event observed in March 2015 at M8 was also clearly visible at M9, however, the maximum speed at M9 (100cm.s$^{-1}$) was greater than that at M8 (80cm.s$^{-1}$)

M10 was the furthest mooring offshore and was positioned on the 4500m isobath (Figure 3.1). M10 showed the highest mean (26.47cm.s$^{-1}$) and standard deviation (±17.93cm.s$^{-1}$) compared to the other moorings (Table 1). Similar to the other moorings, high speed events were also observed throughout the time series of M10 (Figure 4.1D). These events occurred relatively frequently throughout the time series. In contrast to the timing of events observed at the other moorings two events in May 2015 and June 2015, displayed speeds considerably larger than the rest of the events (Figure 4.1D).

There was a clear increase in the mean speed and standard deviation from M7, closest to the shelf, to M10, furthest offshore (Table 1). The increased mean speed and standard deviations across the moorings was a result of the short time scale, high speed events, which increased from M7 to M10 as illustrated by Figure 4.1A-D. There was a clear increase in both the number of these high speed events and the intensity of the high speed events from M7 to M10. The increase in the number and intensity of these events could be visually observed in the time series (Figure 4.1A-D, Figure 4.2C).

| | Mean Spd (cm.s$^{-1}$) | Mean U-component (cm.s$^{-1}$) | Mean V-component (cm.s$^{-1}$) | [Maximum Minimum] (cm.s$^{-1}$) |
|---|---|---|---|---|
| M7 | 15.60(±6.43) | -2.15(±13.32) | -5.67(±8.40) | [2.75 to 37.29] |
| M8 | 18.93(±10.72) | 0.45(±17.82) | -3.22(±12.05) | [2.91 to 93.62] |
| M9 | 22.77(±13.31) | 0.64(±20.88) | -2.85(±15.84) | [3.16 to 110.87] |
| M10 | 26.47(±17.93) | -7.53(±21.33) | 1.59(±22.55) | [2.25 to 105.29] |

**Table 1: Shows the mean of the resultant speed, U-component and V-component as well as the maximum and minimum of the resultant speed. The resultant speed, U-component and V-component is averaged through the upper water column from 18 Sep 2014 to 1 Dec 2015. The standard deviation is shown in brackets**

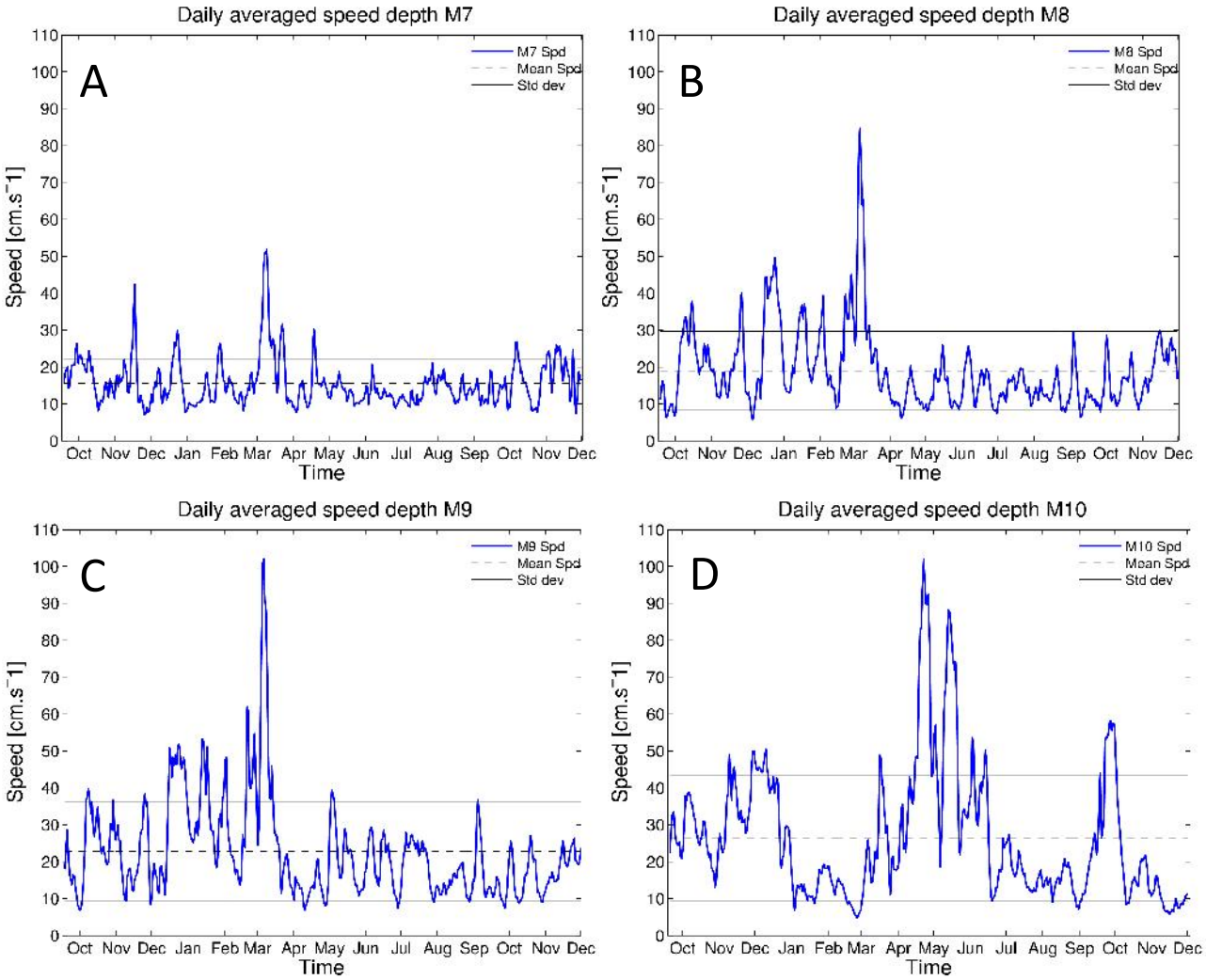


**Figure 4.1: Panel A, B, C and D show time series of current speed observed at M7, M8, M9 and M10 respectively. ADCP observations are averaged daily and through depth (from ~50m to ~500m) from 18 Sep 2014 to 1 Dec 2015. The mean speed of each mooring is represented by the dashed line.**

In order to further investigate the nature of the high speed events observed at each mooring (Figure 4.1A-D) the U- and V-components were analysed. Figure 4.2 showed a combined time series of U- and V-components for each mooring illustrating the characteristics of the flow associated with each of the high speed events.

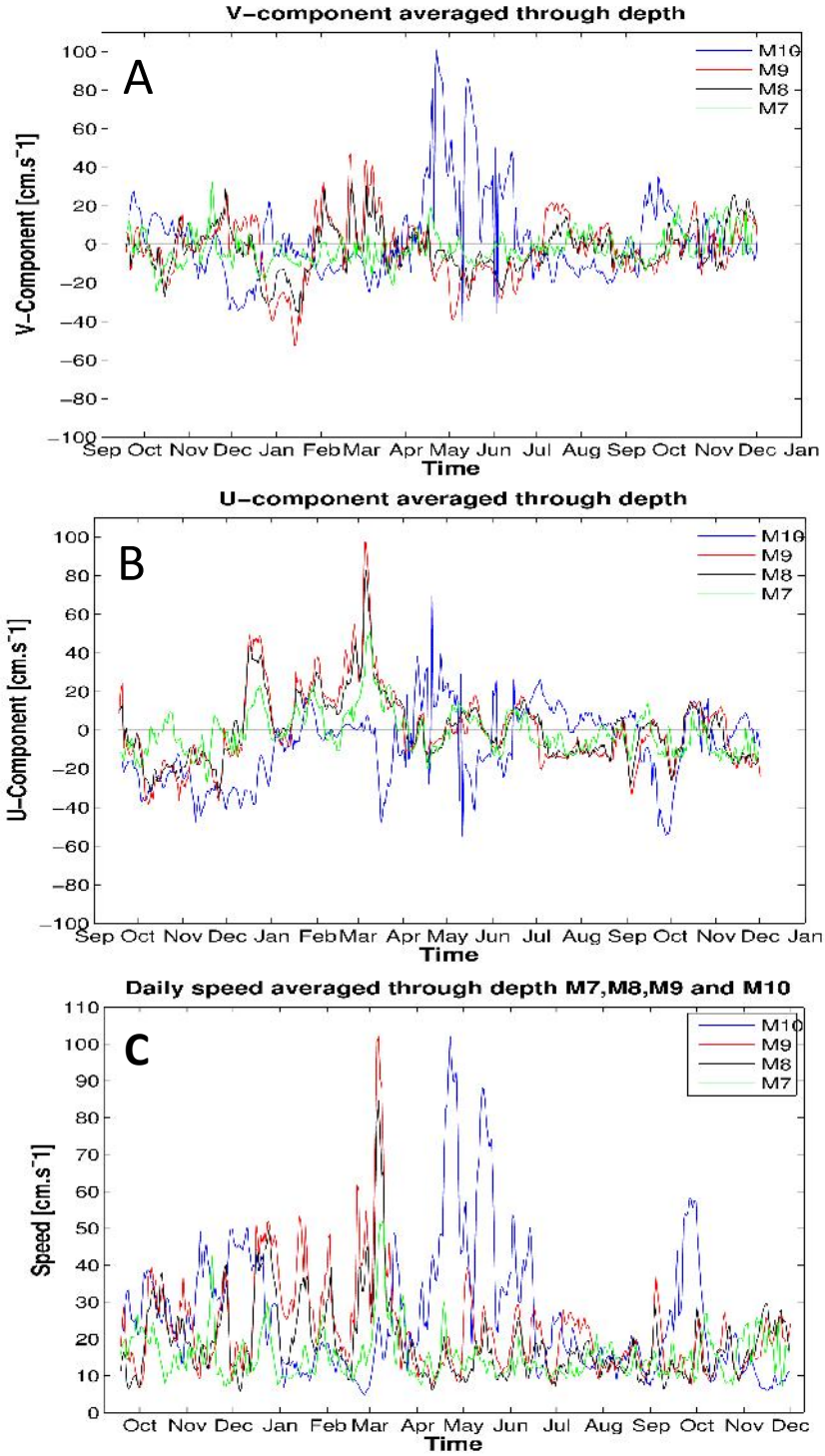


**Figure 4.2: Combined time series of U-component, V-component and observed speed averaged daily and through depth. Panel A shows the V-component, Panel B shows the U-component and Panel C shows the resultant speed. The solid horizontal black line represents zero and is used as a reference line.**

The U (zonal) component of the velocity recorded at M7 (Figure 4.2A) was similar to the speed recorded during the high speed events observed from December 2014 to April 2015 (Figure 4.1A). The similarity in the U-velocity component indicated zonal flows were important for the high speed events during this period. The V (meridional) velocity component calculated for M7 was similar to the speed observed for the beginning (September 2014 to December 2014) and the end (July 2015 to December 2015) of the time series (Figure 4.2B); demonstrating meridional flows were important during these periods. Interestingly, the U-component (Figure 4.2A) for M7 showed a strong resemblance to the U-component of M8 and M9 which was not evident in the V-component. The V-component at M7 was out of phase with M8 and M9 indicating a different timing of events (Figure 4.2B).

The time series of the U-component (Figure 4.2A) for both M8 and M9 showed a strong resemblance to the respective time series of resultant speed (Figure 4.1B, 4.1C) from 18 September 2014 to April 2015. The U-component (both positive and negative) was comparable to the resultant speed indicating a strong zonal component for this period (Figure 4.2A). Conversely the V-component (Figure 4.2B) showed resemblance to the high speed events observed in December 2015 and May 2015 (Figure 4.1B, 4.1C) indicating the events were dominated by meridional flows. The U- and V-components at M8 and M9 both showed a strong resemblance indicating a similar timing of events at both moorings (Figure 4.2A, 11B). The U-components of the extreme event observed in March 2015 (Figure 4.1B, 4.1C) was similar to the speed of the event at both M8 and M9 (Figure 4.2A, 11B); indicating the event was dominated by zonal flows.

The U-component observed at M10 was similar to the speed of high speed events from September 2014 to April 2015 and again in September 2015 demonstrating the dominance of zonal flow during these events (Figure 4.2A). Notably the two large events during May 2015 and June 2015 showed a low U-component and high V-component signifying meridional flows were more important than zonal flows during these two events. These high speed events indicated an oscillation from positive to negative U- and V-components during the extreme events; this oscillation was not shown in the events identified in M7, M8 and M9 (Figure 4.2A, 4.2B).

### 4.1.2 Variation in Direction

The variation in the direction of flow across the mooring array was analysed using current rose diagrams. The current roses represented the daily averaged direction of flow at each mooring as a percentage of the total direction of flow over the observed time period. This percentage was depicted by the circular dashed line (5% and 10%). The speed associated with each direction of flow was represented by the colour map and legend. The speed and direction of flow were averaged through

the upper water column from ~50 to ~500m depth. The direction of flow was depicted in the oceanographic convention with coloured bars pointing in the direction of flow.

The direction of flow averaged through depth at M7 was predominantly south eastward and south westward (Figure 4.3A). North westward flows were frequent but contribute much less to the total direction compared to the southeast and south westward flows. North eastward flows were not observed at M7. The speed of flow, averaged through depth, recorded at M7 was predominantly between 10cm.s$^{-1}$ and 20cm.s$^{-1}$. High speed flows (>30cm.s$^{-1}$) were only observed in the south eastward and north westward direction.

M8 indicated more variability in the directions of flow (Figure 4.3B), showing no predominant flow direction. Notably there was an absence of due northward flows. There was substantially more high speed (>30cm.s$^{-1}$) flows compared to M7 (Figure 4.3A). These flows were present for most flow directions but were more frequently observed in the north eastward and south eastward direction.

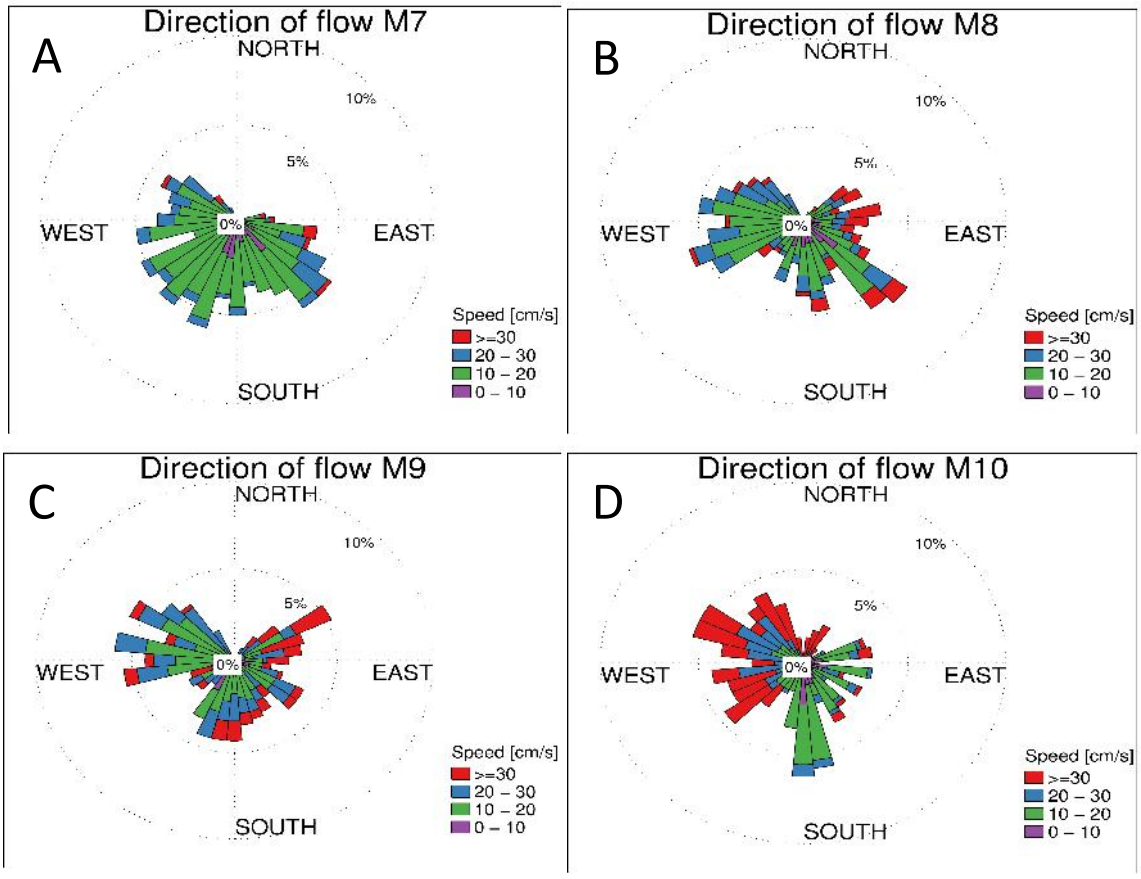


**Figure 4.3: Current roses depicting daily direction of flow averaged through depth. Panel A, B, C and D show the direction of flow for M7, M8, M9 and M10 respectively. The current roses are depicted using the oceanographic convention with coloured bars pointing in the direction of flow.**

As observed at M8 (Figure 4.3B) the direction of flow at M9 (Figure 4.3C) showed substantial variation in the direction of flow, with an absence of due north flows. There was a slight increase in high speed (>30m.$s^{-1}$) flows shown at M9 when compared to M8. The high speeds at M9 were mostly concentrated in the north eastward direction. A number of high speed flows in the southward and south eastward direction was also observed.

Similar to M8 and M9, M10 (Figure 4.3D) also displayed variable direction of flow. However, in contrast to M8 and M9 there were due north flows present at M10. Interestingly, a large portion of the flow observed at M10 was in a southward direction, which was associated with low speeds (10cm.$s^{-1}$ to 20cm.$s^{-1}$). There were substantially more observations of high speed flows (>30cm.$s^{-1}$) at M10 compared to the other moorings. The high speeds were generally associated with south westward, westward and north westward flows

The current roses showed a similar pattern to the variation of speed across the mooring array (Figure 4.1, Table 1). There was a clear increase in the number of high speed flows from M7, closest inshore, to M10, furthest offshore. In addition to the increased high speed flows, the current roses showed increased variability in the direction of flow from M7 which showed the least variation in direction of flow to M10 which showed the most variable direction of flow.

### 4.1.3 Investigating the features driving the local circulation

Mesoscale variability is known to substantially influence the local circulation of southeast Cape Basin (Boebel et al. 2003, Richardson 2007, Hall and Lutjeharms 2011). Mesoscale features are generally identified by anomalies in the sea level; therefore, the *in situ* ADCP data was compared to altimetry in order to investigate if mesoscale features were responsible for the differences in speed and direction observed across the mooring array.

The geostrophic velocities derived from the SLA were used to calculate the eddy kinetic energy (EKE). The EKE describes the energy of the ocean associated with turbulent or eddy flows. Within the southeast Cape Basin, low EKE values (100 $cm^2/s^{-2}$) were observed over the shelf in waters shallower than 1000m. In contrast, much higher EKE (400$cm^2/s^{-2}$) was observed offshore (Figure 4.4). The high offshore EKE was connected to the high EKE observed in the region of the Agulhas retroflection indicating the source offshore EKE originated within the retroflection area (Figure 4.4). Relatively high EKE (200- 250$cm^2/s^{-2}$) was observed along the shelf edge north of the mooring array. The high EKE along the shelf edge showed a clear separation from the cohesive pool of EKE offshore. The separation between high offshore EKE and EKE observed along the shelf edge indicated an additional source of EKE along the shelf edge.

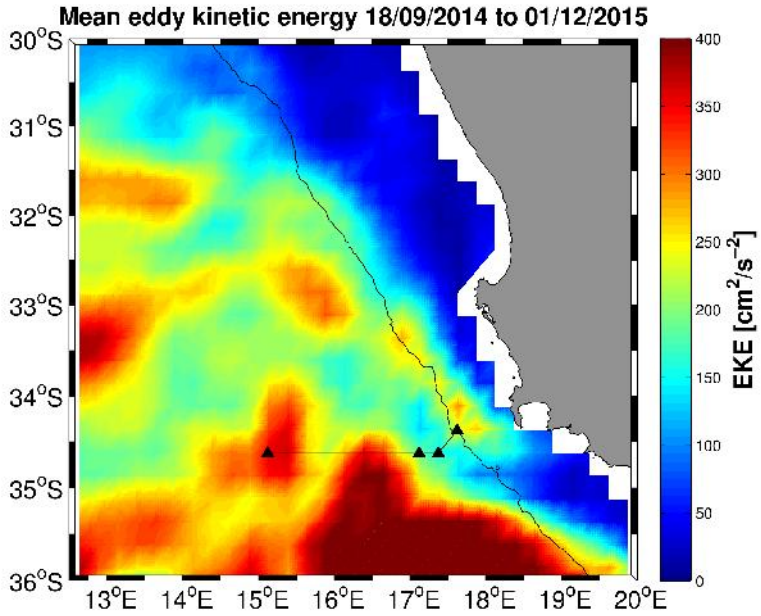


**Figure 4.4: Mean eddy kinetic energy ($cm^2.s^{-2}$) within the southeast Cape Basin from 18/09/2014 to 1/12/2015. The mooring array and positions are represented by the black line and triangles respectively. The shelf edge is depicted 1000m contour.**

M10 was located in the region of high offshore EKE (Figure 4.4) and therefore was most likely to be influenced by mesoscale features which originate from the retroflection region. M9 and M8 were located on the edge of the band of high offshore EKE (Figure 4.4), and were therefore

less likely to be impacted by mesoscale activity. The position of M8 and M9 between the high offshore EKE and the elevated EKE observed along the shelf edge suggested that these moorings should have observed mesoscale variability originating from both locations. M7 was much less likely to be affected by the high offshore EKE due to its location on the shelf edge. However, it may have been impacted by the mesoscale features associated with the relatively high EKE observed along the shelf edge.

The correlation between the geostrophic velocities derived from altimetry and the *in situ* ACDP data describes the relationship between the two datasets (Table 2). The U- and V-components of the geostrophic velocities derived from sea level anomaly (SLA) data were compared to the U- and V-components calculated from the surface ADCP data ($\pm$50m) at each mooring. A correlation, close to 1, showed a strong relationship; and would indicate the ADCP data displays a similar variation and pattern to the satellite derived velocities. Conversely a low correlation, close to 0, indicated a weaker relationship between the flow observed from the ADCP and satellite data. Each correlation has been shown to be significant with a p-value of less than 0.001 calculated at a confidence interval of 95%.

| | Correlation of U-velocity component with SLA [p-value] | Correlation of V-velocity component with SLA [p-value] |
|---|---|---|
| M7 | 0.47 [<0.0001] | 0.41 [<0.0001] |
| M8 | 0.80 [<0.0001] | 0.62 [<0.0001] |
| M9 | 0.79 [<0.0001] | 0.74 [<0.0001] |
| M10 | 0.79 [<0.0001] | 0.84 [<0.0001] |

**Table 2: The correlation of U- and V- velocity components of M7, M8, M9 and M10 at the surface bin (~50m) and U and V geostrophic velocity derived from gridded sea level anomaly (1/4° AVISO). The p-values calculated at a 95% confidence interval are present in square brackets.**

The correlation of the U- and V-components at M7 were substantially lower than the correlation calculated at M8, M9 and M10 (Table 1). However, the correlations for the U-components (0.47) and the V-components (0.41) were not negligible and were shown to be significant ($p<0.0001$) which suggested there was some agreement between the datasets. The relatively weak correlation indicated that there were features impacting M7, causing variation in flow, which were not captured by the altimetry. The slightly stronger correlation in U-component than V-component at M7 may suggest that these features were associated with meridional flows.

M8 showed a much stronger correlation in the U-component (0.80) and in the V-component (0.62). The positive correlation in the U-component was the highest observed across the mooring array (Table 2), which showed the flow recorded at M8 is in good agreement with the altimetry. As for M7, the slightly lower correlation of the V-component at M8 suggested that there were features impacting the flow recorded at M8 which were not observed by the altimetry and that these features induced meridional flows.

Similar to M8, a strong correlation in the U-component (0.79) and in the V-component (0.74) was observed for M9 (Table 2), which showed a strong agreement with the altimetry data. As for M7 and M8 there was a slightly lower correlation in the V-component. However, this correlation in the V-component was much higher than that at M8 and M7 showing there was a strong relationship with the altimetry in both U- and V-component at M9.

M10 showed a strong correlation in both the U-component (0.79) and the V-component (0.84) (Table 1). The strong correlation showed the variation in flow recorded at M10 was in good agreement with the altimetry data. There was a slight decrease in the correlation for the U-component, but similar to M9, the difference was relatively small.

The differences in the correlations between the moorings showed a similar pattern to the variation in speed and direction across the mooring array. M10, furthest offshore, indicated a high correlation with the derived velocities for the U- and V-component. M8 and M9 both recorded a high correlation for the U-component and lower correlations in the V-component. M8 showed a lower V-component than M9. M7, positioned closest to the shelf, showed the lowest correlation in both the U- and V-components. The variation in the correlation with the altimetry across the mooring array was in good agreement with EKE within the region; with the highest EKE observed further offshore and the lowest EKE observed closest to the shelf edge (Figure 4.4).

The variation in speed (Figure 4.1, Table 1), direction (Figure 4.3) and the comparison with the altimetry (Figure 4.4, Table 2) indicated distinct differences in flow dynamics observed across the mooring array. M8, M9, and M10 seemed to be substantially influenced by offshore dynamics driven by the band of high EKE (Figure 4.4, Table 2). In contrast, M7 seemed to be influenced by features along the shelf-edge, not observed by the altimetry, and to a lesser extent by offshore dynamics (Figure 4.4, Table 2).

## 4.2 Investigating the impact of mesoscale variability on the local circulation

### 4.2.1 Characterising the mesoscale variability

The variation in speed (Figure 4.1, Table 1) and direction (Figure 4.3) observed at M8, M9 and M10 was strongly driven by the offshore mesoscale variability (Figure 4.4, Table 2). Therefore, the variation in speed and direction through the upper water column (±50m to ±500m) at M8, M9 and M10 was analysed in order to analyse the impact of the offshore mesoscale features on the mooring array.

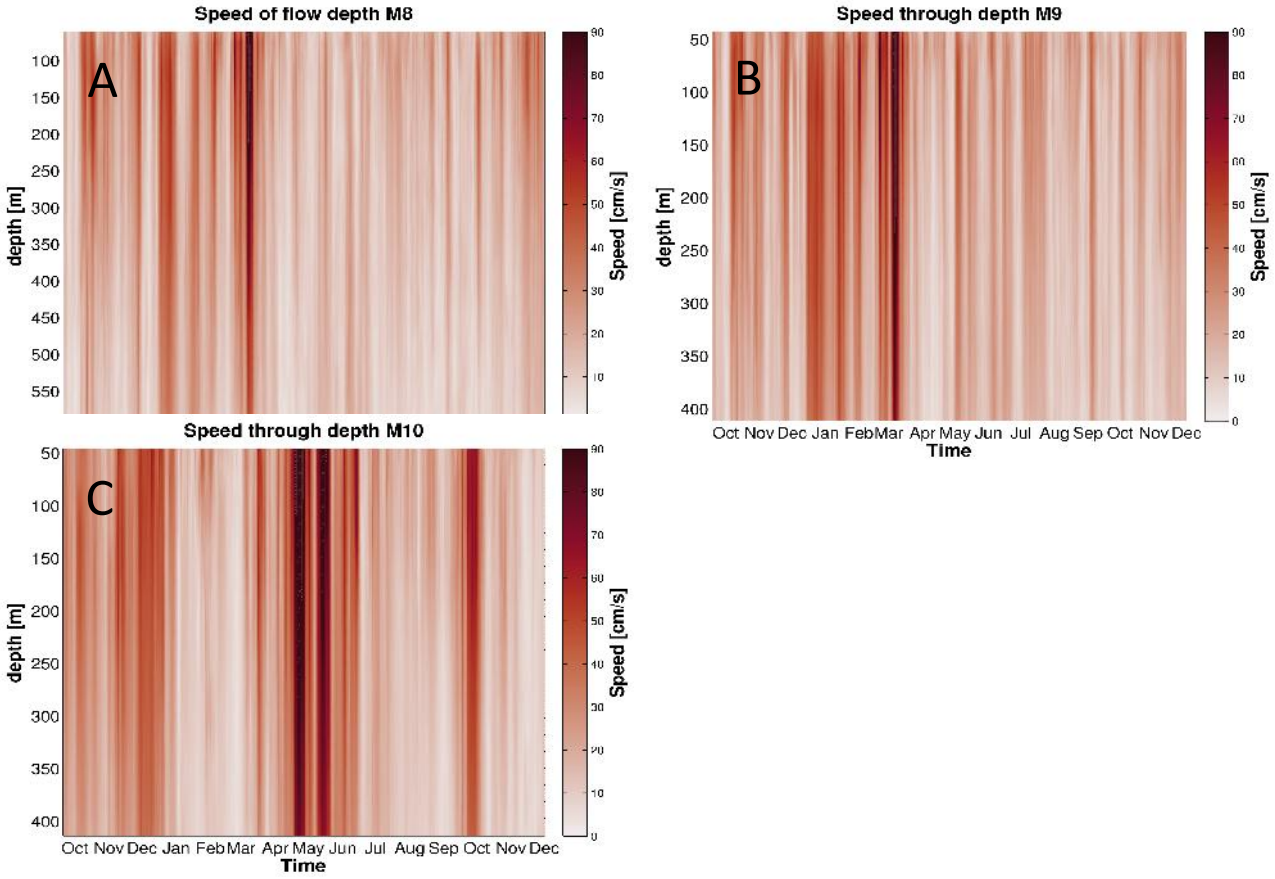


**Figure 4.5: Speed of flow [cm/s] in the upper 550m, 400m and 400m observed at M8, M9 and M10 respectively. Panel A, B and C show the speed of flow for M8, M9 and M10**

The speed through depth at M8, M9 and M10 highlighted the timing of the high speed events and the depth to which each high speed event impacted the water column. The pattern of high speed events observed at M8 and M9 were similar (Figure 4.1B, 4.1C); a higher number of events from September 2014 to April 2015 and fewer events from May 2015 to December 2015 (Figure 4.5A, 4.5B). The high speed events observed at M8 and M9 penetrated through the upper water column to 550m and 400m depth respectively (Figure 4.5A, 4.5B). Similarly, the extreme event observed in March 2015 (Figure

4.1B, 4.1C) penetrated through the upper water column to a depth of 550m and 400m at M8 and M9 respectively (Figure 4.5A, 4.5B).

High speed events were observed relatively frequently throughout the time series and through the upper 400m of the water column at M10 (Figure 4.1D, Figure 4.5C). The high speed events all penetrated to a depth of at least 400m (Figure 4.5C). The two extreme high speed events, May 2015, June 2015, also penetrated through the upper water column to a depth of at least 400m (Figure 4.5C). These two high speed events showed barotropic signal, as the speed showed no change with increasing depth.

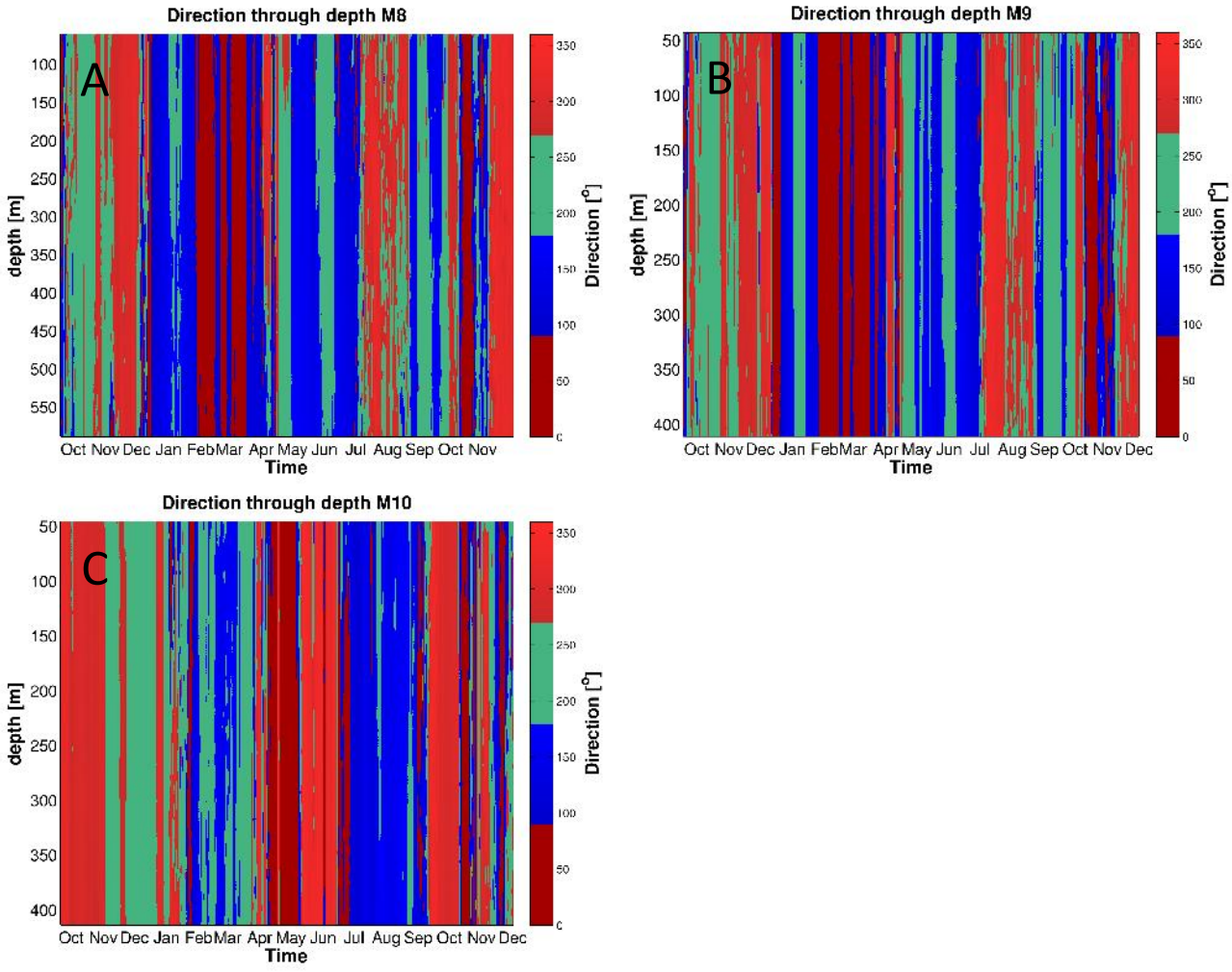


**Figure 4.6: Direction of flow [°] in the upper 550m, 400m and 400m observed at M8, M9 and M10 respectively. Panel A, B and C show the speed of flow for M8, M9 and M10.**

The direction of flow through depth observed at M8 and M9 showed a variable direction of flow for the high speed events (Figure 4.6A, 4.6B). The direction showed the same pattern as the speed (Figure

4.5A, 4.5B) as all the events penetrated through the water column to a depth of 550m and 400m respectively (Figure 4.6A, 4.6B).

Similar to M8 and M9, the high speed events at M10 were not associated with a specific direction; showing variable direction of flow, which penetrated through the upper water column to a depth of 400m (Figure 4.6C).

The similarity in both the speed and direction of the high speed events observed at M8, M9 and M10, through the upper water column, provided a synopsis of the impact of mesoscale features on the mooring array. The high speed events associated with mesoscale features were shown to penetrate through the upper water column to at least 400m and were associated with variable direction of flow.

### 4.2.2 Analysing individual mesoscale features

The ability of the mooring array to capture the influence of mesoscale features (Figure 4.5, Figure 4.6) associated with the band of high EKE offshore (Figure 4.4) allowed for the individual features to be identified and described. The SLA and the eddy tracking algorithm described by section 3.3.1 were used to highlight and characterise the impact of individual mesoscale features which passed over the mooring array.

The eddy tracking algorithm identified a total of 38 anticyclonic and 33 cyclonic eddies from 18/09/2014 to 01/12/2015 within the region (Figure 4.7A). The initial position of eddy trajectories showed a high number of cyclonic eddies along the continental shelf with a smaller number of cyclonic eddies first detected over the Agulhas Bank (Figure 4.7D). A large portion of the anticyclonic eddies were initially detected within the retroflection area (Figure 4.7D). Additionally, a substantial number of cyclonic and anticyclonic eddies were first detected offshore of the shelf edge and north of the retroflection region; not associated with large scale oceanographic and topographic features (Figure 4.7D).

The trajectories observed for both the cyclonic and anticyclonic eddies were highly erratic highlighting the turbulent nature of the southeast Cape Basin (Figure 4.7A). Despite the high variability of the trajectories, the cyclonic eddies were shown to have a general west to south westward drift (Figure 4.7B), while the anticyclonic eddies indicated a general west north westward drift (Figure 4.7C).

Each of the high speed events (defined as a speed greater than two standard deviations from the mean speed) observed at M8, M9 and M10 was associated with the 8 anticyclonic and 6 cyclonic eddies identified by the eddy tracking algorithm. Each of the high speed events corresponded to a cyclonic or anticyclonic eddy in close proximity to the mooring. Three case studies were selected and are

presented below. Two cyclonic eddies and one anticyclonic eddy, were analysed through the upper water column to show the physical characteristics of each features.

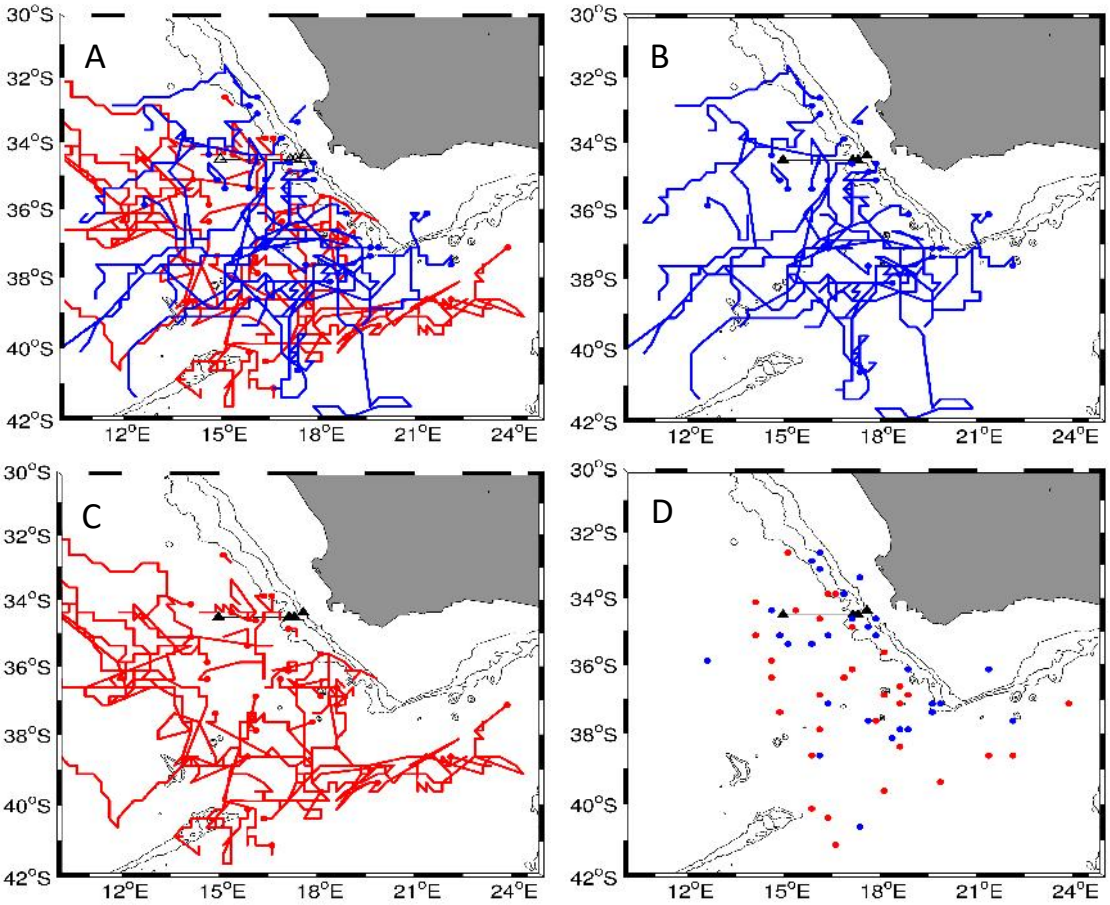


**Figure 4.7: The trajectories and positions of initial detection for all eddies identified using the eddy tracking scheme from the 18/09/2014 to 01/12/2015. Panel A represents all eddies identified. The anticyclonic eddy tracks are represented in red and cyclonic eddies in blue. Panel B shows only the cyclonic eddies. Panel C shows only the anticyclonic eddies. Panel D presents the position each anticyclonic and cyclonic eddy was first detected.**

### 4.2.2.1 Mature cyclonic shelf eddy

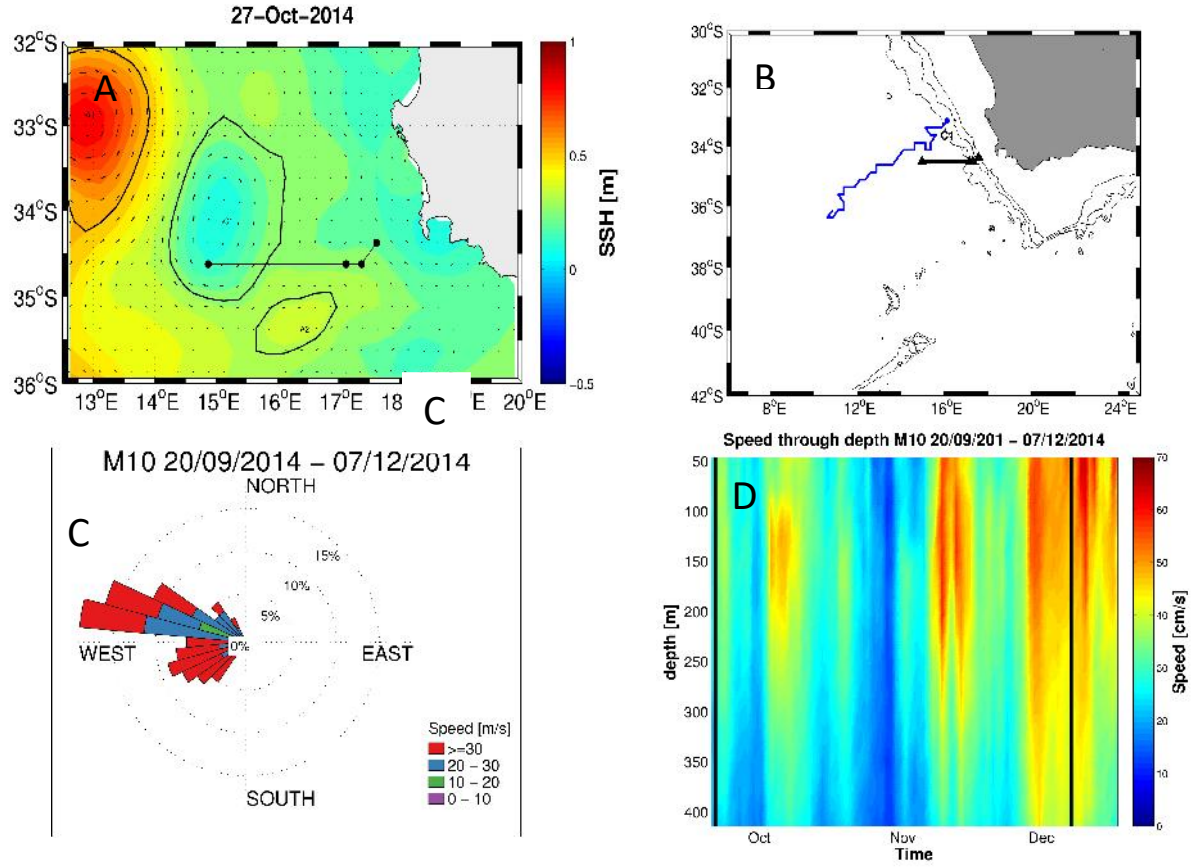


**Figure 4.8: The impact of a mature cyclonic eddy on M10. Panel A shows a SLA snapshot of cyclonic eddy (C1) at the position of M10. Panel B shows the trajectory of the cyclonic eddy. Panel C shows the current rose for the period the cyclonic eddy impacts M10. Panel D shows speed through depth for the period the cyclonic eddy is observed to impact M10. The current roses are depicted using the oceanographic convention with coloured bars pointing in the direction of flow.**

The initial detection and trajectory of the cyclonic eddy (C1) showed C1 was formed along the continental shelf edge north of the mooring array and moved south westward across the southeast Cape Basin (Figure 4.8B). C1 was first detected by the eddy tracking scheme on the 3/07/2014 and first impacted the mooring array on the 20/09/2014 indicating the eddy was well established (detected for 117 days) by the time it impacted M10 and therefore, was considered a mature feature. The interaction of C1 on M10 was clearly identified by the SLA snapshot (Figure 4.8A). Both the SLA and the *in situ* data showed C1 impacted the flow at M10 from 20/09/2014 to 07/12/2014. The current rose indicated a strong westward flow for the observed period (Figure 4.8C).

The westward flow is in agreement with the rotation of cyclonic eddies and therefore can be solely attributed to C1. The mean speed of flow for the observed period was 32.33cm.s$^{-1}$ with a maximum speed of 50.14cm.s$^{-1}$. The speed of flow penetrated through the water column to a depth of 400m; however, each event showed a decrease in speed with depth. The speed through depth showed an

oscillating signal, with periods of increase and decreased speed during the period C1 was over the position of M10. The oscillating signal was most likely a result of small changes in position of C1 relative to M10.

### 4.2.2.2 Immature cyclonic shelf eddy

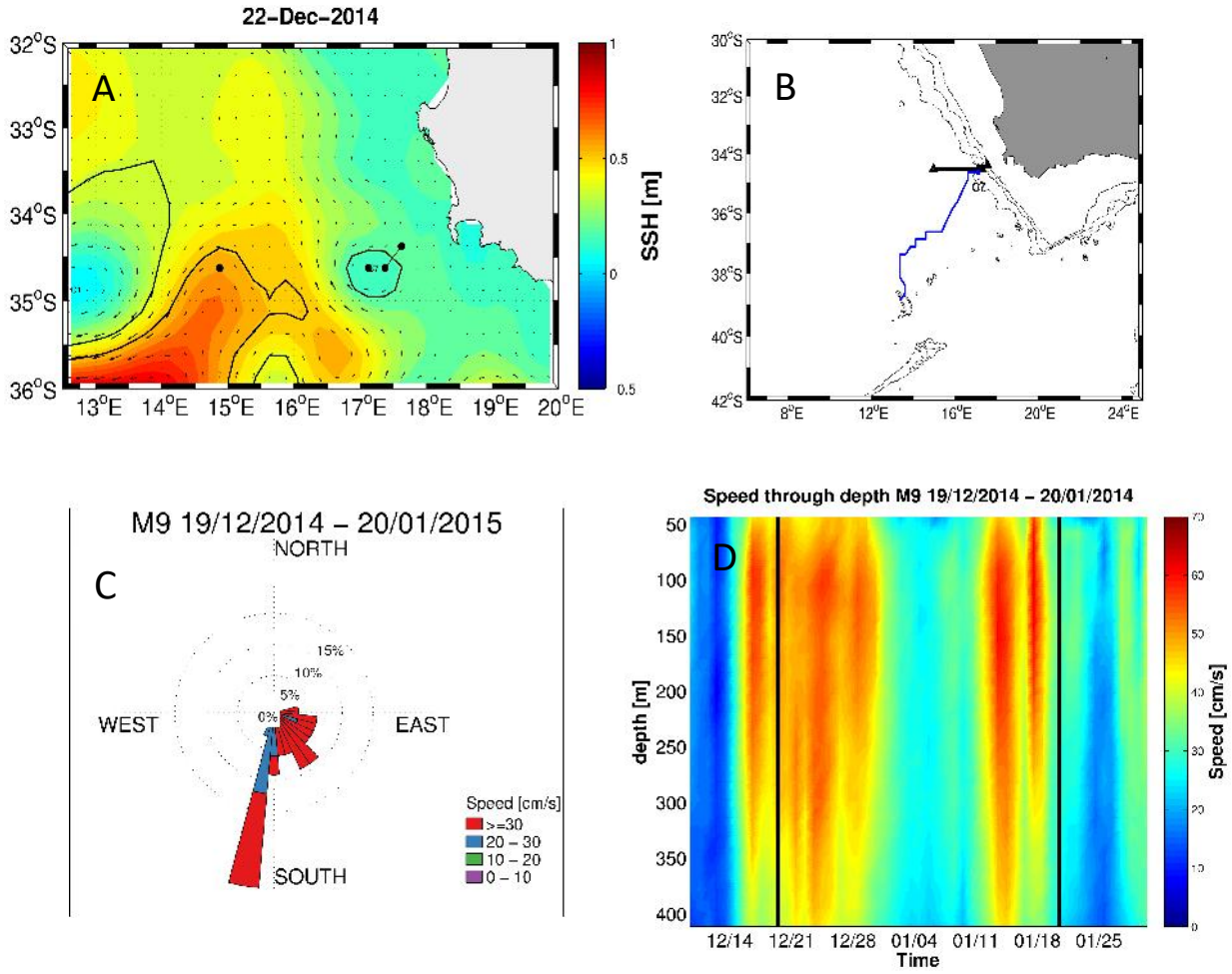


**Figure 4.9: The impact of an immature cyclonic eddy on M9. Panel A shows a SLA snapshot of cyclonic eddy (C7) impacting M9. Panel B shows the trajectory of the cyclonic eddy. Panel C shows the current rose for the period the cyclonic eddy impacts M9. Panel D shows the speed through depth for the period the cyclonic impacts the M9. The current roses are depicted using the oceanographic convention with coloured bars pointing in the direction of flow.**

The trajectory of the cyclonic eddy (C7) showed C7 was formed along the shelf edge (Figure 4.9B) as was the case for C1 (Figure 4.8B). The trajectory indicated a south westward movement into the interior of the southeast Cape Basin. C7 was first detected on the 19/12/2014 in close proximity to the position of M8 and M9. The impact of C7 on the flow at M9 and the eddy's first detection was simultaneous; indicating C7 had only recently been formed when it impacted the mooring array (Figure 4.9B). The current rose from M9 indicated a strong south to south eastward flow (Figure 4.9C),

which was consistent with the cyclonic rotation associated with C7. The difference in the direction of flow recorded at M9 resulting from C7 (Figure 4.9C) compared to direction of flow recorded at M10 resulting from C1 (Figure 4.9C) was a result of the respective eddies having different positions relative to the mooring array. C7 was positioned slightly west of M9 (Figure 4.9A) while C1 was positioned north of M10 (Figure 4.8A). The mean speed recorded during the period C7 impacted M9 was 39.85cm.s$^{-1}$ with a maximum of 53.16 cm.s$^{-1}$. The speed through depth showed C7 impacted speed of flow to 400m depth (Figure 4.9D). C7 showed the same oscillating signal of increased and decreased periods of speed observed for C1 (Figure 4.9D); but only showed two periods of increased speed which was possibly a result of the shortened period over which the eddy interacted with the mooring array.

### 4.2.2.3 Mature anticyclonic eddy

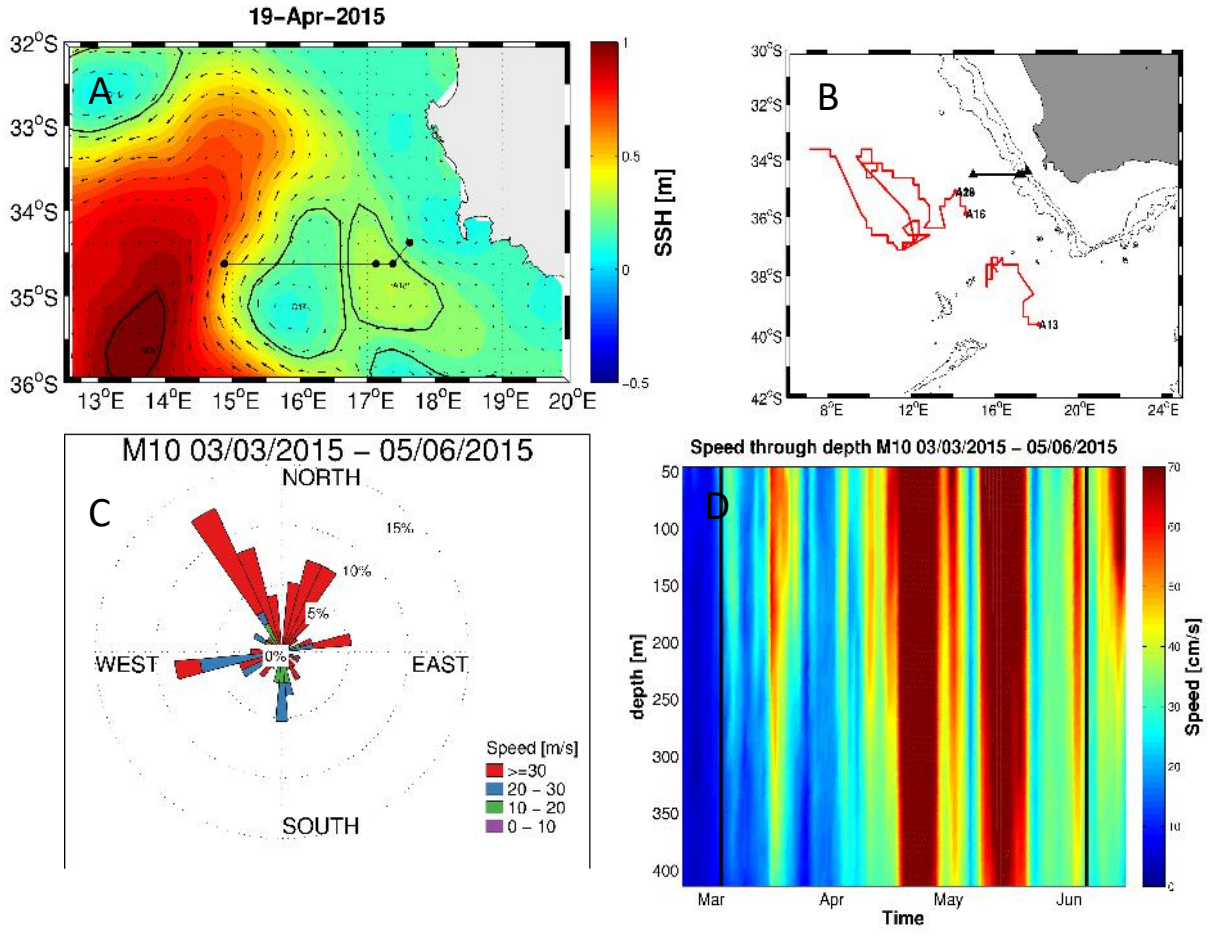


**Figure 4.10: The impact of a mature anticyclonic eddy on M10. Panel A shows a SLA snapshot of anticyclonic eddy impacting M10. Panel B shows the trajectory of the anticyclonic eddy. Panel C displays the current rose for the period the cyclonic eddy impacts M10. Panel D shows the speed through depth for the period the anticyclonic eddy impacts M10. The current roses are depicted using the oceanographic convention with coloured bars pointing in the direction of flow.**

The SLA snapshot (Figure 4.10A) indicated a large anticyclonic eddy in close proximity to M10. However, due to the complex nature of mesoscale activity within the southeast Cape Basin (fully described in chapter 1) the eddy was not a single coherent structure. The structure was deformed, split and merged with other anticyclonic features as it travelled across the basin. The complex nature of the feature was also indicated by the complex trajectory (Figure 4.10B). The anticyclonic feature formed within the retroflection region and was identified as A13. The feature A13 moved northwards and then split forming a new anticyclonic structure which is labelled as A16. A16 continued to move northwards where it merged with an existing anticyclonic feature (A20), and formed a new structure denoted as A16/A20 (Figure 4.10B). The features A13, A16 and A16/A20 all impacted M10 and were considered as a single feature. For brevity only the feature A16/A20 is shown by the SLA snapshot (Figure 4.10A). The anticyclonic eddy A13 was first detected on the 26/01/2015 and the subsequent features were observed to first impact the mooring array on the 03/03/2015. The 36 day period between the first detection and the impact on the mooring showed the anticyclonic feature was well established and represented a mature eddy. The trajectories showed a general north westward drift (Figure 4.10B). The complex structure and trajectory associated with the anticyclonic feature was reflected in the *in situ* data, as high variability was observed in the direction of flow at M10 (Figure 4.10C). Most of the changes in direction of flow were a result of A13 moving from east of M10 to west of M10. There was a large amount of north westward flow which was associated with high speeds (Figure 4.10C). This north westward flow was consistent with the anticyclonic rotation of A16/A20 as it was positioned south west of M10 for the majority of the observed period (Figure 4.10A). The mean speed recorded at M10 during the influence of the anticyclonic feature was 43.90cm.s$^{-1}$ with a maximum speed of 101.93cm.s$^{-1}$. The same alternating signal, periods of higher and lower speed, observed in Figure 4.8D and Figure 4.9D was also observed at M10 (Figure 4.10D). Within this oscillating signal two barotropic high speed events were observed. The remaining periods of increased speed showed a baroclinic signal which impacted to 400m depth.

## 4.3 Investigating the features driving circulation along the shelf edge

The dissimilarity in speed (Figure 4.1, Table 1), direction of flow (Figure 4.3) and the comparison with the altimetry (Figure 4.4, Table 2) between M7 and the remaining moorings suggested M7 is impacted by additional flow the dynamics not observed by the altimetry. The variation in speed and direction through depth was analysed in order to identify the features influencing the circulation M7.

### 4.3.1 Flow characteristics through depth

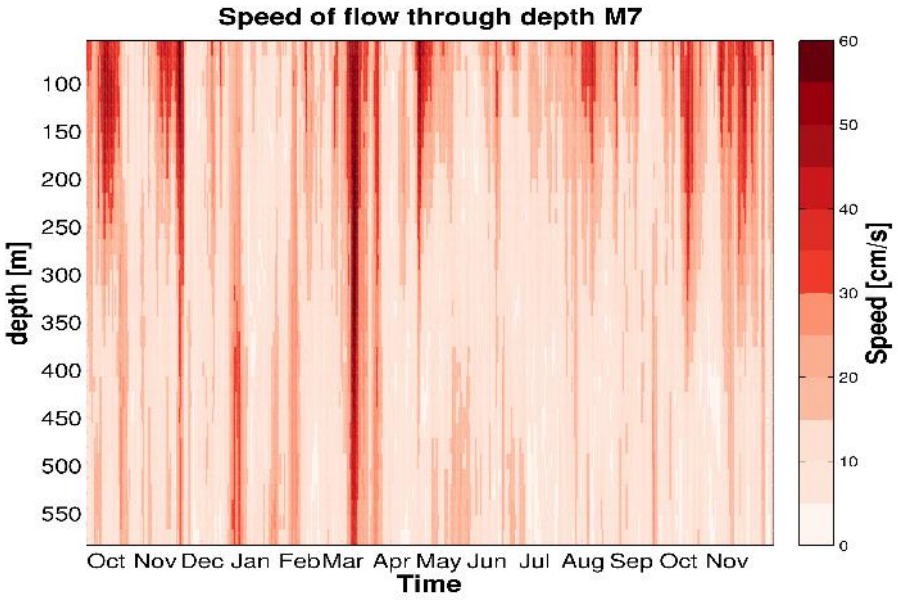


**Figure 4.11: Speed of flow [cm/s] in the upper 550m observed at M7 from 18/09/2014 to 1/12/2015.**

Figure 4.11 highlights both the timing of the high speed events and the depth to which each event impacted. The majority of high speed events at M7 did not penetrate through the upper 550m of the water column. The depth to which each event penetrated varied but tended not to impact deeper than 350m (Figure 4.11). The clear exception is the high speed event observed from1$^{st}$ to 13$^{th}$ of March which impacted the water column to at least 550m depth.

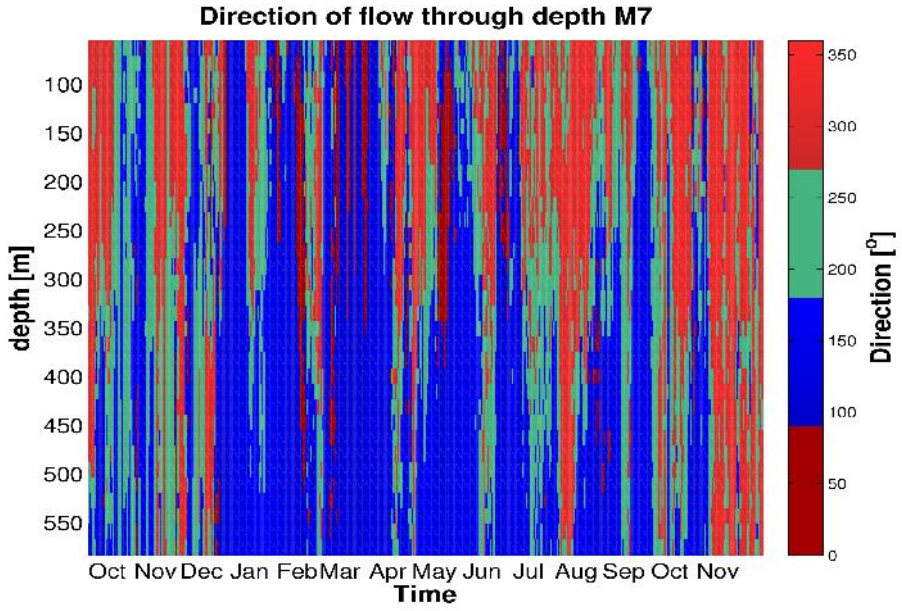


**Figure 4.12: Direction of flow [°] in the upper observed 550m at M7 from 18/09/2014 to 1/12/2015.**

The direction through depth of M7 allowed a better understanding of the characteristics of the high speed events observed at M7. The high speed events were almost exclusively associated with north westward flow (flow with a direction between 270° and 360°) (Figure 4.12). The exception again was the high speed event observed from 1$^{st}$ to 13$^{th}$ of May, which was characterised by a mixture of north eastward and south eastward flow. The high speed events associated with north westward flow direction tended not to impact deeper than 350m depth (Figure 4.11, 4.12). The high speed event from 1$^{st}$ to 13$^{th}$ of May penetrated to a depth of at least 550m. It is important to note the large amount of south eastward flow, which was observed at depths from 350 to 550m. The south eastward flow was characterised by low speeds (Figure 4.11) and was observed throughout the full time period of ADCP data (18/09/2014 to 01/12/2015) (Figure 4.12).

### 4.3.2 Features driving the circulation along the shelf edge

The low correlation between SLA data and ADCP observations (Table 2) suggested M7 was influenced by alternative flow dynamics not observed by the SLA data. Four high speed events were used as case studies in order to identify the features that are responsible for the high speed events and in turn strongly impact the circulation at the shelf edge.

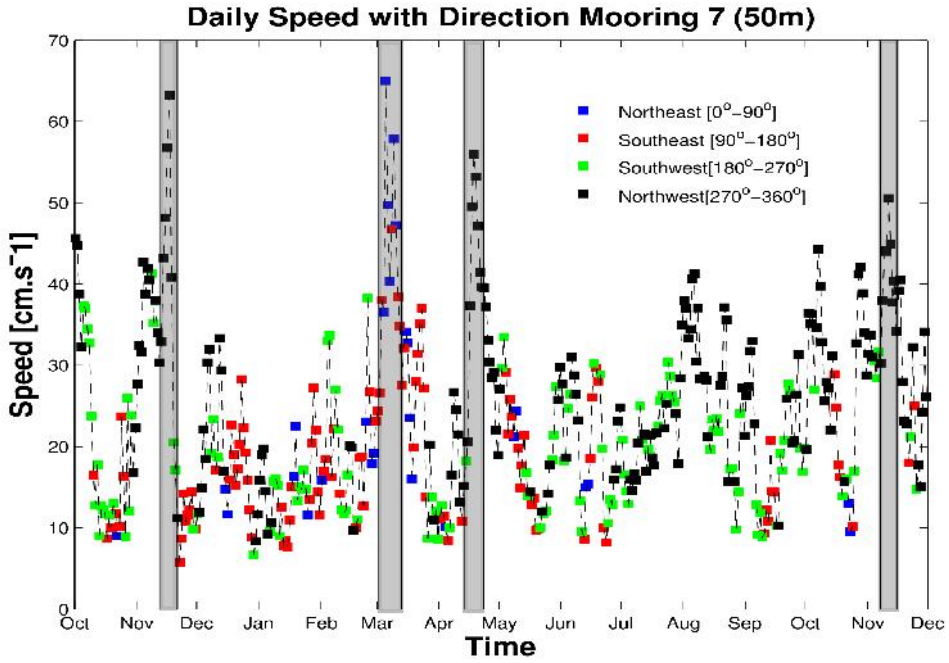


**Figure 4.13: The time series represented by the dashed line shows the daily averaged speed at ±50m observed at M7. The coloured squares indicate the direction (averaged daily) associated of the speed of flow. The highlighted bars represent four case studies.**

The high speed events at 50m depth were predominantly north westward with the exception of the event observed from 1st to the 13th of May which indicated a combination of north eastward and south eastward flow (Figure 4.13). These observations were in agreement with Figure 4.12. The four case studies were compared to SLA and SST gradient in order to identify the impact of mesoscale features and the upwelling front respectively. The cold upwelled waters along the coast formed a strong temperature gradient with the warmer waters associated with the inflow of Agulhas Current waters (section 2.5.1). The temperature gradient produced a density gradient which drives an equatorward flow. Therefore, the region of strongest SST gradient, which usually coincides with the position of the upwelling front, provided a robust indicator of the position of the equatorward transport driven by the zonal temperature gradient.

### 4.3.2.1 Case study 1 (12/11/2014 – 21/11/2014)

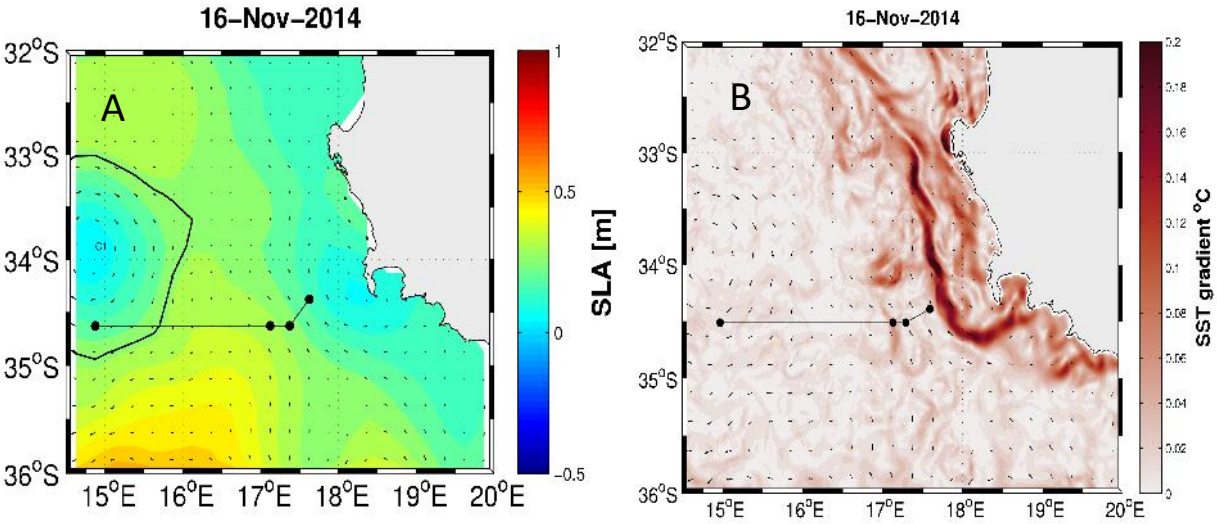


**Figure 4.14: Panel A shows the SLA for 16/11/2014 overlaid with the derived geostrophic velocities vectors. The black contour represents the eddy shape detected by the eddy tracking algorithm. Panel B shows the SST gradient for 16/11/2014 overlaid with derived geostrophic velocities. M7, M8, M9 and M10 are represented by the black.**

The SLA snapshot, 12/11/2014, overlaid with the eddy tracking algorithm showed a cyclonic eddy (C1) located over the position of M10, but no eddy or significant mesoscale feature in the vicinity of M7 (Figure 4.14A). Additionally, the SLA did not show a substantial gradient at the position of M7.

The SST snapshot for 12/11/2014 (Figure 4.14B) showed a high SST gradient offshore from the Cape Peninsula. The SST gradient showed a sharp temperature gradient over the position of M7 (Figure 4.14B). The direction of flow during the high speed event is north westward, which was consistent with flow resulting from the horizontal density gradient (Figure 4.13). The strong SST gradient (Figure 4.14B), direction of flow (Figure 4.14A) and lack of mesoscale features at the position of M7 during the case study (Figure 4.14A) provided strong evidence that the high speed event from 12/11/2014 – 21/11/2014 was driven by the horizontal density gradient.

### 4.3.2.2 Case study 2 (01/03/2015 – 13/03/2015)

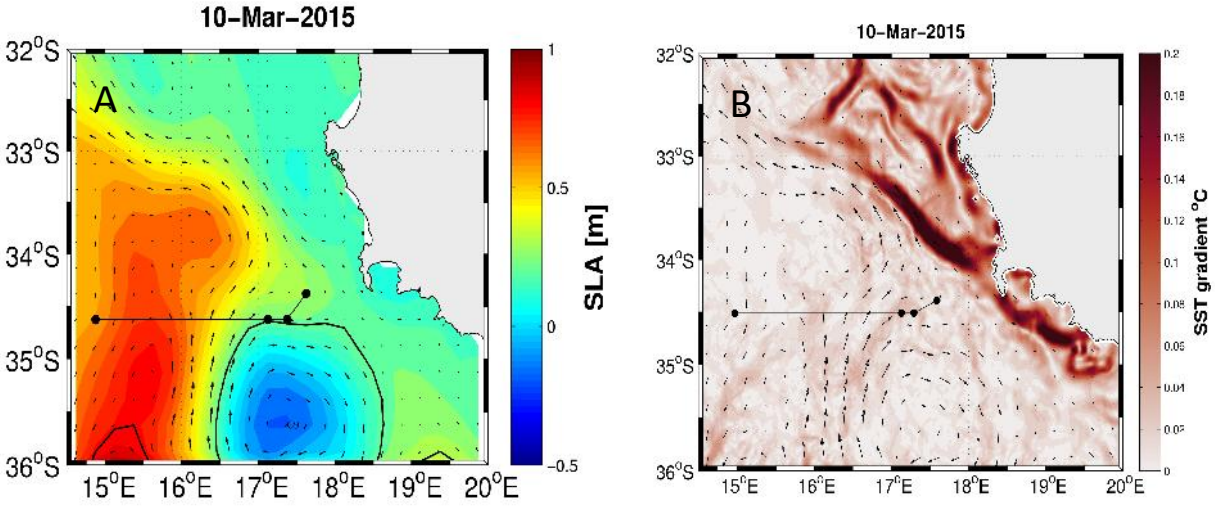


**Figure 4.15: Panel A shows SLA for 10/03/2015 overlaid with derived geostrophic velocities. The black contour represents the eddy shape detected by the eddy tracking algorithm. Panel B shows the SST gradient for 10/03/2015 overlaid with derived geostrophic.**

A strong cyclonic eddy (C9) was observed slightly south of M7 in the SLA snapshot on the 10/03/2015 (Figure 4.15A). The proximity to M7 and the definition of C9, observed by the strongly negative sea surface anomaly (±-0.5m), indicated the eddy (C9) would have strongly influenced the flow recorded at M7. The direction of flow during the high speed event, a mixture of north eastward and south eastward flow (Figure 4.13), was consistent with the cyclonic rotation of the eddy and position relative to the mooring array. The direction of flow was anomalous to the remaining high speed events which were characterised by north westward flow. In addition, the high speed event was the only event observed at M7 which penetrated the water column to at least 550m depth (Figure 4.12). The penetration of the high speed event through the upper water column has been shown to be characteristic of mesoscale features within the southeast Cape Basin (Figure 4.6).

The SST gradient was negligible at the position of M7 from the 01/03/2015 to 13/03/2015 (Figure 4.15B). The SST gradient showed an area of high SST gradient north of the mooring array, most likely representing the upwelling front (Figure 4.15B). However, the lack of SST gradient at the latitude of the mooring array showed the high speed event was not driven by the density gradient (Figure 4.15B).

The strength and proximity of the cyclonic eddy (C9) coupled with the anomalous direction and depth impacted proved the high speed event from 01/03/2015 to 13/03/2015 was driven by the mesoscale variability in the form of a cyclonic eddy (C9).

### 4.3.2.3 Case study 3 (13/04/2015 – 23/04/2015)

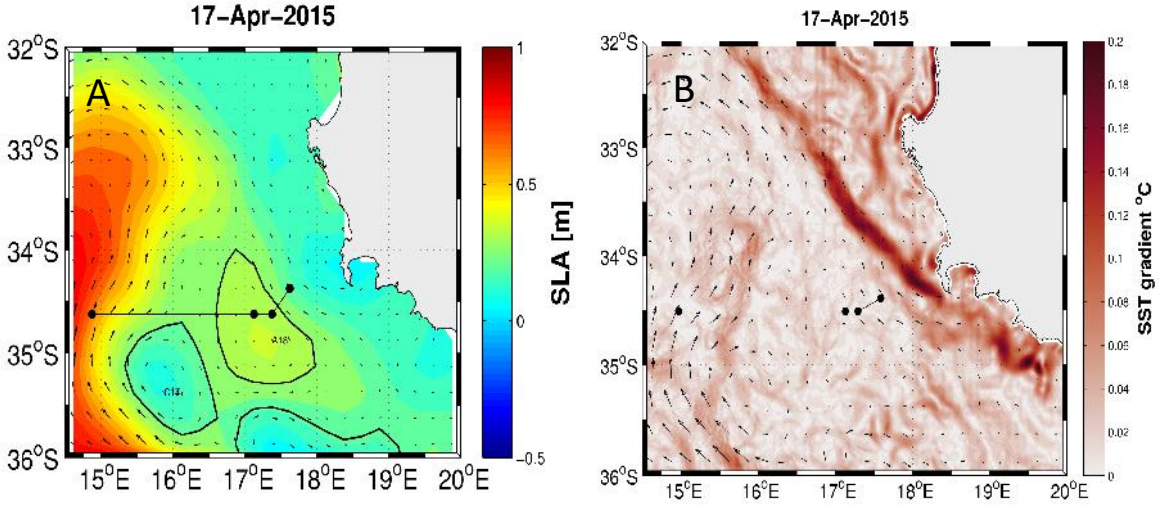


**Figure 4.16: Panel A shows the SLA for 18/04/2015 overlaid with derived geostrophic velocities. The black contour represents the eddy shape detected by the eddy tracking algorithm. Panel B displays the SST gradient for 18/04/2015 overlaid with derived geostrophic velocity vectors.**

A weak SST gradient was observed during the third case study, the high speed event from 13/04/2015 – 23/04/2015 (Figure 4.16B). The direction of flow was north westward, which is a characteristic of the flow driven by the zonal temperature gradient. However, the SST weak gradient did not provide definitive evidence that the high speed event was driven by the zonal density gradient at the shelf edge.

The SLA snapshot (Figure 4.16A) observed a weak anticyclonic eddy (A18) west of M7. The anticyclonic rotation and position relative to M7 was consistent with the north westward direction of flow observed during the high speed event. The feature (A18) showed a weak SLA gradient which implied low rotational speeds. Similar to the weak SST gradient, the weak SLA gradient did not provide definitive evidence that the anticyclonic eddy was responsible for the high speed event.

The weak gradient in SST and SLA made it difficult to distinguish a dominant feature driving the high speed event. It is likely that the high speed event was the result of a combination of both the density gradient and the anticyclonic eddy.

### 4.3.2.4 Case study 4 (07/11/2015 – 15/11/2015)

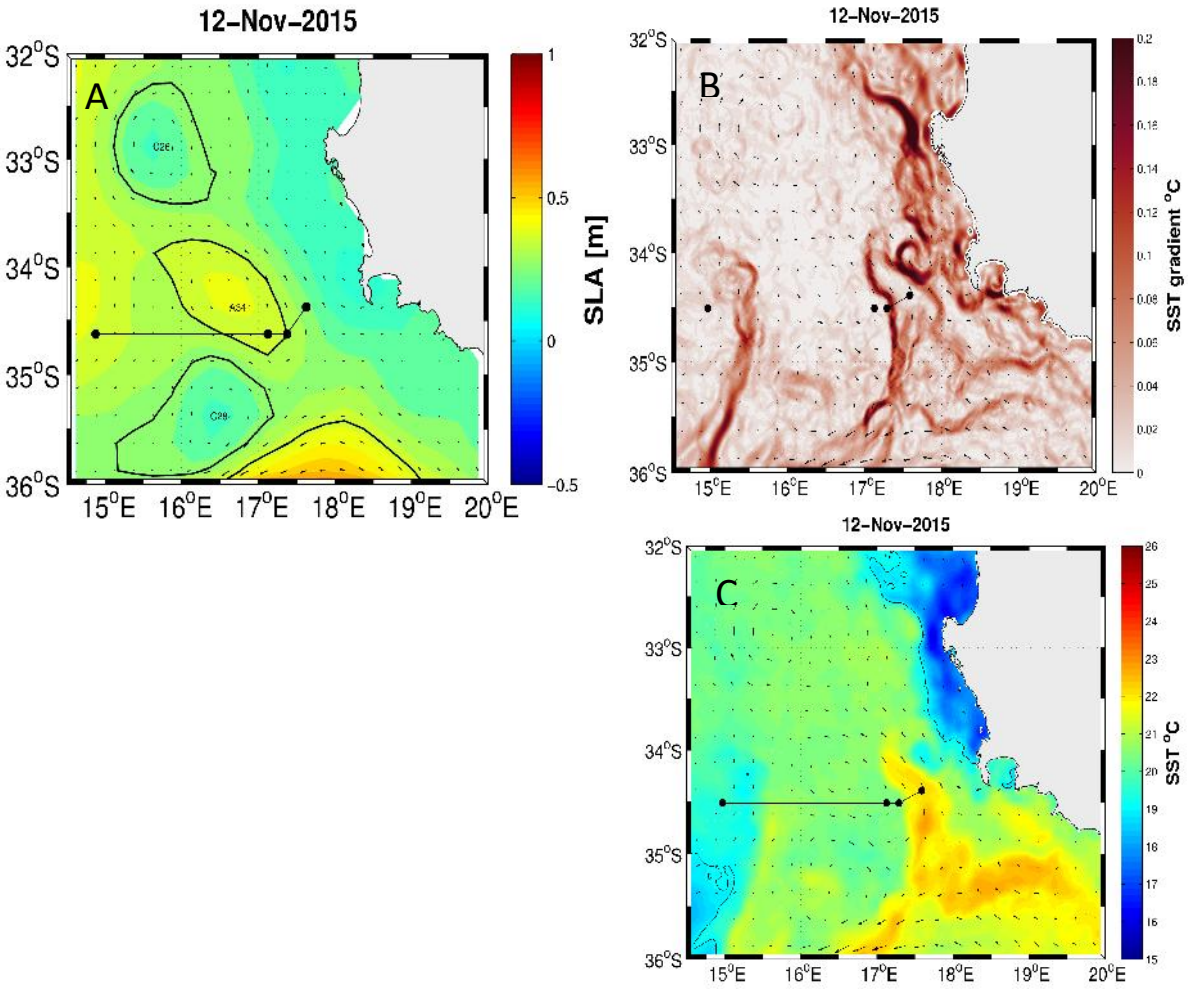


**Figure 4.17: Panel A shows the SLA for 11/15/2015 overlaid with derived geostrophic velocities. The black contour represents the eddy shape detected by the eddy tracking algorithm. Panel B shows the SST gradient for 11/15/2015 overlaid with derived geostrophic velocities from the SLA. Panel C shows the SST for 11/15/2015 overlaid with the derived geostrophic velocities, Panel B highlights the warm filament.**

The final case study, the high speed event from 07/11/2015 – 15/11/2015, showed a strong SST gradient inshore and offshore of M7 (Figure 4.17B). The strong SST gradient was unlikely to be a result of the temperature differences between the upwelling system and Agulhas influx as the high SST gradient was visible both sides, inshore and offshore, of M7. The SST observations, as opposed to the SST gradient, showed a well-defined warm filament over the position of M7 (Figure 4.17C). The filament was first identified south of the mooring array within the reflection region and was advected north westwards across the position of M7. The north westward advection was in agreement with the observed direction of the high speed event (Figure 4.12). The SLA observations showed an anticyclonic eddy (A34) west of M7 (Figure 4.17B). The anticyclonic rotation and position of A34 was consistent

with the north westward flow of the warm filament. It is important to note the advection of the warm filament closely followed the structure of A34. The similarities in structure of the filament and eddy (A34) strongly suggest the warm filament was advected by the anticyclonic eddy A34. Therefore, the high speed event from 07/11/2015 – 15/11/2015 was the result of a warm filament which was advected from the retroflection region by an anticyclonic eddy (A34).

The snapshots of SLA and SST during the four case studies presented, show that the flow at M7 was not controlled by a single dominant flow dynamic. Instead the speed and direction of flow at M7 was strongly influenced by a combination of features including; warm filaments advected from the Agulhas Bank, the density gradient produced by the juxtaposition of the upwelling system and Agulhas influx as well as cyclonic and anticyclonic eddies.

## 4.4 Interaction between mesoscale variability and upwelling system

The speed and direction of flow observed at M7 clearly showed the influence of both the offshore flow dynamics associated with mesoscale features (Figure 4.15A) and the shelf flow dynamics associated with the coastal upwelling (Figure 4.14B). The presence of both features along the shelf edge suggested there is substantial interaction between the offshore flow mesoscale feature and the upwelling front at the position of the SAMBA mooring array.

### 4.4.1 Mesoscale induced cross-shelf transport

Mesoscale features have been observed to interact with the upwelling system inducing large filaments of upwelled water which extend offshore and convolute the upwelling front (Duncombe Rae et al. 1992, Shannon and Nelson 1996, Hutchings et al. 1998). This section highlights a case study of a mesoscale feature which induced a cross-shelf transport event (Figure 4.18). The section presents *in situ* observations and detailed analysis (Figure 4.19, 4.21) of the cross-shelf transport. The analysis provided a unique insight into the interactions between the offshore and shelf dynamics.

Figure 4.18A showed a cyclonic (C1) and anticyclonic (A2) eddy pair over the mooring array on the 30/10/2014. The cyclonic eddy (C1) was positioned slightly north of the anticyclonic eddy (A2). The position and rotation associated with each feature, cyclonic rotation for C1 and anticyclonic rotation for A2, was expected to induce offshore (westward) transport. Initially, there was no significant Chl-a associated with the mesoscale features (Figure 4.18A). As time progressed a large filament of high Chl-a water was advected westward (offshore) from the shelf edge across the mooring array (Figure 4.18B, 4.18C). The filament was visible over the mooring array from the 01/10/2014 to the 16/11/2014. The filament detached from the shelf edge on the 16/11/2014 and the high Chl-a was advected further offshore and dissipated within the open ocean (Figure 4.18D). The filament closely

followed the structure of C1 and A2 (see Figure 4.18A-D) providing strong evidence that the filament was advected by the westward flow induced by the dipole interactions of C1 and A2. C1 was visible above M10 for the entire period while A2 was not identified by the eddy detection scheme after 09/11/2014 (Figure 4.18D).

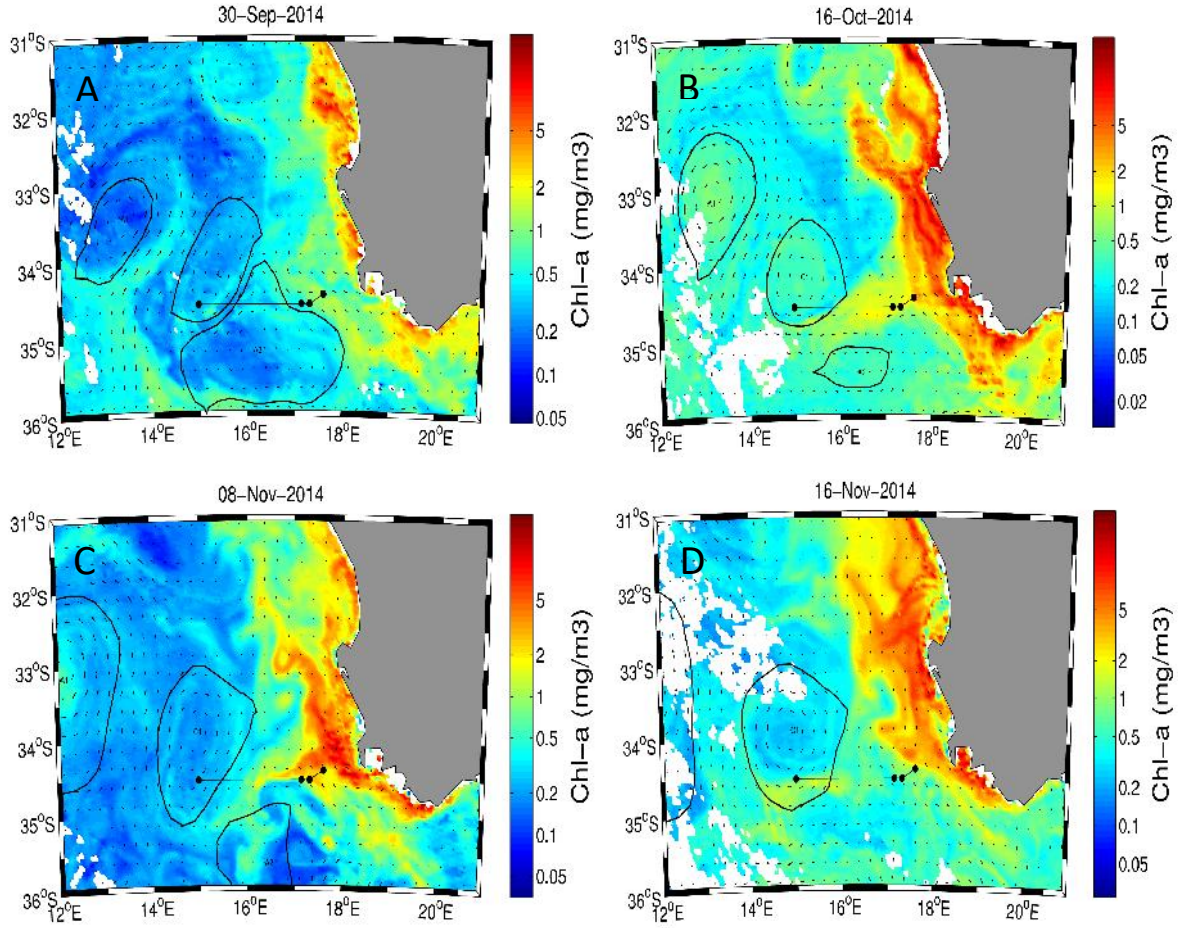


**Figure 4.18: Chlorophyll-a (mg.m$^{-3}$) derived from ocean colour averaged. The daily Chl-a data is averaged every four days to avoid excessive cloud cover. Panel A, B, C and D represent the 28/10/2014, 16/10/2014, 08/11/2014 and 16/11/2014 respectively. The black contour indicates the eddy shape and position derived from SLA.**

The advection of high Chl-a filament induced by C1 and A2 (Figure 4.18) clearly illustrated the interaction offshore mesoscale features with the upwelling front. The high Chl-a concentration of the filament indicated that productive shelf waters were advected across the shelf edge to the open ocean.

The current roses of M7, M8, M9 and M10 showed a predominantly westward (offshore) flow from 28/09/2014 to the 16/11/2014 (Figure 4.19); which is the period the high Chl-a filament was observed over the mooring array (Figure 4.18).

The direction of flow at M7 showed a general westward direction, however, south westward flow was observed most frequently (Figure 4.19A). The speed of the flow at M7 was lower (20 -30cm.s$^{-1}$) when compared to the remaining moorings during this period. The direction of flow observed at M8 was mostly in a south westward to westward direction with high speeds (>30cm.s$^{-1}$) associated with both directions of flow (Figure 4.19B). M9 indicated predominantly due west flows for the period the filament was observed over the mooring array; these west flows were associated with speeds greater than 30 cm.s$^{-1}$ (Figure 4.19C). Similar to M9, M10 recorded predominantly westward flows, which included a number of west north westward flows. M10 recorded high current speed (>30 cm.s$^{-1}$) in the westward and west north westward direction (Figure 4.19D).

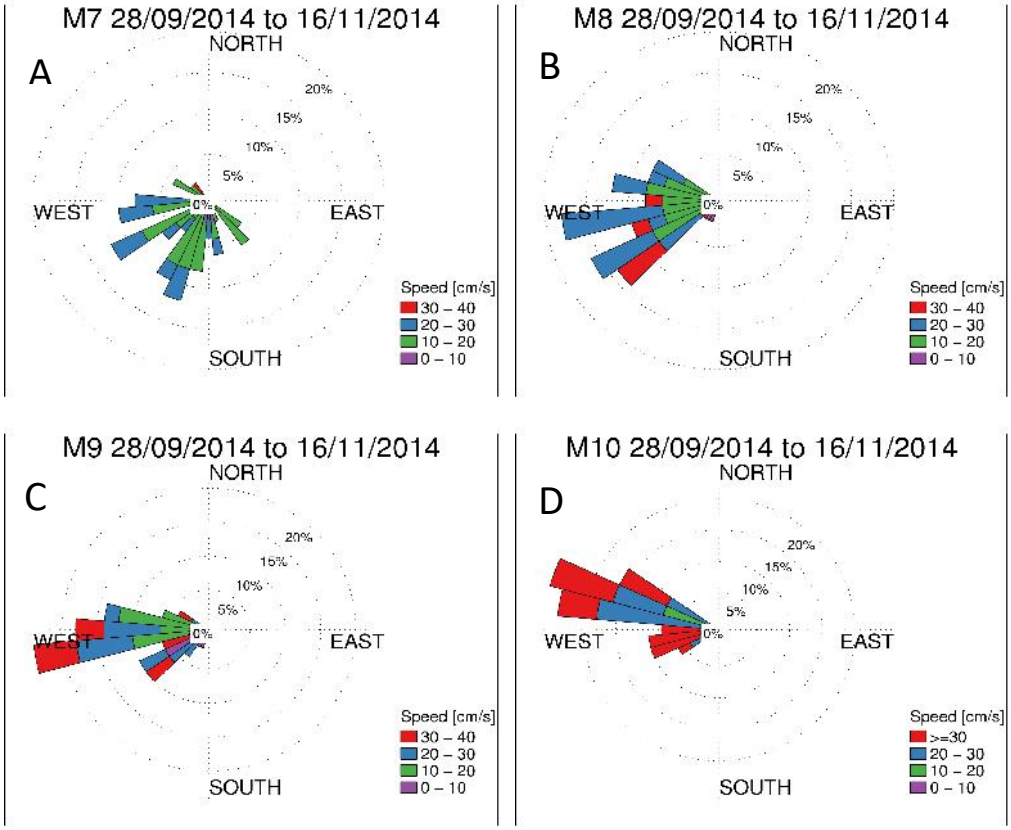


**Figure 4.19: Panel A, B, C and D show the current roses for M7, M8, M9 and M10. The direction of flow is averaged through the upper water column from 28/09/2014 to 16/11/2014. The current roses are depicted using the oceanographic convention with coloured bars pointing in the direction of flow.**

The general westward direction of flow observed by M7, M8, M9 and M10 while the high Chl-a filament was positioned over the mooring array confirmed the dipole interactions of C1 and A2 (Figure 4.18) induced a westward (offshore) flow through the upper 400m of the water column. The westward

direction of flow recorded across the mooring array showed the filament and its characteristics were captured by the ADCP data.

The position of the high Chl-a filament over the mooring array (Figure 4.18) and the confirmation that each mooring was able to capture the impact of the filament (Figure 4.19) provided a unique opportunity to assess the cross shelf transport using *in situ* observations through the upper 400m of the water column.

The SST observations were used to define the high Chl-a filament using its temperature signal (Figure 4.20). The SST defined the shape of the filament more clearly than the Chl-a observations due to similar background Chl-a values within the region (Figure 4.19). Defining the filament by SST allowed for further investigation of the spatial characteristics and origin of the filament.

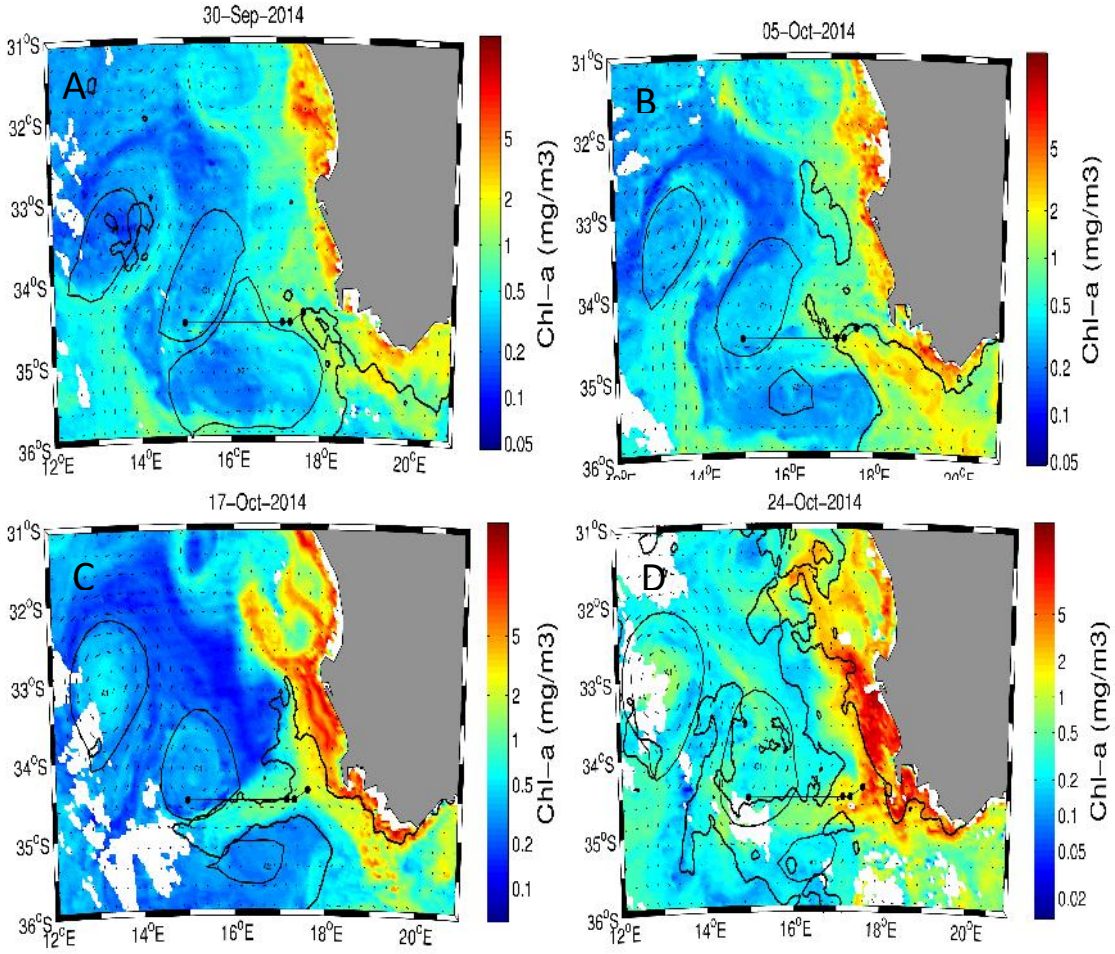


**Figure 4.20: Panel A, B, C and D shows the Chlorophyll-a (mg.m$^{-3}$) for the 30/09/2014, 05/10/2014,17/10/2014 and 24/10/2014 respectively. The Chl-a is derived from ocean colour and averaged every four days. The Chl-a is overlaid with the 19.6°C isotherm from SST. The black contour indicates the 19.6°C isotherm. The eddy shape and position derived from SLA are represent with the thin black line.**

The shape and advection of the high Chl-a filament was best represented by the 19.6°C isotherm. The 19.6°C isotherm clearly defined the high Chl-a filament, mirroring the filament during its formation and offshore advection (Figure 4.20). It was important to note that the 19.6°C isotherm did not define the high Chl-a filament after the 24/10/2014 due to background waters of similar temperature (Figure 4.20D), while the high Chl-a filament was visible over the mooring array until the 16/11/2014 (Figure 4.20D).

The relatively high temperature of the filament, greater than 19.6°C, showed that the filament was not advected from the upwelling region adjacent to mooring array, which is generally associated with temperatures below 19°C. Instead the filament was formed, and advected high Chl-a waters from the Agulhas Bank across the mooring array. The source was confirmed visually as the filament can be seen to form over the Agulhas Bank and was connected to the Agulhas Bank throughout the advection of the filament (Figure 4.20).

### 4.4.2 Quantifying the cross shelf transport event

Defining the high Chl-a filament by the SST (Figure 4.20) provided a clear illustration of the shape and spatial variably of the filament. The definition of the filament allowed for the dimensions, such as the extension offshore and width, of the filament to be calculated. The calculations of the dimensions of the filament along with the high resolution *in situ* observations, through the upper portion of the water column (Figure 4.19), enabled the amount of water transported from the shelf to the open ocean to be quantified.

#### 4.4.2.1 Depth impacted by the filament

The filament was continuously positioned over M8 and M9 from 05/10/2014-20/10/2014 (Figure 4.20). M8 and M9 were used to determine the speed and depth impacted by the filament due to the sustained observations of the filament. M7 and M10 observed the filament but were initially positioned outside the filament defined by the 19.6°C and therefore excluded.

The speed through depth at M8 and M9 showed the depth to which the filament impacted the water column. There was a clear increase in speed (Figure 4.21) from 05/10/2014 at both M8 and M9. The increase in speed corresponded to the date the filament, defined by the 19.6°C isotherm, was first observed at the position of M8 and M9 (Figure 4.20). The observed increase in speed was observed until 20/10/2014 (Figure 4.21), which again corresponded closely to the dissipation of the filament within the SST (22/10/2014) (Figure 4.20D).

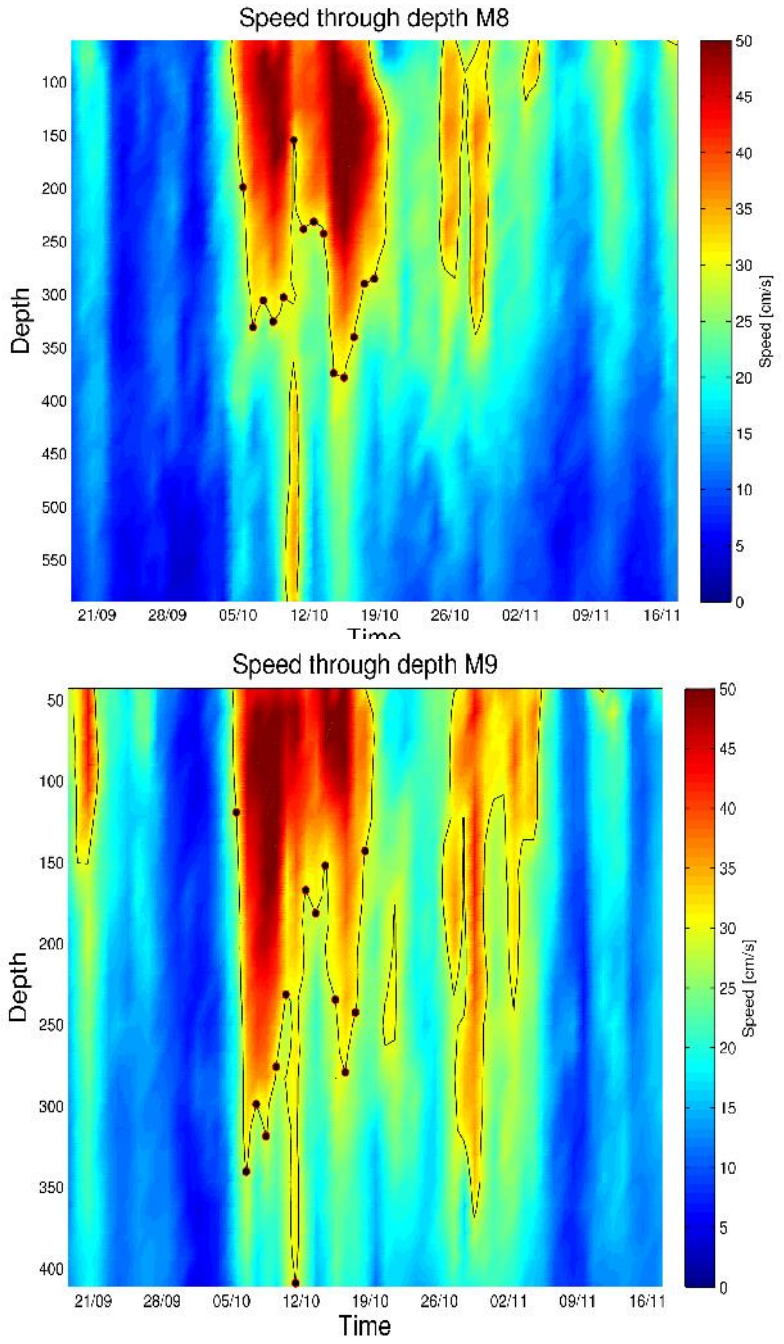


**Figure 4.21: The speed through depth at M8 and M9 [cm/s]. The speed is averaged daily. The black contour highlights the 30 cm/s contour. The red circles indicate the depth to which the filament impacts at each daily time step.**

The 30 cm/s contour captured the majority of the high speed westward flow associated with the filament (Figure 4.21). Therefore, this contour was used to define the depth of the filament. The red circles along the contour (Figure 4.21) indicated the depth to which the filament penetrated for each daily time step. The depth was used to calculate the volume transport and total volume of the

filament. The current speed observed at M8 and M9 which was used for the calculation of volume transport was averaged through depth for each daily time step.

#### 4.4.2.2 The volume of the filament

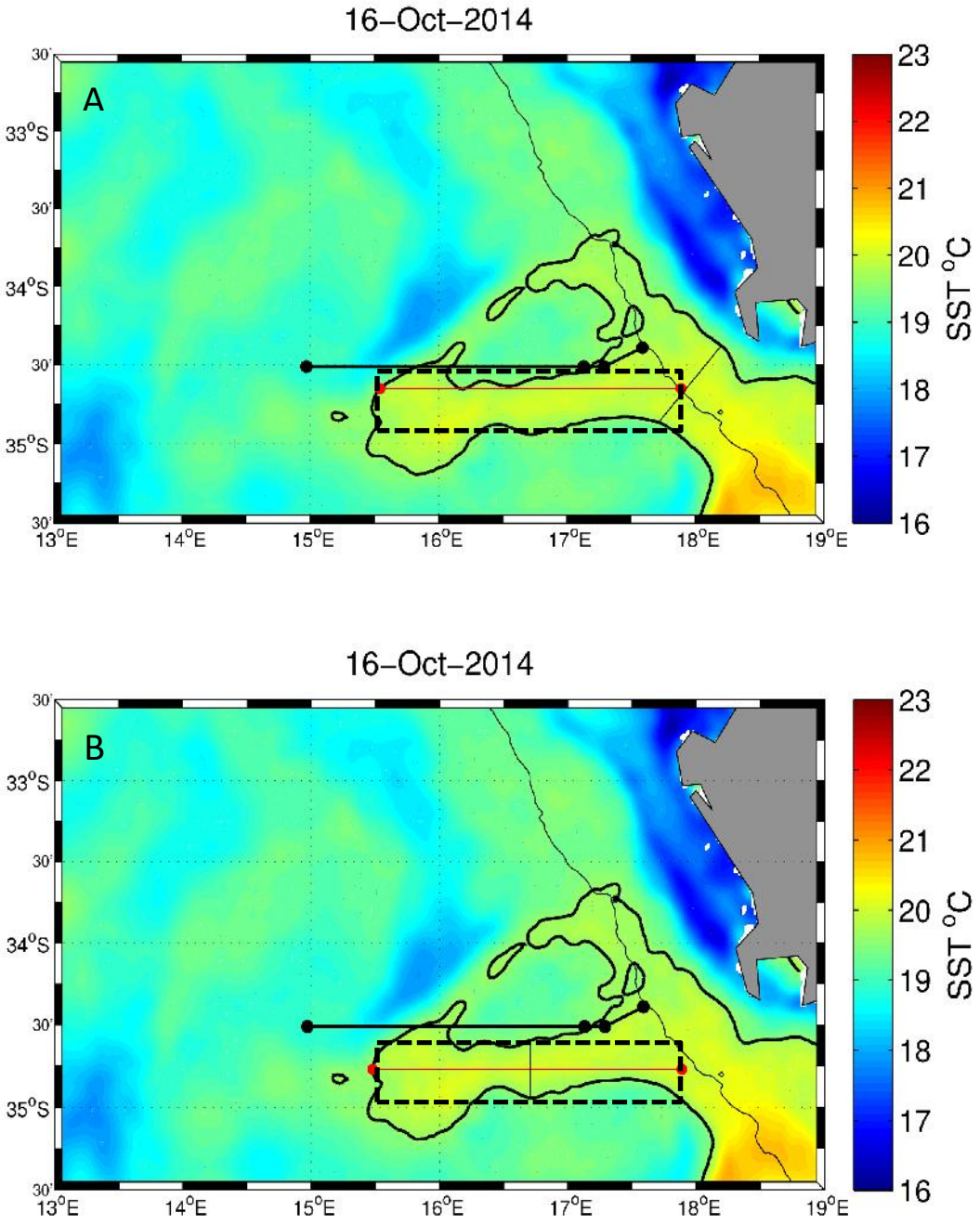


**Figure 4.22: SST for the 16/10/2014. The 19.6°C isotherm is represented by the thick black contour. The thin black contour represents the shelf edge. Panel A shows the area used to calculate the total volume using the width W1 and the length L1. The thin black line represents W1. The red line shows L1 measured from the shelf edge to the westward extend of the filament. Panel B shows the area used to calculate the total volume using W2 and L2. W2 is shown by the thin black line. L2 is represented by the red line. The area is represented by a dashed box for both cases.**

The 19.6°C isotherm was used to determine the dimensions used to calculate the total volume of water within the filament. Two positions were chosen to represent the width of the filament, W1∼17.6°E, 18.11°E (Figure 4.22A) and W2∼16.8°E (Figure 4.22B). The widths were chosen visually in order to provide the best representation of the width of the filament due to the high spatial variability of the filament. The widths were recorded daily across the two sections from 05/10/2014 - 18/10/2014.

Similarly, two lengths were visually chosen in order to provide a robust representation of the spatial variability of the filament. The westward extent of filament at two latitudes L1 - 34.65°S (Figure 4.23A) and L2- 34.77°S were used for the length of the filament (Figure 4.23B). The length was measured from the shelf edge represented by the thin black contour (Figure 4.23). The length was recorded daily throughout the observed period (05/10/2014 - 18/10/2014). The total volume of the filament was calculated under the assumption the filament forms a general rectangular shape, using a combination of the two lengths and two widths described by Figure 4.23 and the depths indicated by Figure 4.21 (Table 4).

| | **Mean Volume ($m^3$) (05/10/2014-18/10/2014)** | **Maximum Volume ($m^3$)** | **Minimum Volume ($m^3$)** |
|---|---|---|---|
| **(L1 W1)** | $2.64 \times 10^{12}$ | $4.65 \times 10^{12}$ | $6.93 \times 10^{11}$ |
| **(L1 W2)** | $2.07 \times 10^{12}$ | $3.68 \times 10^{12}$ | $9.23 \times 10^{11}$ |
| **(L2 W1)** | $2.78 \times 10^{12}$ | $4.77 \times 10^{12}$ | $3.68 \times 10^{11}$ |
| **(L2 W2)** | $2.28 \times 10^{12}$ | $5.37 \times 10^{12}$ | $9{,}06 \times 10^{11}$ |

**Table 3: The total volume calculated for the filament from the 05/10/2014 to the 18/10/2014**

The total volume showed consistency using a combination of W1, W2, L1 and L2 (Table 3). The total volume calculated using a combination of each length and width was in the order of $2\times 10^{12}$ $m^3$. The constancy in the total volume calculated showed the spatial variability of the filament defined by the 19.6°C isotherm was well accounted for using a combination the above mentioned dimensions. The volume calculated indicated that a substantial amount of water was transported from the Agulhas Bank to the open ocean.

### 4.4.2.3 The volume transport

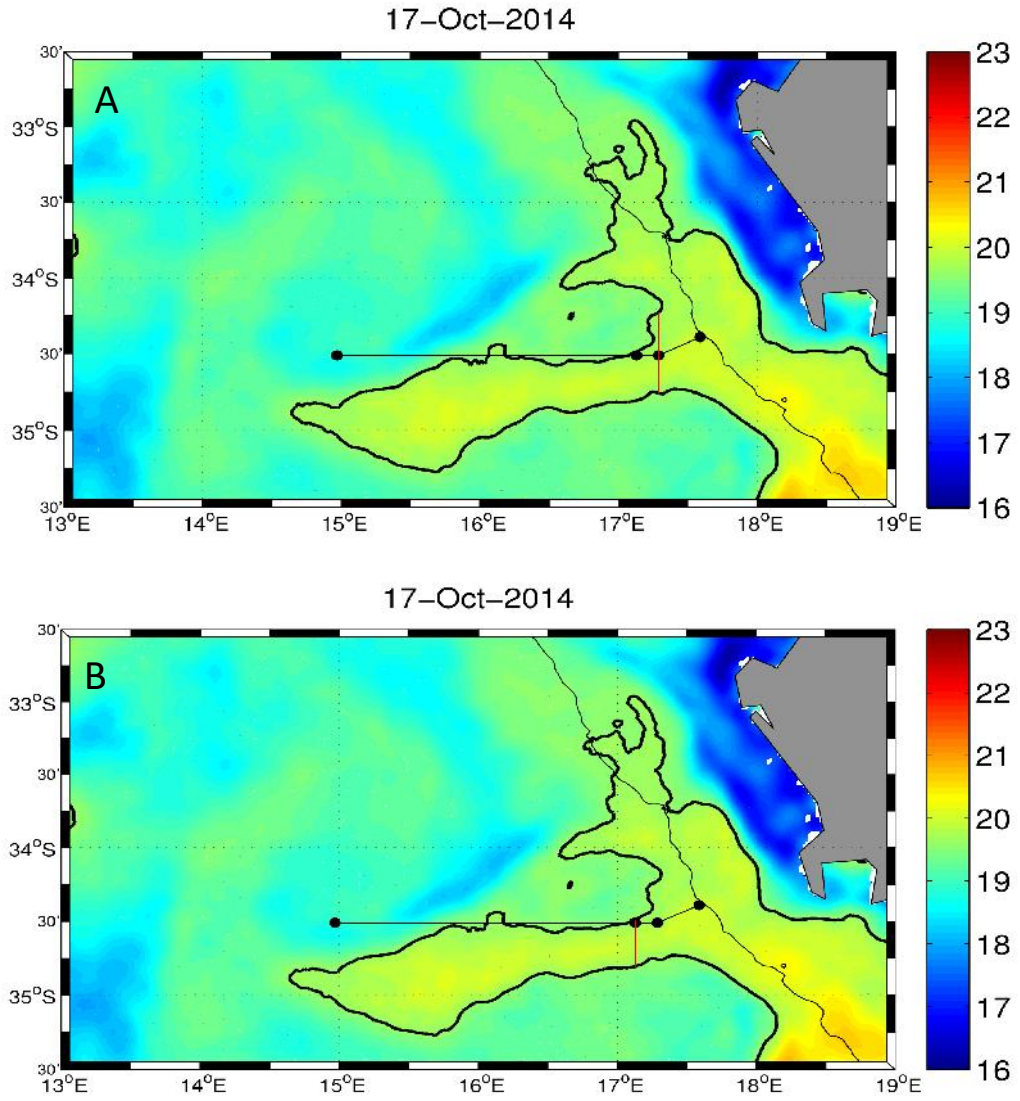


**Figure 4.23: SST for the 17/10/2014. The 19.6°C isotherm is represented by the thick black contour. The thin black contour represents the shelf edge. Panel A shows the width of the section across M8 used to calculate the volume transport. The red line shows the section. Panel B shows the width of the section across M9 used to calculate the volume transport, indicated by the red line.**

The volume transport was calculated across two sections at the position of M8 and M9 respectively. The distance across the filament at the position of M8 (Figure 4.23A) and M9 (Figure 4.23B) was measured for each daily time step from the 08/10/2014 to 17/10/2014. Due to the high spatial variability of the filament the period from the 08/10/2014 to 17/10/2014 represented a consecutive period where a width across the filament, at the position at M8 and M9, was able to be recorded. The distance of the section at the position of M8 and the corresponding depth impacted by the filament M8 was identified for each daily time step. The U-velocity component of the velocity was calculated

and averaged through the upper column. The U-component represented the westward flow during the period and was perpendicular to the sections used to calculate the volume transport at M8. The width, depth impacted, and U-component was used to calculate the daily volume transport. The same procedure was followed for M9. The widths, corresponding depths impacted and speeds were used to calculate the volume transport for each time daily step across the two sections at M8 and M9. The daily volume transport was averaged from the 08/10/2014 to 17/10/2014 for the sections across M8 and M9 (Table 4).

| | **Mean volume transport (08/10/2014-17/10/2014)** |
|---|---|
| **M8** | $-1.56 \times 10^{6}$ $\frac{m^3 \cdot s^{-1}}{m^3 \cdot s^{-1}}$ |
| **M9** | $-7.98 \times 10^{5}$ $\frac{m^3 \cdot s^{-1}}{m^3 \cdot s^{-1}}$ |

**Table 4: The volume transport calculated across the section at the position of M8 and M9 from the 08/10/2014 to the 17/10/2014.**

The volume transport calculations used a number of assumptions which were noted in chapter 5. The assumptions made when defining the dimensions of the filament decrease the precision of the volume transport calculations. Therefore, the values of volume transport were not presented as exact values. However, the *in situ* observations provided an improved estimate of cross shelf transport compared to previous estimates which were limited to satellite and model observations. The volume transport showed that the filament transported a substantial amount of water ±1Sv (1Sv = $10^{6}\ m^3.s^{-1}$) from the shelf to the open ocean from the 08/10/2014 to 17/10/2014. The negative value of final solution of the volume transport indicated the direction of flow (westward) (Table 4).

# Chapter 5: Discussion

The SAMBA mooring array provided the first set of long term, high resolution *in situ* observations within the southeast Cape Basin. The position of the mooring array provided an opportunity to assess the features associated with the offshore mesoscale variability and the coastal upwelling system which have largely been limited to satellite (Hall and Lutjeharms 2011, Dencuasse et al. 2010), model (Rubio et al. 2009, Veitch and Penven 2017) and short term hydrographic studies (Duncombe Rae et al. 1992, Boebel et al. 2003). The *in situ* data, used in conjunction with satellite observations, showed a distinct difference between the offshore circulation and the circulation at the shelf edge. The variation in the local circulation as well as the identification and analysis of the features driving the circulation are elaborated below.

## 5.1 The circulation of the southeast Cape Basin and the features driving the circulation

### 5.1.1 Differences in the circulation at the position of the SAMBA mooring array

The analysis of the ADCP data revealed a substantial difference in both the speed and direction of flow across the mooring array. Both the mean and standard deviation of the resultant speed progressively increased offshore across the mooring array (Table 1). The lowest mean and standard deviation was observed at M7, which was located closest to the shelf, while the highest values were recorded at M10, which was located furthest offshore (Table 1). The variation in speed across the mooring array was the result of an increase in both the number and intensity of short time scale, high speed events; these events were easily identified in the time series of observed speed (Figure 4.1A-D, 4.2C). The direction of flow (Figure 4.3) indicated a similar trend to the observed speed. There was a clear increase in the variability of the direction of flow across the mooring array; with relatively low variability in direction of flow observed at M7, increased variability in the direction of flow was observed at M8 and M9 and the highest variability in the direction of flow was recorded at M10.

U- and V-components of the velocity were analysed to show the relative importance of zonal and meridional flows in an attempt to further investigate the difference in flow detected across the mooring array (Figure 4.2). The U- and V-components observed at M10 were dissimilar to the remaining moorings which indicated the circulation at M10 was most likely driven by features which did not impact the remaining moorings (Figure 4.2). Conversely, the U- and V-components calculated for M8 and M9 were comparable; showing the circulation at M8 and M9 was most likely the

driven by the same features or flow dynamics (Figure 4.2). M7 showed strong similarities to M8 and M9 for the U-component, however, the V-component calculated for M7 showed no resemblance to the remaining moorings (Figure 4.2).

The similarities in the U-component and not the V-component suggested there were features, specifically features associated with meridional flows, driving the circulation at M7 which did not impact the remaining moorings.

It is important to note the position of each mooring within the mooring array when considering the differences in circulation. M10 was located furthest offshore and the distance to the closest mooring, M9, was considerably larger than the distance between the remaining moorings which were relatively close together (Figure 3.1). The irregular location of the moorings may explain the dissimilarity of the U- and V-components between M10 and the remaining moorings; as distance between M10 and the remaining moorings may have allowed offshore features to impact M10 without influencing the moorings closer to the shelf (Figure 3.1). Similarly, the proximity of M8 and M9 explained the similarities in the U and V-components as the moorings were likely to be impacted by the same features. However, the position of the moorings cannot fully explain the dissimilarity between the V-component observed at M7; as M7 was situated relatively close to M8.

### 5.1.2 Identifying the features driving local circulation within the southeast Cape Basin

Mesoscale variability has been shown to strongly influence the local circulation of the southeast Cape Basin (Boebel et al. 2003, Richardson 2007, Dencausse et al. 2010, Hall and Lutjeharms 2011). Considering the prevalent role of mesoscale features within the region the *in situ* ADCP data was compared to altimetry in an attempt to identify if mesoscale variability was responsible for the variation in speed and direction of flow across the mooring array.

The offshore mesoscale variability was examined by calculating the mean eddy kinetic energy (EKE) for the same time period the ADCP data was recorded (Figure 4.4). The southeast Cape Basin was characterised by high EKE offshore and low EKE observed over the shelf; with the expectation of relatively high EKE located along the shelf edge (Figure 4.4). The mean EKE observed (Figure 4.4) showed good agreement with previous descriptions of mesoscale variability within the region (Lutjeharms et al. 2003, Boebel et al. 2003, Hall and Lujteharms 2011). The high EKE offshore was connected to high EKE observed over Agulhas retroflection which confirmed the retroflection was a source of the high offshore EKE (Figure 4.4); the Agulhas retroflection has been well documented as a source of mesoscale features, both cyclonic and anticyclonic, within the southeast Cape Basin (Lutjeharms et al. 2003, Richardson 2007). The relatively high EKE along the shelf can be attributed to

the formation of cyclonic shelf eddies, which are known to regularly form along the shelf edge within the southeast Cape Basin (Rubio et al. 2009, Hall and Lutjeharms 2011). The agreement between the literature and the observed EKE demonstrated the EKE accurately represented the mesoscale variability of the region and could be used to assess the impact of mesoscale features on the mooring array.

The low EKE observed closest to the shelf and high EKE offshore created a substantial zonal EKE gradient at the latitude of the mooring array (Figure 4.4). The EKE gradient mirrored the pattern of increased speed and variability in direction of flow observed across the mooring array; which suggested the mesoscale features associated with the observed EKE was responsible for the variation in flow observed across the mooring array. The physical characteristics of mesoscale eddies can be used to explain the short time-scale high speed observed. The mesoscale eddies within the southeast Cape Basin are characterised by rotational speeds of 40–60 $cm.s^{-1}$ (Richardson 2007). The rotational speeds of the eddies were in agreement with the speed of the high speed current events observed across the mooring array. Furthermore, the advection or translation of the eddy structure, $3.6\pm8cm.s^{-1}$ and $3.8 \pm1.2cm.s^{-1}$ for cyclonic and anticyclonic eddies respectively would result in the short temporal nature of the events observed (Boebel et al. 2003). The variable direction of flow can also be associated with the physical characteristics of mesoscale eddies as the direction of flow would change according to the rotation of the eddy, cyclonic or anticyclonic, and the position of the feature in relation to the mooring array.

The zonal EKE gradient showed the increased number and intensity of high speed events and higher variability in the direction of flow observed at M10 was the result of additional mesoscale features which impacted M10 relative to the other moorings. The increased number of mesoscale features impacting M10 also explained the dissimilarity between the U- and V-components (Figure 4.2) observed at M10. There were distinctive features impacting M10 which did not impact the remaining moorings. M8 and M9 were located in a region of lower EKE and therefore less likely to be impacted by mesoscale features; the reduced impact of mesoscale features was reflected in the decreased number of high speed events and less variability in the direction of flow observed at M8 and M9. The similarity between the U- and V-components of M8 and M9 (Figure 4.2) confirmed they were impacted by the same mesoscale features. There was little difference in the EKE observed over the position M7 and the position of M8 and M9. However, the small difference in EKE was not reflected in the variation in flow across the mooring array as M7 showed fewer high speed events with lower speeds as well as the least variability in direction of flow compared to M8 and M9. This, however, may have been a result of the colormap scaling used to accommodate the high EKE values offshore; the scaling may

have resulted in a smoothing of the gradients between low values of EKE (Figure 4.4). It is important to note the dissimilarity in the V-component observed at M7 compared to M8 and M9 (Figure 4.2). The dissimilarity observed in the V-component and not the U-component points to features that influenced meridional flow at M7 which were not observed and M8, M9 and M9.

In order to further investigate the influence of mesoscale variability on the mooring array the correlation between the derived velocities from altimetry and the ADCP data was assessed (Table 2). Anomalies observed in the sea level within the vicinity of the mooring array can be confidently attributed to mesoscale features due to the domination of mesoscale activity within the southeast Cape Basin (Boebel et al. 2003). Therefore, the geostrophic velocities derived from SLA were assumed to result exclusively from mesoscale activity within the southeast Cape Basin. The correlation of the derived velocity and the flow at ±50m observed at each mooring indicated the relationship between the two data sets. If the two datasets were strongly correlated, the ADCP data displayed similar variations in flow to the derived velocities; which showed the flow was driven by mesoscale features. Conversely a low correlation indicated the ADCP data was not in agreement with the flow derived from SLA and therefore, not driven by mesoscale activity.

It is important to note the constraints of the correlation presented. The U- and V- velocities of the SLA product included only geostrophic flows, flows where the pressure gradient force was balanced by Coriolis force, as the velocities were derived using only the anomalies observed in the sea level. Conversely, the ADCP direct measurements included both geostrophic flows and localized ageostrophic flow events. The U- and V- velocity components of the ADCP data were recorded at ~50m depth whereas the SLA velocities were derived from the surface measurements. In addition, ADCP data provided point measurements compared to SLA which was a gridded product and therefore interpolated across a 0.25° grid cell. Both datasets were averaged daily. Despite the constraints associated with the correlations, all the correlations presented were statistically significant.

There were strong correlations for M8, M9 and M10, which again illustrated the strong influence of mesoscale activity on the offshore moorings. M10 showed the strongest correlation while M9 indicated a slightly stronger correlation than M8 in agreement with the offshore trend previously observed in the speed and variability in the direction of flow (Table 2, Figure 4.1A-D, Figure 4.3). The strong correlation provided definitive evidence that mesoscale variability was the dominant feature driving the circulation at M8, M9 and M10. M7 showed a weak correlation; the correlation was substantially lower for both the U- and V-component compared to the remaining moorings. The weak correlation indicated that mesoscale variability was not the dominant flow dynamic influencing the circulation at M7. The most intriguing result from the correlations was the large difference in

correlations between M7 and the remaining moorings. As previously mentioned, the positions of the moorings were not uniform across the array, as the moorings were located on the geographic contours (Figure 3.1). The distance between M10 and M9 was much larger than the distance between M7, M8 and M9 which were relatively close together. The distance between moorings and as well as offshore EKE gradient (Figure 4.4) suggested the biggest difference between the correlations should have been between M10 and the remaining moorings. However, a substantial difference was observed in the correlation of M7 compared to the remaining moorings. This stark contrast in correlation for M7 compared to the remaining moorings confirmed there was an alternative flow dynamic, not observed by altimetry, driving the circulation at M7 and did not influence M8, M9 and M10.

## 5.2 Investigating mesoscale variability within the southeast Cape Basin

The variation in speed (Figure 4.1, Table 1), direction (Figure 4.3) and the comparison with the altimetry (Figure 4.4, Table 2) provided strong evidence that mesoscale variability was the dominant flow dynamic driving the circulation at M8, M9 and M10. The confirmation that ADCP data observed the impact of mesoscale variability provided a unique opportunity for long term, high resolution *in situ* observations and monitoring of mesoscale variability in southeast Cape Basin. The *in situ* nature observations (section 3.1) were important as previous studies of the mesoscale variability have often been limited to satellite, model or short term hydrographic data preventing precise analysis of mesoscale features through the water column (Boebel et al. 2003, Rubio et al. 2009, Dancausse et al. 2010, Hall and Lutjeharms et al. 2011). The ADCP data was used to show the impact of mesoscale variability on the upper water column as well as provide precise analysis of individual features observed by the mooring array.

### 5.2.1 Characterising the impact of mesoscale variability on the circulation

The high speed events, shown to represent the impact of mesoscale features on the mooring array (section 5.1), were observed to penetrate through the upper water column (Figure 4.6, Figure 4.7). Both the signal of speed and direction of flow were observed to penetrate to 550m (400m) depth for M8 (M9, M10). There were two notable high speed events, both observed at M10, which were characterised by a barotropic signal with no change in speed with depth. The barotropic events were noteworthy as flow associated with mesoscale features within the region have been suggested to be baroclinic (Schimd et al. 2003). There was no discernible trend in direction of flow at M8, M9 and M10, however, each high speed event was associated with a distinctive direction of flow. The variable direction of flow was expected as the direction of flow will depend on the rotation of eddy, cyclonic or anticyclonic, and the position of the feature in relation to the mooring array as mentioned above.

### 5.2.2 Characterising individual mesoscale features

The eddy tracking algorithm (section 3.3) allowed for the identification and tracking of individual mesoscale features. A total of 38 anticyclonic and 33 cyclonic eddies were observed from 18/09/2014 to 01/12/2015 within the southeast Cape Basin (Figure 4.7A). The eddy detection scheme showed anticyclonic eddies exhibit a general north westward trajectory (Figure 4.7C); while the initial detection of the anticyclonic eddies were concentrated within the retroflection region (Figure 4.7D). The trajectory and initial detection of the anticyclonic eddies was in good agreement with previous studies (Boebel et al. 2003, Dencuasse et al. 2010). The cyclonic eddies were shown to have a general west southwestward trajectory (Figure 4.7B). The initial detection of the cyclonic eddies were concentrated along the shelf edge and along the western edge of the Agulhas Bank, inshore of the Agulhas Retroflection (Figure 4.7D); again in line with previous studies (Rubio et al. 2009, Hall and Lutjeharms 2011). The similarities between the literature and the initial detection and trajectory observed by the detection method provided confidence that the eddy tracking algorithm can successfully detect and track mesoscale features within the southeast Cape Basin. The eddy tracking scheme observed a high number of cyclonic and anticyclonic eddies first detected offshore and removed from major topographic or oceanography features. These features represented smaller eddies split from large features or short-lived shear features induced by the passing of larger mesoscale features. The initial detection of these eddies highlighted the complex and turbulent nature of mesoscale activity within the southeast Cape Basin again in good agreement with the literature (Boebel et al. 2003).

From the 38 anticyclonic and 33 cyclonic eddies detected within the southeast Cape Basin 8 anticyclonic and 6 cyclonic eddies could be associated with high speed events (defined as speed higher than two standard deviations from the mean) observed at M8, M9 and M10. From the 8 anticyclonic and 6 cyclonic eddies three case studies were selected in order to provide a precise analysis, through the upper water column, of mesoscale features within the region. Two cyclonic eddies, an early and mature cyclonic eddy, both formed along the shelf edge and one mature anticyclonic eddy, formed within the retroflection region, were used as case studies. The case studies were selected as both the cyclonic shelf eddies and anticyclonic eddies formed with the retroflection region are recurrent features, frequently observed within the southeast Cape Basin, which contribute to both interocean exchanges and coastal-open ocean exchanges (Richardson 2007, Rubio et al. 2009). Cyclonic shelf eddies have been shown to transport substantial amounts of water from the shelf to the open ocean as they translate offshore (Rubio et al. 2009). This coastal-open ocean exchange strongly impacts the

local circulation and marine ecosystem (Rubio et al. 2009). The cyclonic shelf eddies also play a vital role in interocean exchange as their interaction with the Agulhas influx enhances mixing within the southeast Cape Basin (Boebel et al. 2003, Hall and Lutjeharms 2011). The role of anticyclonic eddies shed from the Agulhas retroflection in the interocean exchange is well documented (De Ruijter et al. 1999, Beal et al. 2011). However, many anticyclonic eddies shed from the reflection dissipate rapidly within the southeast Cape Basin and do not contribute to interocean exchanges through the traditional slow leakage of Indian Ocean water (Boebel et al. 2003). Approximately only four to six large, well-defined anticyclonic eddies cross the Cape Basin, slowly leaking their Indian Ocean signal in the background waters of the South Atlantic Ocean (De Ruijter et al. 1999, Beal et al. 2011). The anticyclonic eddy selected as a case study was a well-defined feature and traversed the southeast Cape Basin representing a 'traditional' Agulhas Ring (Figure 4.10).

#### 5.2.2.1 Mature cyclonic shelf eddy

The cyclonic eddy (C1) was observed to form along the shelf edge, north of the mooring array (Figure 4.8B). C1 was first detected on the 03/06/2014 and first impacted the mooring array 117 days later showing it was well established by the time it reached M10 and could be considered a mature structure. The current rose for the observed period indicated a prominently westward flow which was consistent with the cyclonic rotation and position of the eddy relative to the mooring array (Figure 4.8C). The speed through depth provided a more detailed observation of the flow; interestingly the speed displayed an oscillating signal of high and low speed while C1 was in close proximity to M10. The oscillating signal can be explained by small changes in the position of C1 relative to M10. The structure of cyclonic eddies are well known to exhibit the highest rotation speed at the outer-edge of the structure and lowest rotation speed in the centre of the structure. Therefore, depending on the location of C1; shifts in position which brought the centre of the structure closer to M10 resulted in periods of low speed. Conversely, shifts in position which moved the outer edge of the structure closer to position of M10 resulted in periods of increased speed.

The periods of high speed observed while C1 impacted M10 extended through the water column to a depth of at least 400m. The depth impacted by the cyclonic eddy was in agreement with the characteristics of the mesoscale variability observed for the full period of ADCP data (Figure 4.6, Figure 4.7). The mean speed of flow, averaged through the upper water column, from the 20/09/2014 to 07/12/2014 was 32.33cm.s$^{-1}$ with a maximum speed of 50.14cm.s$^{-1}$. There was a distinct period from 01/12/2014 to 07/12/2014 of increased speed. This period of increased speed coincided with an anticyclonic eddy (A2) observed directly south of C1 forming a dipole eddy pair. The rotation and position relative to the mooring array of the anticyclonic eddy (A2) produced an additional westward

flow which added to the westward flow driven by C1. The addition of the two westward flows created the period relatively higher speed. The dipole induced flow highlighted the interaction of mesoscale features within the region and the associated impacts on the local circulation within the southeast Cape Basin.

#### 5.2.2.2 Immature cyclonic shelf eddy

A cyclonic eddy (C9) was observed to impact M8 and M9 from the 19/12/2014 to 20/01/2015. C9 was formed at the latitude of the mooring array, over the continental shelf, and was first detected over the position of M8 and M9 indicating that C9 was a newly formed structure (Figure 4.9B). The formation of C9 over the mooring array provided an ideal opportunity to compare the flow characteristics of a newly formed cyclonic eddy (C9) to a well-established cyclonic eddy (C1) both formed along the shelf edge. The direction of flow observed at M9 showed a predominantly south to south eastward flow, which was consistent with the cyclonic rotation of C9 and position relative to the mooring array (Figure 4.9A, 4.9C). The variation between direction of flow observed at M10 for C1 and M9 for C9 was a result of the respective eddy positions relative to the mooring array.

The speed through depth observed at M9 indicated an oscillating signal of high and low speed similar to C1, however, there were only two periods of high speed and one period of low speed (Figure 4.9D). The decreased number of high and low speed periods compared to C1 was a result of C9 impacting the mooring array for a shorter time period, 32 days compared to 78 days, which allowed for less movement of the C9 relative to the mooring array. The periods of high speed penetrated to a depth of at least 400m on both occasions again in agreement with the general trend of mesoscale variability. Visual comparisons of C1 and C9 from SLA showed C9 as a much smaller structure with a weaker sea surface anomaly gradient (Figure 4.8A, 4.9A). A weaker sea surface gradient is expected to result in a weaker rotational speed. However, the in situ observations from M9 showed a higher mean speed for C9 (39.85 cm/$s^{-1}$) compared to C1 (32.33cm.$s^{-1}$) and a higher maximum speed for C9 (53.16cm.$s^{-1}$) compared to C1 (50.14cm.$s^{-1}$). The higher mean and maximum speed of C9 compared to C1 may suggest that the rotational speed of mesoscale eddies decrease as they translate across the southeast Cape Basin most likely due to the interaction within other mesoscale variability. However, no definitive conclusion can be drawn using only a single example.

#### 5.2.2.3 Mature anticyclonic eddy

A large anticyclonic eddy was observed to impact M10 from the 03/03/2015 to 05/06/2015. The anticyclonic eddy was deformed, split and merged with a smaller anticyclonic eddy as it traversed

across the basin. The complex structure and trajectory of the anticyclonic eddy is characteristic of large mesoscale features within the southeast Cape Basin due to the complex interaction with various other mesoscale features (Boebel et al. 2003). The complex interactions resulted in the eddy tracking scheme identifying the feature as numerous separate anticyclonic eddies, however, the feature has been shown to be a coherent structure (Figure 4.10B) as the tracking of the anticyclonic eddy was visually confirmed.

The high variability in the direction of flow observed at M10, indicated by the current rose (Figure 4.10D), highlighted the complex structure of the anticyclonic feature. Numerous directions of flow were observed although the highest concentration of flow was in a north westward and north eastward direction. The predominantly northward flow was consistent with the anticyclonic rotation of the feature which is positioned west of M10 for the majority of the observed period (Figure 10A). The speed through depth showed an oscillating signal of high and low speeds similar to the signal of C1 and C9. The oscillating signal was not consistent showing prolonged periods of low speed as a result of the deforming, splitting and merging of the eddy. As for C1 and C9 the periods of high speed penetrated down to at least 400m depth. There were two periods of substantially increased speed that showed a barotropic signal. The two periods correlated with a strong cyclonic eddy (C7) east of the anticyclonic eddy. The position of the cyclonic eddy (C7) would create additional northward flow; this dipole interaction was responsible for the high speeds observed and the barotropic nature of flow. The mean speed averaged through depth for the observed period was 43.90 $cm/s^{-1}$ with a maximum of 101.93 $cm/s^{-1}$. The maximum (101.93 $cm/s^{-1}$) value was the highest speed observed throughout the entire time series of ADCP data (Figure 4.1). The maximum speed was the result of the eddy dipole interaction mentioned above, again demonstrating the strong impact of dipole interactions within the southeast Cape Basin.

The observed speed and direction of flow through depth showed mesoscale variability generally impacts to a depth of at least 400m and are characterised by a baroclinic signal. Dipole interactions between features created enhanced flows that were occasionally barotropic to at least 400m depth. Considering the complexity associated with mesoscale features within the southeast Cape Basin (Boebel et al. 2003, Richardson 2007, Hall and Lutjeharms 2011); the observations from three case studies are inadequate to infer the general characteristics of mesoscale eddies within the southeast Cape Basin. However, the analysis of the physical characteristics of mesoscale features through the upper water column highlights the potential for future studies using the ADCP data. Similar analysis using long term data sets of the *in situ* observations has enormous potential to show the precise

physical characteristics of mesoscale eddies, through depth, which will allow for better estimates of inter-ocean exchanges.

## 5.3 Investigating the circulation along the shelf edge

The dissimilarity in the speed (Figure 4.1, Table 1) and direction of flow (Figure 4.3) as well as the comparison with the altimetry (Figure 4.4, Table 2) showed mesoscale variability is not the dominant flow dynamic driving the circulation at M7. The flow characteristics through the upper water column were analysed and compared to SLA and SST observations in order to identify the features driving the circulation at M7.

The high speed events observed at M7 did not tend to impact deeper than 350m (Figure 4.11). The clear exception was the event from 1/03/2015 to 15/03/2015 which penetrated to a depth of at least 550m (Figure 4.11). The direction of flow through depth showed the similar trend to the speed through the upper water column, not impacting below 350m depth with the exception of the event from 1/03/2015 to 15/03/2015 (Figure 4.12). Interestingly, all the high speed events observed at M7 are associated with north westward transport (between 270°-360°); with the exception of the anomalous high speed event observed from 1/03/2015 to 15/03/2015 (Figure 4.12, 4.13). The dissimilar nature of this high speed event implied this event may be driven by an alternative feature, which was not responsible for remaining high speed events observed at M7.

### 5.3.1 Investigating features driving the circulation along the shelf edge

In order to identify the features impacting M7 four high speed events were used as case studies. The four case studies were compared to the SLA and SST.

The cool waters upwelled along the coast create a zonal temperature gradient with the relatively warm waters, associated with the Agulhas leakage, further offshore (Bang and Andrews 1974, Veitch and Penven 2017). The temperature gradient produces a horizontal density gradient which drives an equatorward flow (Veitch and Penven 2017). The flow, referred to as the Goodhope Jet or Benguela Jet, is generally strongest over the shelf edge but is observed to shift zonally (Veitch and Penven 2017). Considering the flow is driven by the temperature gradient both the upwelling system and Agulhas influx play a vital role in the strength of the flow. The SST observations were used to identify the SST gradient within the region as a high SST gradient along the shelf edge will most likely induce an equatorward flow. The SLA observations were used to identify the role mesoscale features on the circulation at the position of M7.

The four high speed events used as case studies showed the circulation at M7 was driven by a combination of different oceanographic features (Figure 4.13). The high speed event used for case study 1 was shown to be driven by the density gradient resulting from the cool upwelling waters along the coast and warm waters offshore, associated with the Agulhas influx (Figure 4.14). Conversely, the high speed events used for case study 2 (Figure 4.15) and 4 (Figure 4.17) were driven by a mesoscale eddy (C9) and warm filament respectively. Case study 3 (Figure 4.16) showed no clear feature responsible for the high speed event observed (Figure 4.13). The high speed event was thought to have been induced by a combination of the density gradient and a mesoscale eddy (A18).

The flow characteristics, such as speed, direction of flow and the depth impacted, associated with the different features showed subtle differences through the water column. The impact of the density gradient was shown to produce a north westward transport which penetrated the water column to a depth of approximately 350m (Figure 4.11). The transport reached speeds of >60cm.$s^{-1}$ which were among the highest values recorded at M7 (Figure 4.13). The direction of flow resulting from the density gradient is in agreement with the literature (Bang and Andrews 1974, Veitch and Penven 2017) which provided strong evidence that the circulation at M7 was strongly influenced by the equatorward transport at the shelf edge often referred to as the Benguela Jet.

The impact of the mesoscale eddy (C9) penetrated through the upper water column to a depth of at least 550m and was associated with a direction of flow dependant on the position and rotation of the eddy relative to the mooring array (Figure 4.13). The speed of flow recorded while the mesoscale eddy was observed at the position of M7 was >60cm.$s^{-1}$ (Figure 4.13), which showed the strong influence the feature had on the circulation at the position of M7. The physical characteristics of the mesoscale eddy (C9) and its signal within the ADCP data, observed at M7, was similar to the physical characteristics of the mesoscale eddies observed at the offshore moorings, M8, M9 and M9 (Figure 4.5, 4.6).

The flow that resulted from the impact of the warm filament showed similar physical characteristics to the flow produced by the density gradient, a north westward transport which did not penetrate through the upper water column (Figure 4.11). The direction of flow during the high speed event was suggested to be the result of rotation and position of the feature (A34), which advects the filament north westward. Therefore, the direction of flow resulting from filaments would depend on the nature of the mesoscale feature it is associated with; whereas the flow associated with the Benguela Jet will always be associated with north westward transport due to the horizontal density gradient. The identification of the warm filament, advected from the retroflection region, in the ADCP data was significant as the Agulhas filament hasbeen shown to contribute to the interocean exchange

(Lutjeharms and Cooper 1996). However, *in situ* observations of these filaments are limited and therefore, the exact contribution of these filament to interocean exchange is not well known (Lutjeharms and Cooper 1996). The identification and analysis of filament through depth provides a powerful tool; as similar analysis, with a long term set of data from the SAMBA mooring array, can be used to show the exact contribution of these filaments to interocean exchange.

The four case studies neatly illustrated that the circulation at the shelf edge was driven by a combination of features associated with both the offshore mesoscale variability and the upwelling system. Although the case studies do not provide enough observations for conclusive characteristics of the filaments and Benguela Jet, the observations have the potential to provide long term *in situ* observations of these features which have been predominately studied through satellite and model observations (Lutjeharms and Cooper 1996, Veitch and Penven 2017). The four case studies emphasised the complexity of flow along the shelf edge as the circulation is driven by various oceanographic features. Importantly, the combination of both features associated with the offshore mesoscale variable and coastal upwelling highlights the connectivity between the two systems, which are often studied as separate systems.

### 5.3.2 Observations of the Benguela undercurrent

Throughout the period of ADCP observations a prevailing south eastward (90°-180°) flow below depths of 350m was observed at M7 (Figure 4.12). The south eastward flow was associated with low speeds between 0 and 10cm.s$^{-1}$ (Figure 4.11). The direction, depth and speed of the south eastward flow was consistent with descriptions of the Benguela upwelling system undercurrent (Nelson 1989). Furthermore, the undercurrent was described to follow the shelf edge which was consistent with the position of M7 (Blanke et al. 2005). The undercurrent deepened as it flowed southward which limited the observations of the undercurrent to the northern Benguela system (Veitch et al. 2009). There are few observations of the undercurrent within the southern Benguela system which can be used as a reference with which to compare characteristics of south eastward flow. However, the similarity of the direction, depth and speed of the south eastward flow to the observations of the undercurrent of the northern Benguela system suggested the undercurrent was present at the position of M7. The identification of the undercurrent at M7 provided an opportunity to fully describe and monitor the undercurrent within the southern Benguela upwelling system. Long term *in situ* observations will help to understand the role of undercurrent in the local circulation as characteristics and influence of the undercurrent within the southern Benguela upwelling system is poorly understood due to the lack of observations.

## 5.4 Interaction between mesoscale features and the upwelling front

The variation in speed (Figure 4.1, Table 1), direction of flow (Figure 4.3) and the comparison with the altimetry (Figure 4.4, Table 2) suggested a separation between the flow driven by the offshore mesoscale variability and flow at the shelf edge associated with the upwelling system. However, flow characteristics through the upper water column at M7(Figure 4.11, 4.12), and comparisons to satellite observations (Figure 4.14, 4.15, 4.16) showed that the apparent separation was not straight forward with both mesoscale variability and the upwelling system impacting the circulation at the shelf edge. The combination of features observed at M7 showed the potential for interaction between the upwelling system and mesoscale features. The interaction between mesoscale features and the upwelling system has been previously observed and shown to induce large filaments of upwelling water extending offshore and convoluting the upwelling front (Duncombe Rae et al. 1992, Shannon and Nelson 1996, Hutchings et al. 1998). The filaments were shown to transport productive shelf waters to the open ocean; these advective losses include chlorophyll and fish larvae which strongly influence the local ecosystem (Shillington et al. 1992, Hutchings et al. 1998). These filaments have been observed and described on separate occasions proving the process is recurrent (Duncombe Rae et al. 1992 Nelson et al. 1998). An example of a mesoscale induced cross shelf transport event was observed during the period of ADCP data. The cross shelf transport event was centred over the mooring array which provided a unique opportunity analyse the feature *in situ* and through depth. Furthermore, the high resolution *in situ* data allowed an opportunity to calculate the amount of water transported from the shelf to the open ocean. The quantification of this feature was unique as previous studies were limited to sparse cruise data, which only allowed for rough estimates of the speed and depth impacted by the filament (Shillington et al. 1992, Duncombe Rae et al. 1992, Nelson et al. 1998). The analysis and quantification of the cross shelf transport event will allow for improved understanding on how mesoscale features interact with the upwelling system and improve estimates of their impact in the local marine ecosystem.

### 5.4.1 Mesoscale induced cross shelf transport

An examination of the derived Chl-a satellite observation showed a large filament of high Chl-a water extended from the shelf across the mooring array into the open ocean. The filament was first visible over the mooring array from the 01/10/2014 and was visible until the 16/11/2014. After the 16/11/2014 the high Chl-a filament was advected further offshore and dissipated within the southeast Cape Basin (Figure 4.18). The Chl-a filament was advected offshore by the westward flow, induced by the dipole interactions of a cyclonic (C1) and anticyclonic (A2) eddy pair (Figure 4.18, 4.19). The high

Chl-a associated with the filament showed the cyclonic (C1) and anticyclonic (A2) eddy transported productive, high bio-mass waters from the shelf to the open ocean.

The SST was analysed to identify the origin and temperature signal of the filament. The shape and advection of the high Chl-a filament was mirrored by the 19.6°C isotherm (Figure 4.20). The similarities between shape and advection of the high Chl-a filament and 19.6°C isotherm showed filament was characterised by waters warmer than 19.6°C. It is important to note that the 19.6°C isotherm did not define the high Chl-a filament after the 24/10/2014 due to background waters of a similar temperature while the high Chl-a was visible until 16/11/2014.

The relatively high temperatures associated with the filament indicated that the filament was not advected from the productive upwelling region along the coast, which is characterised by waters lower than 19°C (Veitch et al. 2010). Instead, the filament could be clearly seen to originate over the Agulhas Bank and was connected to the Agulhas Bank throughout the advection of the filament (Figure 4.20). The relatively high temperatures and visual confirmation (Figure 4.20) showed the filament advected productive shelf waters from the Agulhas Bank to the open ocean and not waters from the coastal upwelling adjacent to the mooring array. The loss of productive shelf water from the Agulhas Bank to the open ocean has a substantial impact on the marine ecosystem as several fish species spawn along the Agulhas Bank (Hutchings et al. 2002). The larvae and juveniles are advected from the spawning grounds along the Agulhas Bank by the equatorward coastal jets to the nursery area in St Helena Bay; however, offshore advective losses reduce successful retention (Hutchings et al. 2002). The filament represented an ideal case study of the physical process which drives these advective losses.

### 5.4.2 Quantifying cross shelf transport

The position of the filament over the mooring array provided a unique opportunity to study the advective losses *in situ* with high temporal resolution. The westward (offshore) direction of flow (Figure 4.19) proved the mooring array is able to capture the physical characterises of the filament. The *in situ* data was combined with the observations from the satellite products in order to quantify both the total volume and volume transport of the filament.

The depth impact and speed of flow within the filament was analysed using the *in situ* observations from M8 and M9 (Figure 4.21). The depth was defined by the 30cm.s$^{-1}$ contour which captured the bulk of the high speed, westward flow induced by the filament (Figure 4.21). Defining the filament by the 19.6°C isotherm using the SST observations (Figure 4.20) provided a clear illustration of the shape and spatial variably of the filament and an easily identifiable feature. The dimensions, length and width, of the filament were calculated using 19.6°C isotherm as the boundary of the filament (Figure

4.22, 4.23). The length, width, depth and speed of flow for the filament were measured daily from the 05/10/2014-18/10/2014.

### 5.4.2.1 The total volume

The total volume of the filament was calculated under the assumption the filament formed a general rectangular shape using the length, the width and the depth which were calculated daily. The rectangular form, however, did not fully cover the spatial variability of the filament which was an irregular shape (Figure 4.20). In order to compensate for the irregular shape and high spatial variability of the filament the volume was calculated four times at each daily time step using a combination of two widths and two lengths. The two widths and lengths were visually chosen to provide a robust representation of the dimensions of the filament. The assumption the filament is rectangular in shape implies the filament holds its form through depth and therefore the width does not change width depth, which is highly unlikely. The assumption of the rectangular form decreased the accuracy of the calculations. Furthermore, the choice of contour, the 19.6°C isotherm and 30cm.s$^{-1}$, heavily influenced the dimensions of the filament. Similarly, the position of the section used to measure the length and width influenced the dimensions and final calculations (Figure 4.22, 4.23). Considering the limitations of the total volume calculations, the values presented (Table 3) were not considered precise values but rather improved estimates of advective losses. Previous estimates have been limited to sparse hydrographic data. The total volume calculated using the different lengths showed consistency indicating the combination of the two lengths and two widths provided a robust representation of the spatial variability and irregular shape associated with the filament. The total volume of the filament averaged from 05/10/2014 to 20/10/2014, using a combination of the two widths and two lengths, was in the order of 2 x $10^{12}$ m$^3$ (lowest 2.07x$10^{12}$ m$^3$ff, highest 2.78x$10^{12}$m$^3$) (Table 3).

### 5.4.2.2 The volume transport

The volume transport across two sections of the filament was calculated to further investigate the amount of water transported from the Agulhas Bank to the open ocean. The distance across the two sections, at the position of M8 and M9, were calculated daily and used as the width (Figure 4.23A, 4.23B). The depth impacted was again defined by the 30cm.s$^{-1}$ contour (Figure 4.21). The U-velocity component was used to calculate the volume transport, as it represents the offshore(westward) flow perpendicular to the sections. The U-component was averaged daily and through the upper water at M8 and M9 respectively (Figure 4.21). The width, depth and U-component were used to calculate the volume transport across the two sections daily (Figure 4.23A-B, Table 4). The volume transport was

calculated under the assumption that the filament is a coherent body and therefore the U-component of flow across the filament was identical to the U-component

of flow observed at M8 and M9. The calculation of volume transport also assumed the width of the filament remained constant through depth. As for the calculation of the total volume of the filament the assumptions made in the calculations decreased the accuracy of the volume transport values. Therefore, the volume transport values presented (Table 4) were considered as improved estimates rather than precise values. The volume transport across the two sections of filament averaged from 08/10/2014 to 17/10/2014 was in the order 1Sv (1Sv = $1 \times 10^6 m^3 s^{-1}$); $1.56 \times 10^6\ m^3.s^{-1}$ for M8 and $7.98 \times 10^5\ m^3.s^{-1}$ for M9 respectively (Table 4).

The calculations of both the total volume and volume transport contained numerous assumptions which have been stated. Considering the assumptions made it is important to realise the limitations of the calculations and the values of the total volume and volume transport presented (Table 3, 4). However, the calculations showed the ability of the mooring array to capture the process controlling advective losses. The ability of the mooring array to provide *in situ* observations of interaction between mesoscale features and the upwelling front as well as the resulting advective losses provided an extremely useful tool in improving the understanding of these processes which have previously received little attention in literature due to limited observations. The quantification of the cross shelf transport event provided an improved estimate for the amount of water transported across the shelf by these recurrent features. These estimates can serve as a baseline for future studies of advective losses, informing and guiding future modelling studies, which aim to show the impact of the mesoscale induced cross shelf transport events on the both the local circulation and local biology.

# Chapter 6: Conclusion

The Cape Basin is a complex oceanographic environment characterised by the juxtaposition of extremely energetic offshore mesoscale variability and strong coastal upwelling. The basin has been the focus of many studies due to its vital role in interocean exchanges and coastal-open ocean exchanges.

The offshore mesoscale features originating from the Agulhas retroflection have been shown to transport Indian Ocean waters into the Atlantic Ocean. The size, translation speed, rotational speed and trajectories of these features are well documented (Boebel et al. 2003, Richardson 2007, Dancausse et al. 2010, Hall and Lutjeharms 2011). However, many of the studies have been limited to satellite, model or short time scale hydrographic data (Byrne et al. 1994, Boebel et al. 2003, Rubio et al. 2009, Hall and Lutjeharms 2011). The lack of long term *in situ* datasets has limited the information on these features' physical characteristics through the water column as well as the understanding of how these features interact with each other. The interaction between mesoscale features is known to enhance mixing and therefore, enhance interocean exchange but the exact mechanisms are relatively unknown (Boebel et al. 2003, Richardson 2007). In addition to their role in interocean exchanges, mesoscale features have been observed to interact with the upwelling system (Duncombe Rae et al. 1992, Nelson et al. 1998). The interactions between the offshore mesoscale features and the upwelling system have shown mesoscale features can induce cross shelf transport events advecting productive shelf water from the upwelling system to the open ocean (Duncombe Rae et al. 1992, Hutchings et al. 2002). The loss of productive shelf water strongly impacts the marine ecosystem, as the loss of nutrient rich waters decreases productivity. The cross shelf transport event has also been shown to entrain fish larvae, decreasing the successful retention of various fish species (Hutchings et al. 2002). The studies of these cross shelf transport events have been largely limited to sparse cruise data and model solutions (Shillington et al. 1992, Duncombe Rae et al. 1992, Nelson et al. 1998). The scale of these cross shelf events is relatively unknown due to the lack of high resolution *in situ* data. The uncertainty in the scale of these events decreases the ability to accurately assess the relative impact the cross shelf transport events have on the marine environment.

The SAMBA mooring array was the first long term moored array in the region and provided a sustained period of *in situ* observations through the upper water column. The SAMBA mooring array was ideally positioned for observations of both the offshore mesoscale variability as well as the interactions between the mesoscale variability and the upwelling system. The high resolution data provided an ideal opportunity to identify and analyse mesoscale features through depth. Furthermore, the long term nature of the data allowed for numerous features to be compared, determining the general

physical characteristics of recurrent features through the water column and can be used to highlight interactions between features. The high resolution *in situ* data also provided a rare opportunity to produce detailed analysis of the interactions between mesoscale features and the upwelling system, through the water column. The detailed analysis will help to improve estimates of the scale of these events and therefore, help to understand their relative impact on the upwelling system.

This thesis presented the first year of data from the SAMBA mooring array. Combining the *in situ* observations from the SAMBA mooring array with remote sensing products, the project showed the differences in the circulation across the mooring array and identified the features responsible for the differences in the circulation. The identification of features driving the circulation, specifically the mesoscale variability and upwelling system, showed the ability of the mooring array to capture the dynamics of the southeast Cape Basin. The successful identification of the features from the *in situ* data allowed the project to analyse the feature through the water column. Considering the thesis only presented the first year of data, using the analysis to generalise the physical characteristics of mesoscale features and their interactions with the upwelling front would be premature. Therefore, the analysis was used to show the potential of the *in situ* observations, used in long term studies, to determine the prevailing physical characteristics of mesoscale features and cross shelf transport events within the southeast Cape Basin. The determination of the physical characteristics of mesoscale features and cross shelf transport events will provide a greater understanding of interocean and coastal-open ocean exchange

The ADPC data showed a clear increase in the mean and standard deviation of speed (Figure 4.1 A-D, Table 1) and an increase in the variability of the direction of flow (Figure 4.3) from M7 which was positioned closest to the shelf to M10 which was located furthest offshore. The difference in flow across the mooring array was the result of short time scale, high speed events (Figure 4.2).

In order to investigate what was driving the variation in speed and direction of flow across the mooring array the *in situ* data was compared with satellite observations. The analysis of altimetry observations showed the circulation at the position of M8, M9, and M10 was driven by mesoscale features associated with the offshore mesoscale variability stemming from the Agulhas retroflection and along the shelf edge. The circulation at M7 appeared anomalous and to be driven by features not observed in altimetry data. (Figure 4.4, Table 2).

The confirmation (Figure 4.4, Table 2) that the variation in speed and direction of flow recorded at M8, M9 and M10 was driven by mesoscale variability provided an opportunity for sustained *in situ* observations of the mesoscale features within the southeast Cape Basin. The ADCP data in

conjunction with the eddy tracking scheme was used show the influence of mesoscale variability through the water column and analyse the physical characteristics of individual features.

The analysis conclusively showed mesoscale features within the southeast Cape Basin produced high speed, baroclinic events which penetrated through the upper water column to a depth at least 400m (Figure 4.5). The high speed events characteristic of mesoscale features were not associated with a particular direction of flow, as the direction of flow was dependent on the rotation of the feature and its position relative to the mooring array (Figure 4.6).

The influence of dipole interactions between eddy pairs was frequently observed across the SAMBA array. The dipole interactions were observed to result in substantial increases in speed through the upper water column (50 to 500m depth). The high speed events induced by the dipole interactions were often characterised by baroclinic flows (Figure 4.8, 4.10, 4.16); however, anomalous barotropic flows resulting from dipole interactions were observed (Figure 4.5). The influence of dipole interactions observed at M8, M9 and M10 highlighted the complexity of the southeast Cape Basin as both the mesoscale features and their interactions with each other influenced the circulation of the region.

Three case studies of induvial mesoscale features, which are frequently observed in the region, were analysed; an anticyclonic eddy (Agulhas ring) and two cyclonic eddies (mature and immature cyclonic shelf eddies). The anticyclonic eddy was shown to have a higher average speed (43.90cm.$s^{-1}$) compared to the two cyclonic eddies, 32.33cm.$s^{-1}$ for C1 and 39.85cm.$s^{-1}$ for C7 respectively (Figure4.8, 4.9, 4.10). Interestingly, the immature cyclonic eddy (C7) showed a higher average speed than the mature cyclonic eddy (C1), the difference in speed may have been a result of the interactions between mesoscale features within the southeast Cape Basin. C1 spent a longer time period in the basin before it was observed and therefore, would have experienced more interactions with other mesoscale features than C7. These interactions may have reduced the rotational speed of C1. The three case studies did not provide a large enough sample size to assume the overriding characteristics of mesoscale features within the southeast Cape Basin. However, the case studies showed the potential for long term *in situ* observations from the SAMBA mooring array to characterise and compare individual mesoscale features, defining precise characteristics, through the water column, of mesoscale features within the southeast Cape Basin.

In order to investigate the differences in the circulation observed at M7, four high speed events were used as case studies and compared to satellite observations in order determine the flow dynamic or features driving the circulation at M7. The case studies showed the circulation observed at the position

of M7 was driven by a combination mesoscale features (Figure 4.15), the density gradient driven by the upwelling system (Figure 4.14) and warm filaments originating at the Agulhas retroflection (Figure 4.16).

Each of the features that drove the circulation at M7 was shown to display different flow characteristics through the upper water column (Figure 4.14, 4.15, 4.16). The combination of features driving the circulation is noteworthy as it erodes the notion of a separation between shelf and offshore circulation. Furthermore, the observations of both the impact of mesoscale features and the upwelling system at the position of M7 showed that interaction between the two systems was highly likely.

The ADCP data recorded at M7 showed a prevailing south eastward flow at depths below 350m. The south eastward flow was associated with relatively low speeds (0- 10cm/$s^{-1}$) and was present throughout the period of ADCP observation (Figure 4.11, 4.12). The position, direction, depth and speed of the flow closely resembled the characteristics of the undercurrent observed in the northern Benguela undercurrent (Blanke et al. 2005) and provided conclusive evidence that M7 observed the Benguela undercurrent at the latitude of the mooring array. The identification of the undercurrent at M7 is an important observation as descriptions of the undercurrent within the southern Benguela system are limited (Blanke et al. 2005). The observation of the undercurrent allowed for long term monitoring of the current helping to define the characteristic of the current as well as the long and short-term variability within the current.

The interaction between the offshore mesoscale variability and the upwelling front was investigated using a case study of a mesoscale induced cross shelf transport (Figure 4.18). A mesoscale eddy pair was observed to induce an offshore flow, which transported a substantial amount of productive shelf waters from the shelf, offshore (Figure 4.18). The *in situ* observations were combined with satellite observations to quantify of the amount of water transported from the shelf to the open ocean. The total volume of the filament averaged from 5$^{th}$ of October 2014 to the 20$^{th}$ of October 2014 was in the order of ~2 x $10^{12}$ $m^3$. The volume transport averaged across two sections within the filament from the 8$^{th}$ of October 2014 to the 17$^{th}$ of October 2014 was in the order of ~1Sv. The total volume and volume transport showed that the filament transported a substantial amount of productive waters from the Agulhas Bank shelf to the open ocean. The high Chl-a and origin of the filament, over the Agulhas, suggested the cross shelf transport would have strongly influenced the biology of the region. The improved estimates of cross shelf transport can serve as a baseline for future studies, which will help advance predictions of the scale of cross shelf transport within the region and the associated impacts on the local circulation and biology.

The results of the thesis confirmed the strong influence of mesoscale features on the offshore circulation in the southeast Cape Basin. Importantly, the thesis showed the SAMBA mooring array can successfully capture the influence of these offshore mesoscale features, which allowed for the detailed analysis of individual mesoscale features through the upper water column. Similar analysis using a long time scale data set will provide an improved understanding of the physical characteristics of these features, which will improve the estimates of the interocean exchanges within the region. The results of the thesis also showed the complexity of the circulation at the shelf edge. The circulation was shown to be driven by a combination of processes associated with both the offshore mesoscale variability and the upwelling system. The combination of features highlighted the connectivity between the two systems. The thesis further highlighted the connectivity with the identification of mesoscale induced cross shelf transport event. The *in situ* observations were used to calculate the amount of water transported from the shelf to the open ocean. The quantification of this cross shelf event provided a rare insight into the scale of these events which was previously not well known. The improved estimate of the scale of the cross shelf transport event will help to improve estimates of coastal-open ocean exchanges and their relative impact on the biology.

# References


Ansorge, I. J., et al., 2014, 'Basin-Wide Oceanographic Array Bridges the South Atlantic', Eos Trans. AGU, 95(6), 53.

Arhan, M., Mercier, H. & Lutjeharms, J. R. E., 1999, 'The disparate evolution of three Agulhas rings in the South Atlantic Ocean', *Journal of Geophysical Research*, 104(C9), 20987–21005, doi:10.1029/1998JC900047.

Andrews, W.R.H. & Hutchings, L., 1980, ''Upwelling in the Southern Benguela Current', *Progress in Oceanography,* 9(1), 1-8.

Baker-Yeboah, S., Flierl, G.R., Sutyrin, G.G. & Zhang, Y., 2010, 'Transformation of an Agulhas eddy near the continental slope'. *Ocean Science* 6, 143–159.

Bang, N.D. & Andrews, W.R.H., 1974,' Direct Current Measurements of a Shelf-Edge Frontal Jet in the Southern Benguela System', *Journal of Marine Research*, 32 (3), 405–417.

Beal, L., De Ruijter, W.P.M., Biastoch & A., Zahn, R. 2011, 'On the role of the Agulhas system in ocean and climate circulation', *Nature* 472, 429-436.

Biastoch, A., Boning, C.W. & Lutjeharms, J.R.E., 2008, 'Agulhas leakage dynamics affects decadal variability in Atlantic overturning circulation', *Nature* 456, 489-492.

Blanke, B., Speich, S., Bentamy, A., Roy, C. & Sow, B., 2005, 'Modeling the structure and variability of the southern Benguela upwelling using QuikSCAT wind forcing', *Journal of Geophysical Research*, 110, C07018, doi:10.1029/2004JC002529.

Boebel, O., Lutjeharms, J., Schind, C., Zenk, W., Rossby, T. & Barron, C., 2003, 'The Cape Cauldron: a regime of turbulent inter-ocean exchange', *Deep-Sea Research* II 50 (2003). 57 - 86.

Boebel, O., Duncombe Rae, C., Garzoli, S., Lutjeharms, J.R.E., Richardson, P., Rossby, T., Schmid, C., Zenk, W, 1998, 'Float experiment studies interocean exchanges at the tip of Africa', *Earth & Space News,* 79(1), 1-8.

Brown, P.C., Painting, S.J. & Cochrane, K. L., 1991., 'Estimates of phytoplankton and bacterial biomass and production in the northern and southern Benguela ecosystems', *South African Journal of Marine Science,* 11(1), 537-564.

Byrne, D.A., Gordon, A.L & Haxby, W.F., 1994, 'Agulhas Eddies: A Synotip View Using Geostat ERM Data', *Journal of Physical Oceanography,* 25, 902-917.

Chaigneau, A., Eldin, G. & Dewitte, B., 2009,' Eddy activity in the four major upwelling systems from satellite altimetry (1992–2007)', *Progress in Oceanography*, 83, 117–123, doi:10.1016/j.pocean.2009.07.012

De Ruijter W.P.M. & Boudra, D.B., 1985,'The wind-driven circulation in the South Atlantic-Indian Ocean — I. Numerical experiments in a one-layer model', *Deep-Sea Research* 32(5), 557–574.

De Ruijter, W.P.M., Biastoch, A., Drijfhout, S.S., Lutjeharms, J.R.E., Matano, R.P., Weijer, W., Van Leeuwen, P.J., Pichevin, T. & Weijer, W., 1999a, 'Indian-Atlantic interocean exchange: Dynamics, estimation and impacts', *Journal of Geophysical Research* 104(C9), 20,885-20,910.

De Ruijter W.P.M., van Leeuwen, P.J. & Lutjeharms, J.R.E., 1999b, 'Generation and Evolution of Natal Pulses: Solitary Meanders in the Agulhas Current', *Journal of Physical Oceanography, 29, 3043–3055.*

Dencausse, G. Arhan ,M. & Speich, S., 2010, 'Routes of Agulhas rings in the south eastern Cape Basin', *Deep-Sea Research I* 57, 1406-1421.

Donohue, K.A. & Toole, J.M., 2003, 'A near-synoptic survey of the Southwest Indian Ocean'*, Deep-Sea Research* II 50 (2003), 1893–1931.

Duncombe Rae, C.M., Garzoli, S.L & Gordon, A.L., 1996, 'The eddy field of the southeast Atlantic Ocean: A statistical census from the Benguela Sources and Transports Project', *Journal of Geophysical Reasearch,* 101(C5), 11949–11964.

Duncombe Rae, C.M., Shillington, F.A., Agenbag, J.J., Taunton-Clarke, J. & Grundligh, M.L., 1992, 'An agulhas ring in the South Atlantic ocean and its interaction with the Benguela upwelling frontal system', *Deep Sea Research I ,*39(11-12), 2009-2027.

Garzoli, S.L. & Gordon, A.L., 1996, 'Origins and variability of the Benguela Current', *Journal of Geophysical Research,* 10 (C1), 897–906.

Gordon, A.L., Weiss, R.F., Smethie, W & Warner, M., 1992, 'Thermocline and Intermediate Water Communication Between the South Atlantic and Indian Oceans', *Journal of Geophysical Research* 95(c5), 7223-7240.

Hall, C. & Lutjeharms, J. R. E., 2011, 'Cyclonic eddies identified in the Cape Basin of the South Atlantic Ocean', *Journal of Marine Science,* 85(2011), 1-10.

Hardman-Mountford, N.J., Richardson, A.J., Agenbag, J.J., Hagen, E., Nykjaer, L., Shillington, F.A. & Villacasin, C., 2003, 'Ocean climate of the South East Atlantic observed from satellite data and wind models', *Progress in Oceanography,* 59, 181-221.

Hutchings, L., Beckley, L.E., Griffiths, M.H., Roberts, M.J., Sundby, S.& van der Lingen, C., 2002, 'Spawning on the edge: spawning grounds and nursery areas around the southern African coastline', *Marine and Freshwater Research,* 53(2), 307 – 318.

Hutchings, L., Barange, M. , Bloomer S. F. , Boyd A. J., Crawford, R. J. M, Huggett, J. A., Kerstan M., Korrûbel, J.L., de Oliveira J. A. A., Painting S. J., Richardson A.J., Shannon L.J., Schülein, F.H., van der Lingen, C.D. & Verheye H. M., 1998, 'Multiple factors affecting South African anchovy recruitment in the spawning, transport and nursery areas', *South African Journal of Marine Science*, 19(1), 211-225.

Hutchings, L., van der Linden, C.D., Shannon, L.J., Crawford, R.J.M., Verheye, H.M.S., Barthlolmare, C.H., van der Plas, A.K., Louw, D., Kreiner, A., Ostrowski, M., Fidel, Q., Barlow, R.G., Lamont, T., Coetzee, Z., Shillington, F., Veitch, J., Currie, J.C. & Moneiro, P.M.S., 2009, 'The Benguela Current: An ecosystem of four components', *Progress in Oceanography*, 83(1-4),15-32.

Lutjeharms, J.R.E. & Van Ballegooyen R.C., 1988, 'The Retroflection of the Agulhas Current', *Journal of Physical Oceanography,* 18(November 1988). 1570-1583.

Lutjeharms, J.R.E. & Cooper, J., 1996, 'Interbasin leakage through Agulhas current filaments', *Deep Sea Research Part I: Oceanographic Research Papers*, 43(2), 213-215, 217-238.

Lutjeharms, J.R.E. & Meeuwis, J.M., 1987, 'The extent and variability of South-East Atlantic upwelling', *South African Journal of Marine Science,* 5(1), 51-62.

Lutjeharms, J.R.E., Boebel, O. & Rossby, H.T., 2003, 'Agulhas cyclones', *Deep Sea Research Part II: Topical Studies in Oceanography,* 50(1), 13-34.

Lutjeharms, J.R.E., 2006, 'The Agulhas Current', *Springer Berlin Heidleberg*.

Mohrholz, V., Bartholomae, C.H., van der Plas, A.K. & Lass, H.U., 2008, The seasonal variability of the northern Benguela undercurrent and its relation to the oxygen budget on the shelf, *Continental Shelf Research,* 28(3), 424-441.

Nelson, G., 1989, Poleward Motion in the Benguela Area. In: Neshyba S.J., Mooers C.N.K., Smith R.L., Barber R.T. (eds) Poleward Flows Along Eastern Ocean Boundaries. Coastal and Estuarine Studies (formerly Lecture Notes on Coastal and Estuarine Studies), vol 34. Springer, New York, NY

Nelson, G., Boyd, A.J., Agenbag, J.J. & Duncombe Rae, C.M., 1998, 'An upwelling filament north-west of Cape Town, South Africa', *South African Journal of Marine Science*, 19(1), 75-88, DOI: 10.2989/025776198784126953.

Richardson, P.L., 2007, 'Agulhas leakage into the Atlantic estimated with subsurface floats and surface drifters'. *Deep-Sea Research* I., 54, 1361–1389.

Rubio, A., Blanke, B., Speich, S., Grima, N. & Roy, C., 2009, 'Mesoscale eddy activity in the southern Benguela upwelling system from satellite altimetry and model data', *Progress in Oceanography,* 83, 288–295.

Peterson, R.,G. & Starmma, L., 1991, 'Upper-level circulation in the South Atlantic Ocean', *Progrees in Oceanography,* 26(1), 1-73.

Pujol, M. I., Faugère, Y., Taburet, G., Dupuy, S., Pelloquin, C., Ablain, M. and Picot, N. (2016). DUACS DT2014: the new multi-mission altimeter data set reprocessed over 20 years. Ocean Sci., 12(5), 1067-1090, doi: 10.5194/os-12-1067-2016.

Schmid, C., Boebel, O., Zenk, W., Lutjeharms, J.R.E., Garzoli, S.L., Richardson, P.L. & Barron, C., 2003, 'Early evolution of an Agulhas Ring'. *Deep-Sea Research* II 50, 141–166.

Shannon, L.V., 1985, The Benguela ecosystem. I: Evolution of the Benguela physical features and processes*', Oceanography and Marine Biology*, 23, 105-182.

Shannon, L.V. & Nelson, G., 1996, 'The Benguela: Large Scale Features and Processes and System Variabilty',in *The South Atlantic: Present and Past Circulation*, 163–210, Springer.

Shelton, P.A., & Hutchings, L., 1982, 'Transport of anchovy, Engraulis capensis Gilchrist, eggs and early larvae by a frontal jet current', *Journal of Marine Science*, 40(2),185–198, https://doi.org/10.1093/icesjms/40.2.185

Shillington, F.A., Hutchings, L., Probyn, T.A., Waldron, H.N & Peterson, W.T, 1992, 'Filaments and the Benguela frontal zone: offshore advection or recirculating loops?', *South African Journal of Marine Science*, 12:1, 207-218.

Stramma, L. & England, M., 1999, 'On the water masses and mean circulation of the South Ocean Atlantic', *Journal of Geophysical Research*, 104(C9), 20863-20883.

Van Aken, H.M., van Veldhoven, A.K., Veth, C., de Ruijter, W.P.M., van Leeuwen, P.J., Drijfthout, S.S., Whittle, C. & Rouault, M., 2003, 'Observations of a young Agulhas ring, Astrid, during MARE in March 2000', *Deep-Sea Research Part II,* 50, 167-195.

Van Leeuwen, P. J., de Ruijter, W. P. M., & Lutjeharms, J.R.E., 2000, 'Natal pulses and the formation of Agulhas rings', *Journal of Geophysical Research*., 105(C3), 6425–6436,doi:10.1029/1999JC900196.

Veitch, J., Penven, P. & Shillington, F., 2009, 'The Benguela: A laboratory for comparative modelling studies', *Progress in Oceanography*, doi:10.1016/ j.pocean.2009.07.008

Veitch, J., Penven, P. & Shillington, F., 2010, 'Modelling Equilibrium Dynamics of the Benguela Current System', *Journal of Physical Oceanography,* 40, 1942-1964, doi:10.1175/2010JPO4382.1

Veitch, J. & Penven, P., 2017, 'The role of the Agulhas in the Benguela Current system: A numerical modelling approach', *Journal of Geophysical Research: Oceans,* 122, doi:10.1002/2016JC012247.

Wedepohl, P.M., Lutjeharms, J.R.E. & Meeuwis, J.M., 2000, 'Surface Drift in the South-East Atlantic Ocean', *African Journal of Marine Science,* 22, 71-79.